

Computational Hemodynamic Modeling of Pediatric Cardiovascular Diseases

by

Christopher Tossas-Betancourt

A dissertation submitted in partial fulfillment
of the requirements for the degree of
Doctor of Philosophy
(Biomedical Engineering)
in the University of Michigan
2023

Doctoral Committee:

Professor David Kohn, Chair
Professor Daniel Beard
Associate Professor Jimmy Lu
Professor David Nordsletten

Christopher Tossas-Betancourt

tossas@umich.edu

ORCID iD: 0000-0002-1352-7923

© Christopher Tossas-Betancourt 2023

Acknowledgements

I would like to first thank my family – William, Madeline, and Joshua – for their unconditional support and never-ending love. They have taught me some of the most valuable life lessons and helped me tremendously in achieving my academic goals. ¡Los amo con todo mi corazón! I would also like to acknowledge my uncle, Alex, for his continual support in my academic career, and for the countless times he has taught me something or made me laugh.

I would like to thank my PhD advisor, Professor C. Alberto Figueroa, for his mentorship throughout these years and creating a collaborative and fun lab environment. He gave me an opportunity to be involved in some amazing projects, and supported me throughout to ensure that these projects have impactful clinical implications.

I would like to give a special thank you to my committee members: Professor David Nordsletten for sharing his knowledge on ventricular modeling, mentorship, and contagious happy mood; Professor Jimmy Lu for his clinical perspective, and willingness to meet and answer any of my clinical questions; Professors David Kohn and Daniel Beard for their support in my journey towards receiving a PhD.

I also would like to thank my collaborators who have been key in the execution of this work. Dr. James Stanley and Dr. Adam Dorfman for their advice and clinical perspective, which was key to amplifying the clinical impact of my work. Professors Lik Chuan Lee and Sheikh Mohammad Shavik whose work set the foundation for the ventricular models used in this thesis. Dr. Vasilina Filonova for her mentorship and guidance in the earlier part of my PhD. Lastly, I would like to thank the clinical teams from Mott Children’s Hospital (Drs. Mary Olive, Ronald

Grifka, Wendy Whiteside, Heang Lim, Arash Salavitarbar, and Katherine Afton) and Nationwide Children's Hospital (Drs. Simon Lee, Christina Phelps, Robert Gajarski, and Brian Beckman) for their help and support.

I am very thankful for all the members of the computational vascular biomechanics lab: Theo and Kritika (the lab youngsters/elders) for their endless support; Liz, Nic, Jonas, Federica, Taeouk, Yunus, Pieter, Sabrina, Nitesh, Abhilash, Alex, Chris Arthurs, Diederik, Ignas, and Jonathan for all the memories and laughs we shared. My lab is one of the most supportive and fun groups I've had the pleasure to be a part of. I will miss all of you and hope that you continue our favorite lab traditions, from roasting marshmallows for smores (in places we probably shouldn't) to spending countless hours finishing puzzles.

I would like to thank my friends who have served as a family in the U.S. Jared and Claudia: I cannot express how much you both mean to me and I hope to see more of you in the coming years. I would like to thank my little family in Ann Arbor – Sang, Ravi, Dan, Nick, Kelly, Tim, Scott, Pieter – for making my time in Ann Arbor special. It was incredible to share this journey with all of you!

In grad school, I met my partner and best friend, Laura. I could not have completed this journey without your love, support, and contagious laugh. Thank you for helping me every step of the way (including editing my long thesis document) and never failing to cheer me up or make me laugh along the way. I could not be more excited for the next chapter in our lives. I would also like to thank Laura's family for welcoming me with open arms and for their support. I'm looking forward to spending many more holidays together!

Table of Contents

Acknowledgements.....	ii
List of Tables	viii
List of Figures	x
List of Appendices	xiv
List of Acronyms	xv
Abstract	xvii
Chapter 1 Introduction	1
1.1 Cardiovascular system.....	1
1.2 Hemodynamics and cardiovascular disease	3
1.3 Pediatric cardiovascular disease	4
1.3.1 Clinical management	4
1.4 Computational modeling	5
1.4.1 Investigating the effects of hemodynamics in CVD.....	5
1.4.2 Patient stratification.....	6
1.4.3 Surgical planning.....	7
1.5 Diseases of interest.....	8
1.5.1 Pulmonary arterial hypertension.....	8
1.5.2 Renovascular hypertension caused by an abdominal aortic coarctation	9
1.5.3 Hypoplastic left heart syndrome.....	10
1.6 Structure of Thesis	12
Chapter 2 Background	14

2.1 Arterial hemodynamics	14
2.1.1 Disease and arterial stiffness	15
2.2 Ventricular hemodynamics	16
2.2.1 Ventricular function.....	17
2.2.2 Changes in ventricular function.....	19
2.3 Ventricular-arterial coupling	20
2.4 Computational modeling	22
2.4.1 Central pulmonary and systemic arterial modeling.....	22
2.4.2 Ventricular modeling.....	24
Chapter 3 Multi-Scale Closed-Loop Modeling Framework to Study PAH Pathophysiology	26
3.1 Original publication information.....	26
3.2 Introduction	26
3.3 Materials and Methods	28
3.3.1 Clinical Data.....	29
3.3.2 Patient demographics and clinical metrics	31
3.3.3 Strategies for mitigation of inconsistencies in clinical data	31
3.3.4 High-resolution arterial model	37
3.3.5 High-resolution ventricular model	44
3.3.6 Metrics for disease severity stratification.....	49
3.4 Results	51
3.4.1 High-resolution arterial models	51
3.4.2 High-resolution ventricular models	54
3.4.3 Metrics for disease severity stratification.....	55
3.5 Discussion	57
3.5.1 Clinical Applications	59

3.6 Limitations	60
Chapter 4 Hemodynamic Mechanisms Contributing to Renovascular Hypertension Caused by an Abdominal Aortic Coarctation.....	63
4.1 Original publication information.....	63
4.2 Introduction	63
4.3 Methods.....	64
4.3.1 Patient history.....	65
4.3.2 Imaging data	65
4.3.3 Thoracoabdominal bypass	66
4.3.4 Kidney size	67
4.3.5 Computational modeling	67
4.4 Results	70
4.4.1 Postoperative course.....	70
4.4.2 Preoperative simulation	71
4.4.3 Postoperative simulations.....	72
4.4.4 Kidney size	74
4.5 Discussion	75
4.5.1 Clinical experience	79
4.5.2 Computational modeling	79
4.6 Limitations	81
4.7 Conclusions	83
Chapter 5 Interventional Planning for Endovascular Revision of a Lateral Tunnel Fontan.....	84
5.1 Original publication information.....	84
5.2 Introduction	84
5.3 Methods.....	86
5.3.1 Patient's history	86

5.3.2 Rationale for proposed endovascular repair	87
5.3.3 Clinical data acquisition	88
5.3.4 Computational analysis	88
5.3.5 Energy dissipation	93
5.4 Results	94
5.4.1 Pre-intervention model	94
5.4.2 Post-intervention model.....	95
5.5 Clinical decision making	97
5.6 Discussion	98
Chapter 6 Conclusion.....	102
6.1 Pulmonary arterial hypertension (Chapter 3)	102
6.1.1 Summary of contributions and conclusions	102
6.1.2 Future directions	103
6.2 Renovascular hypertension caused by an abdominal aortic coarctation (Chapter 4).....	105
6.2.1 Summary of contributions and conclusions	105
6.2.2 Future directions	105
6.3 Hypoplastic left heart syndrome (Chapter 5)	108
6.3.1 Summary of contributions and conclusions	108
6.3.2 Future directions	109
6.4 General conclusions	109
Appendices.....	110
Appendix A Supplementary Strategies to Mitigate Data Inconsistencies.....	111
Appendix B Abdominal Aortic Coarctation Models: Additional Information	119
Bibliography	124

List of Tables

Table 3.1 Summary of patient demographics and clinical metrics (MRI- and cath-derived).....	32
Table 3.2 Hemodynamic metrics and tuned parameters of the high-resolution arterial model.	42
Table 3.3 Hemodynamic metrics and tuned parameters of the high-resolution ventricular models.	48
Table 3.4 Stratification of patients from lowest (value of 1) to highest (value of 8) disease severity.	50
Table 3.5 Spearman’s rank correlation coefficients (ρ), p-values (p-val), and Benjamini- Hochberg critical value (iQ/m) of each data-derived and model-derived metric resulting from a comparison to clinical disease severity rankings are shown in two columns.	56
Table 4.1 Simulated mean flow rates in mL/min.	74
Table 5.1 Parameter values and units for components of the single ventricle heart model. The time constants are expressed in terms of the cardiac cycle length ($T = 0.8$ s).....	93
Table 5.2 Calibrated parameter values of Windkessel models.	94
Table A 1 Truncated ventricular volumes (mL) and ejection fractions (%).	112
Table A 2 Patient-specific arterial wall stiffness ($g/(mm*s^2)$) calculated from PC-MRI and catheterization data.	113
Table A 3 Patient-specific elastance waveform parameter values.	113
Table A 4 Calibrated parameter values of patient-specific closed-loop ventricular models.	114
Table A 5 The disease severity stratification analysis used the aggregate of patient demographics, data-derived metrics (MRI- and cath-derived), and model-derived metrics.	115
Table A 6 Normalized sensitivity values of measured hemodynamic metrics to parameter changes of 10% in the high-resolution arterial model of Subject #6. Normalized sensitivity value represents a ratio of change in error relative to a parameter value change.	117

Table A 7 Normalized sensitivity values of measured hemodynamic metrics to parameter changes of 10% in the high-resolution ventricular model of Subject #6. Normalized sensitivity value represents a ratio of change in error relative to a parameter value change. 118

Table B 1 Parameter values for the three-element Windkessel models used in the preoperative model (left) and all postoperative models (right). 123

Table B 2 Simulated mean flow rates in mL/min. Hepatic Left Artery in Preoperative model includes the addition of mean flow from both Hepatic Artery 1 and Hepatic Artery 2. Mean flows for all branches were matched within 5% error margins. 123

List of Figures

Figure 1.1 Diagram of the cardiovascular system containing the heart, its four chambers, and the systemic and pulmonary circulations.....	1
Figure 1.2 Schematic of blood pressure along the systemic and pulmonary circulations.	3
Figure 2.1 Positive feedback loop between local wall mechanics and global hemodynamics that describe the relationship between hemodynamics and disease. Increases in pressure (consequent of CVD) cause increases in stiffness, and vice versa. Adapted from [71].....	16
Figure 2.2 Top: Pressure and volume waveforms of the left ventricle. Bottom: Pressure-volume loop of the left ventricle, with the four phases, end-systolic and end-diastolic pressures, volumes, and pressure-volume relationships.....	17
Figure 2.3 Derivation of ESPVR by altering preload via vena cava occlusion.....	19
Figure 2.4 Changes in (A) contractility, (B) preload, and (C) afterload lead to affect the pressure-volume relationship.....	20
Figure 2.5 PV loops at three different stages: healthy (blue), diseased but coupled (green), diseased and uncoupled (purple), which is progressing towards ventricular failure. Adapted from [50].....	21
Figure 3.1 Workflow of study investigating the effects of PAH. Clinical data was acquired and adjusted to mitigate inconsistencies. Clinical and computational metrics (derived from the computational models) were used in the clinical disease severity stratification.	29
Figure 3.2 MRI was performed to acquire arterial anatomy and hemodynamics (A), and ventricular volumes (B). Catheterization was performed to acquire ventricular and arterial pressures (C).	31
Figure 3.3 (A) PV loop built by aligning ECG-gated pressure and volume waveforms. (B) Optimization algorithm shifts data to define a new PV loop, an ellipse is fitted to each iteration. The optimally aligned PV loop is the iteration with the maximum area.	36
Figure 3.4 Multi-scale closed-loop model consisting of high-resolution (3D) arterial models of aorta and large pulmonary arteries, coupled to (0D) lumped parameter models of heart (H) and distal circulations (W).....	40

Figure 3.5 (A) Workflow for boundary condition design and calibration of high-resolution arterial models. (B-D) Stage 1-3 of boundary condition design, respectively. (E) Strategy for ventricular volume adjustment.....	44
Figure 3.6 High-resolution (3D) ventricular model coupled to a 0D closed-loop circulatory model, which includes the systemic and pulmonary arteries, venous systems, atria, and valves.	45
Figure 3.7 Metrics derived from the high-resolution ventricular models.....	51
Figure 3.8 Velocity and pressure maps of the high-resolution arterial models at peak systole. Hemodynamic comparison shows agreement between simulated and clinical data.....	52
Figure 3.9 Distribution of total pulmonary arterial resistance and compliance between central (3D model, shown in blue) and peripheral (lumped-parameter models, shown in red) pulmonary vessels.....	53
Figure 3.10 Displacement maps of ventricular models at end-systole and end-diastole. Comparison of LV and RV PV loops shows agreement between simulated and clinical data. ...	55
Figure 4.1 Preoperative (left) and postoperative (right) image data and corresponding computational models.....	66
Figure 4.2 Left: Preoperative anatomy containing the PC-MRI planes (1 and 2) at which the flow measurements were acquired. Right: Comparison between the clinically measured flow and pressure data, and the simulation results in the validated preoperative model.....	68
Figure 4.3 Close-up posterior views of the abdominal coarctation region and the renal arteries of all TAB (left) and PA (right) surgical options. Graft material of the bypass and patch is presented in gray.....	69
Figure 4.4 Left: 3D maps of preoperative hemodynamics in peak systole. Right: flow (blue) and pressure (red) waveforms in the ascending aorta, left renal artery, and right renal artery.....	70
Figure 4.5 Left: 3D maps of preoperative hemodynamics in peak systole. Note the high velocities and large pressure gradient through the coarctation. Right: flow (blue) and pressure (red) waveforms in the ascending aorta, left renal artery, and right renal artery.....	71
Figure 4.6 Comparison of the renal artery waveforms between the preoperative and control case shows that removal of the pathologic anatomy results in higher renal pressures, elimination of the high-frequency disturbances and systolic dominated waveforms.....	72
Figure 4.7 Ascending aortic pressure waveforms in all models. All postoperative models exhibited an important pressure reduction compared to the preoperative state. PA procedures resulted in a greater decrease of aortic pressure compared to TAB procedures.....	73
Figure 4.8 Renal flow waveforms in all models. Both TAB and PA resulted in restoration of systolic-dominated renal flows, reduction of high frequency disturbances and increased flow. .	75

Figure 4.9 Renal pressure waveforms in all models. Most surgical repairs resulted in a reduction in renal artery pressures, associated with the large reductions in aortic pressures in all postoperative models.	76
Figure 4.10 Comparison of the flow waveforms from the TAB-14mm simulation results and PC-MRI imaging data at 1-year follow-up.	77
Figure 4.11 Comparison of the flow waveforms from the TAB-14mm simulation results and PC-MRI imaging data at 1-year follow-up.	78
Figure 4.12 Velocity streamlines for the PA-50% model at mid-deceleration (t=0.30 s). Disturbed flow patterns are clearly evident in the region of the patch, propagating into the renal arteries.	82
Figure 5.1 Patients with hypoplastic left heart syndrome typically undergo staged palliation consisting of 3 consecutive surgeries. (A) Stage 1: Norwood, (B) Stage 2: Hemi-Fontan, and (C) Stage 3: Lateral Tunnel Fontan.	85
Figure 5.2 A model of the Fontan pathway was constructed from MRI data (A). Path lines and vessel contours were used to delineate and loft the vessels (B), which were blended to create an anatomical model (C), and subsequently discretized to create a FE mesh.	89
Figure 5.3 Distribution of stiffness and thickness of the pre- and post-intervention models. The introduction the endograft blocks the fenestration, which was therefore excluded from the post-intervention model.	90
Figure 5.4 3D-0D open loop model of the HLHS patient includes an FSI model of the Fontan circulation containing venae cavae, pulmonary arteries and fenestration, and lumped-parameter network of models.	92
Figure 5.5 Top: Velocity volume rendering and pressure contour at systole. Comparison between flow and pressure waveforms at the LPA, IVC, SVC, and RPA show good agreement. Bottom: Comparison between simulated results (light gray) and clinical data (dark gray).	95
Figure 5.6 Velocity streamlines depict swirling flow and low velocities in the dilated portion of the Fontan pathway.	96
Figure 5.7 Comparison between pre- and post-intervention hemodynamics. Endovascular intervention led decreases in mean flow and increases in mean pressure at IVC and SVC and increases in backflow at the IVC.	97
Figure 6.1 Left: Canine data for anatomy, hemodynamics, and arterial wall properties. Right: Results corresponding to a 60% diameter reduction AAC model and 12 mm TAB repair. Highly disturbed flow is seen in the isolated AAC and TAB repair models.	106
Figure 6.2 Timeline for the experimental portion of the study. Data acquisition will include anatomical and flow measurements from MRI, pressure measurements from catheterization, and renin concentration from venous assays.	107

Figure B 1 Renal flow waveforms in preoperative models with mesh sizes of 2.5 million elements (blue) and 4.9 million elements (red). Local mesh refinement methods were used to increase mesh size in the region of the aortic narrowing and renal arteries. 121

Figure B 2 Simulations of the preoperative model were run with a time step size of 2.5×10^{-5} s (blue) and 5×10^{-6} s (red). All waveforms exhibit high-frequency disturbances, confirming the presence of high-frequency disturbances in both temporal resolutions. 121

Figure B 3 Left: 3D maps of preoperative hemodynamics in peak systole. Right: flow (blue) and pressure (red) waveforms in the ascending aorta, left renal artery, and right renal artery. The renal artery waveforms reveal near normal systolic dominated flows. 122

List of Appendices

Appendix A	Supplementary Strategies to Mitigate Data Inconsistencies.....	111
Appendix B	Abdominal Aortic Coarctation Models: Additional Information	119

List of Acronyms

- AAC** Abdominal aortic coarctation
- ATA** Ascending thoracic aorta
- BCT** Brachiocephalic Trunk
- CFD** Computational Fluid Dynamics
- CVD** Cardiovascular Disease
- DTA** Descending Thoracic Aorta
- EDV** End-Diastolic Volume
- ESPVR** End-Systolic Pressure Volume Relationship
- ESV** End-Systolic Volume
- FEM** Finite Element Method
- HLHS** Hypoplastic Left Heart Syndrome
- LV** Left Ventricle
- LCCA** Left Common Carotid Artery
- LPA** Left Pulmonary Artery
- LSA** Left Subclavian Artery
- MPA** Main Pulmonary Artery
- MRI** Magnetic Resonance Imaging

PAH Pulmonary Arterial Hypertension

PC-MRI Phase-Contrast Magnetic Resonance Imaging

PWV Pulse Wave Velocity

RAAS Renin-Angiotensin-Aldosterone System

RPA Right Pulmonary Artery

RV Right Ventricle

SAAC Suprarenal Abdominal Aortic Coarctation

SV Stroke Volume

Abstract

Pediatric cardiovascular disease (CVD) is one of the leading causes of mortality in children. While innovations in pediatric CVD treatment have improved mortality and morbidity, the incidence of residual disease remains high. This is in part due to management of pediatric CVD being based on single institution observational studies or extrapolated from studies conducted on adult populations. Another significant hurdle is the growing variability in pathophysiology, where only a small number of patients with a particular pediatric CVD can be recruited in clinical studies. Furthermore, patient-specific hemodynamics are intrinsically linked to the onset and progression of CVD. Therefore, there is a pressing need to improve our understanding of pediatric CVD while considering patient-specific hemodynamics and individualizing treatment plans.

Computational hemodynamic modeling can be used to gain insight on the pathophysiology of an individual patient. Models can leverage information from various sources, such as patient-specific hemodynamic data and literature biomechanical data, to inform its parameters and assumptions and provide a comprehensive description of an individual's condition. Computational modeling can be used to gather in-depth information about disease progression, treatment planning, and develop diagnostic criteria. In this thesis, we leverage computational modeling to study three pediatric CVDs: pulmonary arterial hypertension (PAH), renovascular hypertension caused by an abdominal aortic coarctation (AAC), and hypoplastic left heart syndrome (HLHS).

Chapter 1 Introduction

1.1 Cardiovascular system

The primary purpose of the cardiovascular system is to deliver nutrient- and oxygen-rich blood to organs and tissues in the body. The cardiovascular system also removes waste from cells and transports them to organs, such as the kidneys and liver, for removal. Components of the cardiovascular system (heart, arteries, veins, and capillaries) work in unison to meet these goals under various conditions, such as exercise, sleep, disease, etc. The heart, the central organ of the cardiovascular system, uses its four chambers – left atrium, right atrium, left ventricle, and right ventricle – to deliver blood to the systemic and pulmonary circulations (**Figure 1.1**).

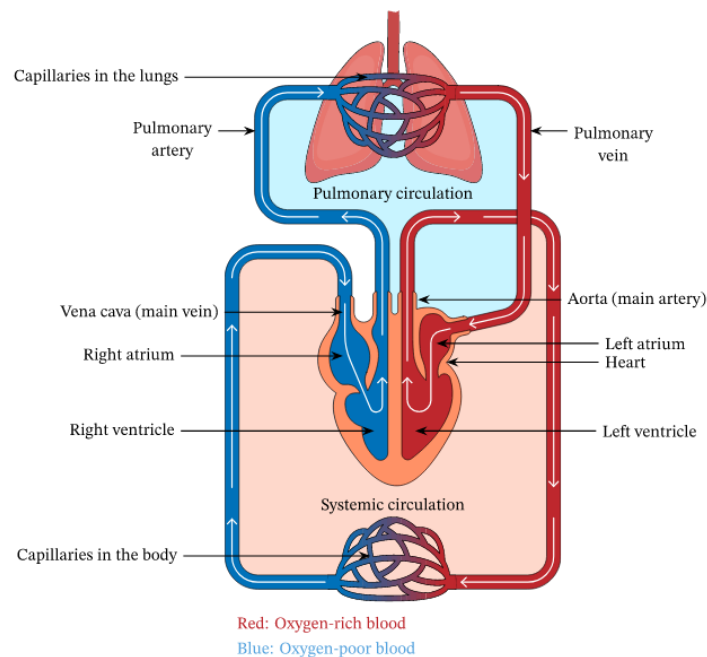


Figure 1.1 Diagram of the cardiovascular system containing the heart, its four chambers, and the systemic and pulmonary circulations¹.

¹ Image: <https://www.nagwa.com/en/explainers/912123271719/>

The left atrium receives oxygenated blood from the pulmonary veins and supplies it to the left ventricle. The left ventricle pushes blood that flows through the aorta to small arteries until it reaches the capillaries, where the oxygen and nutrients are diffused to the tissues and organs. Deoxygenated blood then travels through the systemic veins into the right atrium, where blood gets pushed to the right ventricle. The right ventricle contracts to push deoxygenated blood into the pulmonary arteries until they reach the alveoli. In the alveoli, gas is exchanged, and oxygen is passed from the lungs into the blood. This oxygenated blood flows through the pulmonary veins into the left atrium, completing this cycle.

The cardiovascular system performs its function while operating in a physiologic range of pressures (**Figure 1.2**), where the highest levels of pressure are observed in the ventricles and large arteries, and the lowest levels of pressure are observed in the veins, capillaries, and atria. In healthy adults, systemic arterial pressure is 120/80 mmHg. Furthermore, healthy mean pulmonary arterial pressure is around 14 mmHg [1]. Alterations to these pressures or lesions to the structure of the cardiovascular system are linked with cardiovascular disease (CVD).

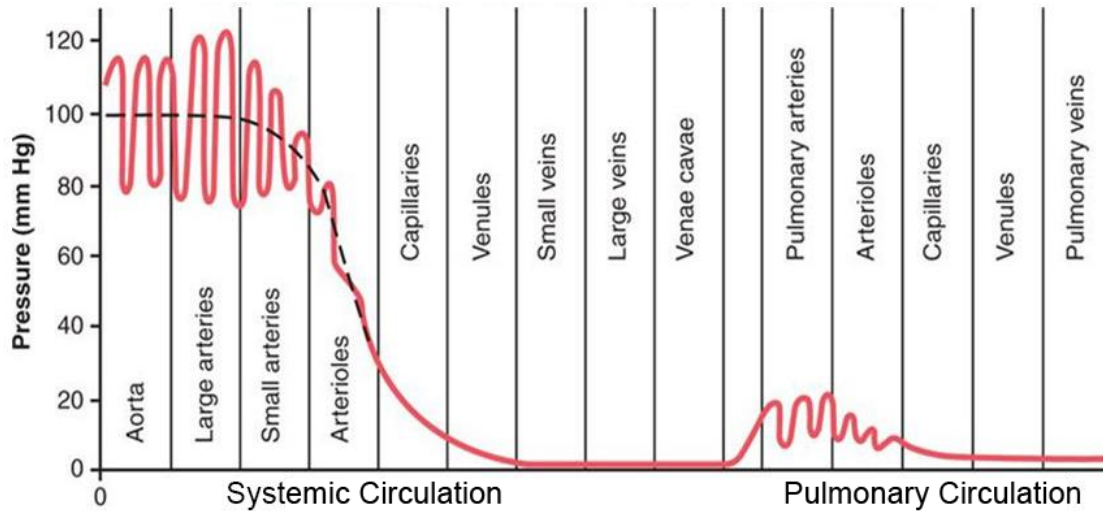


Figure 1.2 Schematic of blood pressure along the systemic and pulmonary circulations².

1.2 Hemodynamics and cardiovascular disease

Alterations in hemodynamics – the dynamics of blood flow – have been linked to the progression of pediatric CVDs, such as pulmonary arterial hypertension [2], renovascular hypertension [3], and hypoplastic left heart syndrome [4]. Altered hemodynamics drive numerous adaptations in the cardiovascular system, such as the thickening of blood vessels [5], constriction of small resistance vessels [6], [7], stiffening and dilation of the central arteries [8], [9], ventricular hypertrophy [10], [11], and affect ventricular-arterial coupling [12]. These adaptations occur to maintain an adequate blood flow to maintain the body’s metabolic demands, but often come at a cost. These adaptations typically only increase arterial pressures or ventricular volumes further, which aggravate the respective disease. Therefore, an improved understanding of the role of hemodynamics in CVD would help guide better treatment. To this end, computational models can play a crucial role in improving our understanding of CVD [13]–[15].

² Image: <https://doctorlib.info/physiology/textbook-medical-physiology/14.html>

1.3 Pediatric cardiovascular disease

Pediatric CVD is a broad term that can refer to a wide range of pathological conditions in the cardiovascular system in children. Pediatric CVD affects 3%-5% of children [16] and is one of the leading causes of infant mortality [17]. In some pediatric CVDs, treatment decisions are extrapolated from adult data due to a limited number of pediatric clinical trials [18], [19]. Therefore, there is a pressing need to improve the clinical management of these patients, particularly since children are more susceptible to the long-term catastrophic complications of CVD, such as myocardial infarction or stroke.

1.3.1 Clinical management

Innovations in treatment strategies for pediatric CVD have improved patients' mortality, morbidity, and quality of life, although the incidence of residual disease remains high [20]. Clinical management of CVD heavily relies on acquiring patient-specific data from diagnostic tools such as MRI and catheterization to measure anatomy, flow, and pressure. Patient-specific hemodynamic data is subsequently compared to values established in empirical clinical studies using large groups of patients with similar pathologies. This helps the clinical team stratify patients according to disease severity and can inform clinical decisions, such as altering drug therapy or surgical approaches.

1.3.1.1 Surgical interventions

Pediatric CVDs caused by defects to the structure of the cardiovascular system, such as abdominal aortic coarctation or hypoplastic left heart syndrome, require surgery to ameliorate the hemodynamic effects of these defects. Depending on the severity of the defect, surgical interventions may be necessary to guarantee patient survival. Surgical planning decisions,

however, are often based on the experiences of large-scale institutions with significant surgical expertise in the given disease. These decisions are, therefore, informed by population-based outcomes, which can fail to consider patient variability even in patients with similar pathologies and can vary from institution to institution [18], [21].

1.4 Computational modeling

Computational modeling has numerous applications in the study of cardiovascular disease, ranging from improving non-invasive disease diagnosis to evaluating the design of different surgical alternatives. This section will discuss the main applications used in this work.

1.4.1 Investigating the effects of hemodynamics in CVD

Thanks to technological advancements in diagnostic tools, the increasing level of detail in clinical data enables the construction of complex models that output hemodynamic metrics with higher spatial and temporal resolution than those obtained with currently available diagnostic tools [22], [23]. These models can leverage information from population-based studies to inform physical and physiological relationships that cannot be uniquely set with patient-specific data. These well-informed models can yield insight into the underlying hemodynamic mechanisms contributing to CVD [24].

Computational modeling provides high-resolution estimates of hemodynamic metrics, such as flow and pressure, which has sparked interest in the clinical field and led to continual collaborations between modeling researchers and clinical teams. However, the design of these models, including adequate boundary condition design, is a complex, case-specific endeavor that ultimately depends on the availability of clinical data and the clinical problem at hand. Therefore,

scientific researchers and clinicians must collaborate to understand the viability of the proposed methods and ensure that these methods adequately address the goals of the proposed studies [25].

Computational modeling has been used extensively to study the relationship between hemodynamics and different CVDs. In [26], computational modeling was used to evaluate the capacity of multiple hemodynamic metrics in predicting arterial stiffness, which is an initiator and indicator of CVD [27]. Computational modeling revealed that out of the evaluated metrics, carotid-femoral pulse wave velocity was the only weakly correlated metric with arterial stiffness, even though it is commonly used in the clinic as a surrogate for arterial stiffness [28], [29]. Computational modeling has been used to help to analyze wall shear stress patterns in patients with pulmonary arterial hypertension (PAH) [30]. This study revealed that patients with PAH have a decreased wall shear stress in the large pulmonary arteries, but an increased wall shear stress in the distal small pulmonary vessels. Overall, computational studies have helped uncover mechanical stimuli that are contributing to numerous CVDs, such as pulmonary hypertension [23], [31], aortic coarctations [32], [33], and hypoplastic left heart syndrome [34], [35].

1.4.2 Patient stratification

Improvements in diagnostics have elucidated a growing variability in patient pathophysiology, leading researchers to stratify patients into an increasing number of subgroups [36]. This limits the utility of a “one size fits all” approach and motivates a shift from empirical clinical studies using large groups of patients to a personalized approach. Personalized, or patient-specific, computational models leverage clinical data to study the relationship between patient-specific hemodynamics and CVD pathophysiology and can yield metrics to assess disease severity in a given patient. These metrics can subsequently be used in isolation or in combination with other metrics to stratify patients accordingly and inform clinical care.

The use of computational models for patient stratification is still in its infancy as computational models, and their prognostic metrics, require extensive validation efforts. However, in some CVDs such as coronary artery disease, computational modeling has played a large role in patient stratification. CFD models are used to assess the severity of a coronary artery stenosis by virtually estimating fractional flow reserve [37], [38], a key index for risk stratification, to stratify patients and guide surgical decisions. CFD-derived fractional flow reserve has been proven to improve patient outcomes when compared to imaging techniques [39] and has even been approved by the FDA for coronary artery disease management [40]. As computational modeling tools continue to be used for the study of pediatric CVD, model-derived hemodynamic metrics with prognostic value will continue to be identified and validated. Consequently, modeling will play a larger role in predicting prognosis of pediatric CVDs and stratifying patients.

1.4.3 Surgical planning

Surgeries used in the treatment of pediatric CVD aim to restore blood flow to compromised parts of the cardiovascular system. Predicting surgical outcomes can be difficult due to an inability to capture the specific effects that the planned surgery would have on hemodynamics. This issue is accentuated in pediatric patients due to additional considerations such as vascular and cardiac growth [41]. Therefore, clinicians must supplement their current surgical planning workflow to improve the prediction of surgical outcomes.

Computational hemodynamic modeling presents excellent promise in enhancing cardiovascular surgical planning, as it can directly inform the surgeon of the expected hemodynamic changes caused by the proposed surgery. Modeling helps surgeons understand the effect of the proposed intervention on variables such as flow distribution [42], [43], kinetic energy losses [44], and wall shear stress [45]. Furthermore, modeling is the only method that can quantify

the effect of multiple intervention alternatives to help identify an optimal solution that improves the considered hemodynamic metrics.

Surgical planning via computational hemodynamic modeling has been used considerably in patients with CVD. In [46], computational modeling was used to compare the hemodynamic efficiency of different surgical options in several anatomical locations in a cohort of 12 pediatric patients. The ultimate goal of these surgical planning efforts was to determine the optimal surgical strategy that balanced hepatic flow distribution and prevented the progression of pulmonary arteriovenous malformations. Another important application for computational modeling is to evaluate different stent designs and configurations in proposed endovascular interventions. In [47], computational modeling was used to determine the optimal stent size used to repair a complex aortic recoarctation. In [48], different endograft designs for Zone 0 aortic arch endovascular repair were evaluated and significant differences in hemodynamic performance were found between these designs. These studies demonstrate that computational modeling can provide key insights that improve planning of surgical interventions.

1.5 Diseases of interest

Pediatric CVD is comprised of a wide range of diseases with varying symptoms, etiologies, and comorbidities, which could motivate a countless number of computational modeling studies. While the tools used in this work could be applied to the study of many CVDs, this work focuses on three: pulmonary arterial hypertension, renovascular hypertension caused by an abdominal aortic coarctation, and hypoplastic left heart syndrome. In this section, we discuss the individual needs of each disease that will be addressed in this work.

1.5.1 Pulmonary arterial hypertension

Pulmonary arterial hypertension (PAH), defined by a mean pulmonary arterial pressure greater than 20 mmHg [49], is a complex, progressive disease that causes functional and structural changes in the pulmonary circulation and right ventricle (RV). Increases in pulmonary arterial pressures lead to structural remodeling and increased contractility of the RV to maintain typical cardiac outputs and meet metabolic demands [50]. Throughout the progression of PAH, the contractility of the RV increases until the ventricle can no longer compensate for further increases in pulmonary pressures. Consequently, RV stroke volume and ejection fraction decrease, which can ultimately cause decompensated RV failure [12]. Given that ventricular-arterial interactions are a crucial determinant of the clinical course of PAH [51], there is a pressing need to identify metrics that consider these interactions to describe PAH pathology accurately. Towards this goal, we will use high-resolution models of the central components of the cardiopulmonary circulation – LV, RV, large systemic and pulmonary arteries – to capture ventricular-arterial hemodynamics and their interactions.

Assessing risk and stratifying PAH patients is difficult since they tend to have varying etiologies, lesions, and symptoms. Parameters derived from clinical data, including invasive and non-invasive variables, are used individually to stratify patients and predict outcomes [52]–[54]. While these parameters help predict outcomes in these patients at a large scale, PAH progression is mainly driven by the patient’s hemodynamic conditions, which cannot be highly resolved with current diagnostic modalities. Understanding detailed hemodynamics in a given patient can provide insights into disease progression. To this end, high-resolution computational models of the ventricles and arteries can output hemodynamic metrics to help in PAH patient stratification.

1.5.2 Renovascular hypertension caused by an abdominal aortic coarctation

Renovascular hypertension is a rare, secondary form of hypertension driven by the renin-angiotensin-aldosterone system [55], [56]. It is typically caused by a narrowing of the renal arteries or the abdominal aorta, commonly referred to as an abdominal aortic coarctation [57]. When an anatomical narrowing restricts flow being delivered to the kidneys, the renin-angiotensin-aldosterone system (RAAS) increases the secretion of renin, which gets converted to angiotensin II and aldosterone, to increase renal perfusion. This response relies on increasing vasoconstriction, cardiac contractility, and blood volume, which all contribute to an effective increase in arterial blood pressure.

A common issue with this disease is that even when patients undergo successful surgery, where the anatomical narrowing is repaired and renal perfusion pressure is restored, nearly half of these patients require antihypertensive medication postoperatively [58]–[60]. However, our current understanding of the RAAS fails to explain this persistent hypertension. Therefore, unknown hemodynamic mechanisms might trigger the RAAS and contribute to the persistence of renovascular hypertension. In this thesis, we aim to explore these hemodynamic mechanisms by leveraging diagnostic data and computational modeling.

1.5.3 Hypoplastic left heart syndrome

Hypoplastic left heart syndrome is a severe, congenital CVD in which newborns have malformations of the heart's structure. The defects in the hearts of these children are as follows: the left heart is underdeveloped with significant hypoplasia of the left ventricle, aortic and mitral valves, and ascending aortic arch. In some of these patients, an atrial septal defect (hole connecting the left and right atria) is also present. These malformations prevent these children from being able to deliver blood to the systemic circulation effectively.

In healthy patients, the left ventricle supplies oxygen-rich blood to the systemic circulation whereas the right ventricle supplies de-oxygenated blood to the pulmonary circulation. However, in HLHS patients, the right ventricle, typically the weaker ventricle, is solely responsible for pumping blood that flows through both the pulmonary and systemic circulations since the left ventricle is not functional.

During the first few days of life for an infant with HLHS, oxygen-rich blood has to bypass the hypoplastic left heart via the pulmonary circulation and through the patent ductus arteriosus to reach the distal systemic circulation. However, since the patent ductus arteriosus is bound to close (as it typically does in any infant), these patients require a staged reconstruction surgery, where the first surgery is conducted during the first week of a patient's life, to "normalize" their cardiovascular system and ensure survival [61]. These staged surgeries ensure that the systemic circulation receives oxygenated blood while the pulmonary circulation receives deoxygenated blood. A detailed account of the treatment of hypoplastic left heart syndrome, including a description of each surgical stage, pre-, intra-, and post-operative considerations, and complications is provided in [61].

While these surgeries have significantly improved patient mortality and morbidity [62], these patients are far from having a normally functioning cardiovascular system since all of the blood is pumped by the right ventricle, which is typically the weaker ventricle. Therefore, these patients present various complications, such as exercise intolerance, arrhythmias, and protein-losing enteropathy (amongst others). Hemodynamic alterations are believed to contribute to these complications, which has motivated numerous computational studies [43]. The variability of these complications poses new, highly-specific considerations in guiding the care of these patients and

motivates the use of patient-specific computational models to determine optimal treatment strategies.

1.6 Structure of Thesis

In this dissertation, we combine patient-specific computational modeling with clinical data to study hemodynamics in pediatric CVD, providing insight into disease pathophysiology, aiding in patient stratification, and optimizing treatment strategies. The structure of this thesis, including an overview of the remaining chapters, is detailed below:

- **Chapter 2: Background.** The foundational background of the functional cardiovascular metrics and methods referenced in the remainder of this thesis are detailed.
- **Chapter 3: Multi-scale, multi-physics, closed-loop modeling to study PAH pathophysiology and patient stratification.** Multi-scale closed-loop models of the (A) arteries and (B) ventricles were constructed and calibrated to study PAH pathophysiology. The relationship between computational and clinical metrics with disease severity was assessed to aid in patient stratification.
- **Chapter 4: Hemodynamic mechanisms contributing to renovascular hypertension.** A case study was conducted on a 9-year-old patient with a surgically-repaired abdominal aortic coarctation with postoperative renovascular hypertension. Computational modeling was used to investigate renal hemodynamics in this patient before and after surgical intervention.
- **Chapter 5: Interventional planning for endovascular revision of a Lateral Tunnel Fontan.** A case study was conducted on a hypoplastic left heart syndrome patient that had undergone all three stages of Fontan reconstruction surgery and had postoperative complications: elevated venous pressures and hepatic venous reflux. The patient was being

considered for an endovascular intervention to treat these complications. A computational model was constructed to study the impact of the planned endovascular intervention on the patient's hemodynamics.

- **Chapter 6: Conclusions.** The contributions and critical findings of the main projects in this thesis are summarized. Future directions of these projects are also presented.

Chapter 2 Background

The aim of this chapter is to provide an overview of metrics and methods that will be used in this thesis. First, metrics that measure the function of the heart, arteries, and their interactions (i.e., ventricular-arterial coupling) will be introduced. We will also be covering how these metrics can be used to study CVD. Subsequently, the methods related to constructing patient-specific computational arterial and ventricular models used to output these metrics will be introduced. Overall, this chapter aims to lay out foundational physiology and technical background for this doctoral work.

2.1 Arterial hemodynamics

The cardiac cycle, the period of time required for a single heartbeat, is composed of two important phases: systole and diastole. Systole is defined as the period of ventricular contraction, whereas diastole is defined as the period in which the ventricles relax and fill up with blood. Systolic pressure represents the maximum arterial pressure, whereas diastolic pressure represents the minimum arterial pressure. Pulse pressure is the subtraction of systolic and diastolic pressure, and mean arterial pressure is the temporal average throughout a cardiac cycle.

The most common method of measuring blood pressure in the clinic is using a cuff, where systolic and diastolic pressures are measured in the brachial artery. These brachial pressures can be used to estimate central arterial pressures [63]–[65] and provide insight on central arterial hemodynamics. However, the accuracy of these estimations can be affected by the medication used to treat CVD [66]. Therefore, catheterizations should be conducted in CVD patients that necessitate a strong description of localized hemodynamics. For example, in patients with aortic

coarctations, catheterizations are used to measure the trans-coarctation pressure drop which is a key indicator of its severity [67], [68]. Furthermore, catheterizations are required to measure pressures in regions of the vasculature that cannot be accessed superficially such as the pulmonary circulation and systemic veins, which are essential to study PAH and HLHS.

Cardiac output is the rate of blood being pumped through the heart into the major arteries, typically measured in liters per minute. In the clinic, cardiac output is generally measured either with phase-contrast magnetic resonance imaging (PC-MRI) or echocardiography at the ascending aorta and main pulmonary artery. While a typical cardiac output range for healthy adults is 5-6 L/min [69], cardiac output varies greatly in children, where it depends on the child's weight, height, and body surface area [70]. Central arterial hemodynamics should be measured directly in pediatric patients to adequately inform computational models.

2.1.1 Disease and arterial stiffness

Central arterial stiffness is both a cause and consequence of hypertension, driven by a positive feedback loop between arterial stiffness and blood pressure [71]. As shown in **Figure 2.1**, increases in arterial blood pressure cause an increase in stress on the arterial wall, which is mediated by increases in wall thickness. Increases in wall thickness lead to an increase in structural stiffness of the arterial wall. An elevated structural stiffness increases blood pressure and accelerates disease progression. Structural changes, such as dilation of the central arteries, constriction of the small resistance arteries, and reduced compliance of the central arteries (i.e., increased stiffness), occur as a result of hypertension or CVD [72], [73].

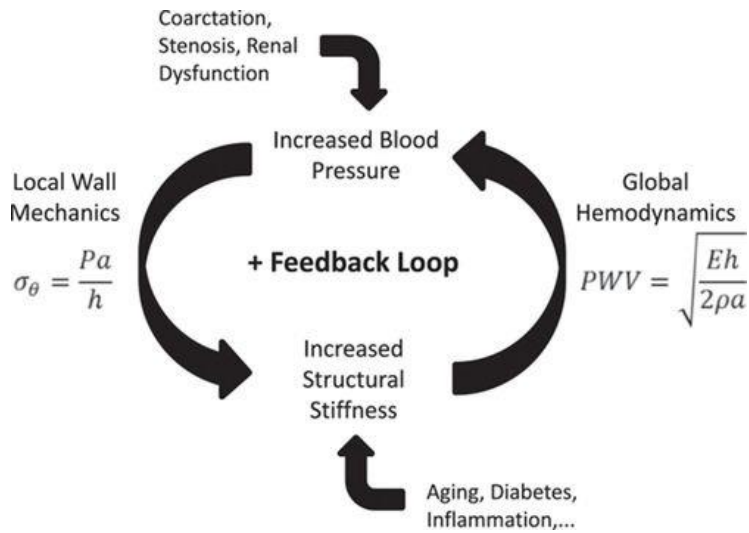


Figure 2.1 Positive feedback loop between local wall mechanics and global hemodynamics that describe the relationship between hemodynamics and disease. Increases in pressure (consequent of CVD) cause increases in stiffness, and vice versa. Adapted from [71].

2.2 Ventricular hemodynamics

The properties of the ventricle vary with time, depend on the phase of the cardiac cycle, and can be described using a pressure-volume loop. A pressure-volume loop describes the instantaneous relationship between ventricular pressure and volume waveforms. As shown in **Figure 2.2**, a PV loop is composed of four phases: (A) filling (diastole), (B) isovolumetric contraction (systole), (C) ejection (systole), and (D) isovolumetric relaxation (diastole). Point 1 on the PV loop represents the start of the isovolumic contraction (i.e., when the mitral/tricuspid valves close). Point 2 represents the start of the ejection phase, which takes place when the aortic/pulmonary valves open and blood gets pushed out of the ventricles into the central arteries. Therefore, since the aortic/pulmonary valves open at Point 2, this is also deemed as the systemic/pulmonary arterial diastolic pressure. Point 3 represents end-systole, which is the point of end-systolic pressure (P_{es}) and volume (ESV), maximum elastance, and the start of the isovolumetric relaxation. Lastly, Point 4 represents the mitral/tricuspid valves opening, and kicks off the filling phase where blood moves from the atria into the ventricles.

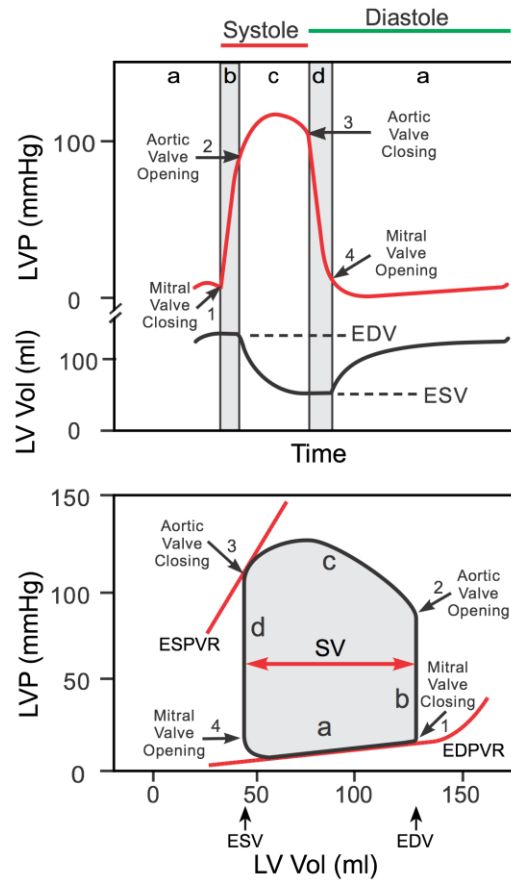


Figure 2.2 Top: Pressure and volume waveforms of the left ventricle. Bottom: Pressure-volume loop of the left ventricle, with the four phases, end-systolic and end-diastolic pressures, volumes, and pressure-volume relationships³.

2.2.1 Ventricular function

A PV loop is a tool to measure ventricular function and can be used to obtain several parameters of physiologic importance. The maximum (end-diastolic) volume and minimum (end-systolic) volume can be subtracted to derive the stroke volume, which represents the amount of blood ejected in each cardiac cycle. Cardiac output can also be derived by multiplying stroke volume (from ventricular segmentations) and measured heart rate. Ejection fraction, a measure of how efficient the ventricles are at pumping blood, is derived by dividing the stroke volume over

³ Image: <https://www.cvphysiology.com/Cardiac%20Function/CF024>

the end-diastolic volume. Ventricular volumes tend to be higher in the right ventricle than in the left ventricle, leading lower values of ejection fraction in the right ventricle [74].

End-systolic pressure-volume relationship (ESPVR), or end-systolic elastance (E_{es}), is a load-independent measure of ventricular contractility, which depends on the mass of the ventricle and the contractile force of cardiomyocytes. ESPVR can be measured by altering venous return (preload), which causes the PV loops to shift, and drawing a line through the end-systolic PV values (top-left corner of the PV loops) (**Figure 2.3**). Measuring ESPVR is rarely done in the clinic due to the risks associated with simultaneously altering venous return (preload) and invasively measuring ventricular pressure. Therefore, we rely on information from carefully-controlled experimental studies that cannot be replicated in pediatric patients [75]–[77]. Alternatively, we can virtually estimate these quantities using computational modeling [78], [79]. The end-diastolic pressure-volume relationship (EDPVR) line describes the diastolic filling of the ventricle. The mechanical properties of the relaxed ventricle (i.e., shape, wall thickness, etc.) determine the shape of the EDPVR line.

Preload is the load on the myocardium before systole begins. Ventricular preload can be measured in various ways, such as end-diastolic pressure and volume, end-diastolic stress, and end-diastolic strain. A right heart catheterization (RHC) can be performed to estimate preload in both ventricles. LV and RV preload can be estimated by pulmonary capillary wedge and central venous pressure, respectively, which are both measured during an RHC.

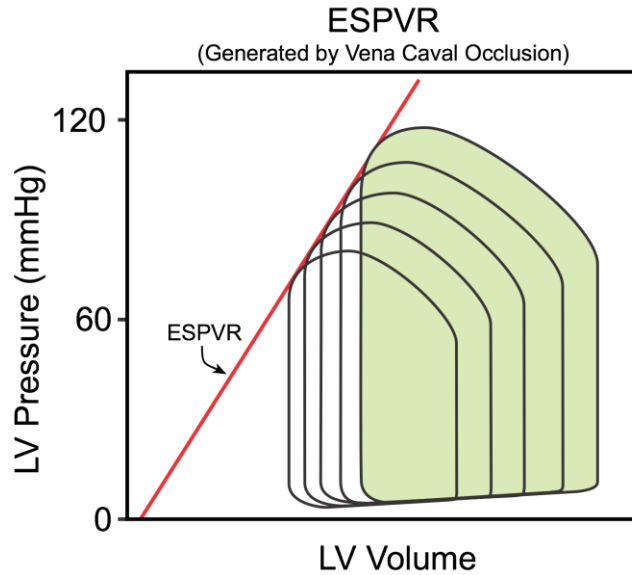


Figure 2.3 Derivation of ESPVR by altering preload via vena cava occlusion⁴.

Afterload is the load the arterial system imposes on the myocardium during ejection. Afterload can be measured in various ways, such as systemic/pulmonary arterial pressures, total arterial resistance, and peak myocardial stresses. In a PV loop, the afterload is derived as the ratio between end-systolic pressure and stroke volume. PV loops can be used to understand how ventricular function is affected by changes in preload, afterload, and contractility.

2.2.2 Changes in ventricular function

Contractility, preload, and afterload are interdependent variables that provide insight into ventricular function. The relationship between preload, afterload, and contractility is complex, where changes in one will lead to changes in the others. Therefore, it is essential to understand how changing one of these variables in isolation affects ventricular function.

Changes in contractility, also known as inotropy, can be caused by disease, exercise, remodeling, etc., and are positively correlated with changes in stroke volume (**Figure 2.4A**). A

⁴ Image: <https://www.cvphysiology.com/Cardiac%20Function/CF024>

change in preload can be achieved by altering venous return or venous pressure. For example, a patient with pediatric pulmonary hypertension can have elevated pulmonary venous pressures which increase LV preload. A change in preload drastically changes the shape of the PV loop, significantly affecting ventricular volumes and systolic pressures (**Figure 2.4B**). Lastly, changes in afterload, which are most directly related to arterial disease (i.e., hypertension), lead to changes in ventricular end-systolic volumes and pressures (**Figure 2.4C**).

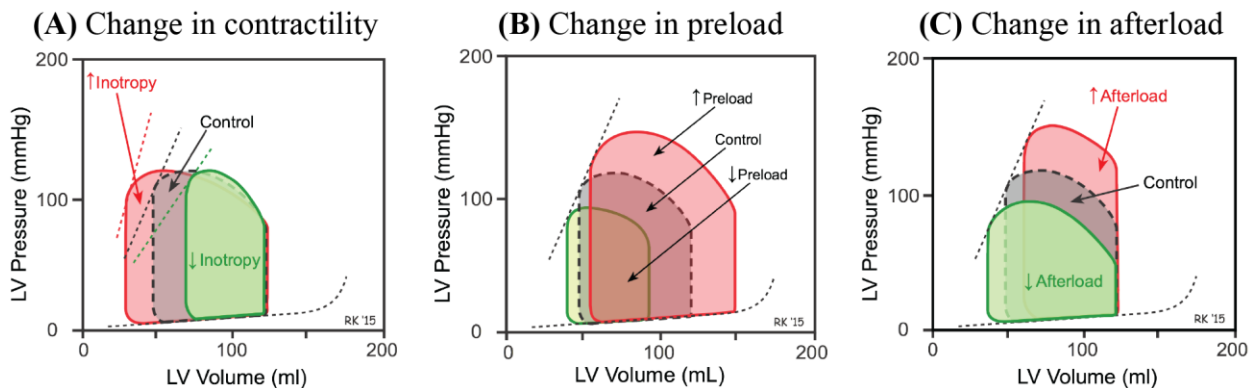


Figure 2.4 Changes in (A) contractility, (B) preload, and (C) afterload lead to affect the pressure-volume relationship⁵.

2.3 Ventricular-arterial coupling

Arterial and ventricular functional metrics are of strong interest in the clinic, since homeostatic values of blood pressure, cardiac output, and ventricular contractility are all essential for the cardiovascular system to continue operating in physiologic conditions. These metrics are heavily intertwined; changes in either of these metrics lead to changes in the others, which is a phenomenon referred to as “ventricular-arterial coupling”. It is important to develop a strong understanding of how ventricular and arterial function interact to adequately study the pathophysiology of pediatric CVD, including pulmonary arterial hypertension.

⁵ Image is adapted from: <https://www.cvphysiology.com/Cardiac%20Function/CF025>

Ventricular-arterial coupling can be characterized as the ratio between ventricular contractility (or end-systolic elastance (E_{es})), and arterial load (or arterial elastance (E_a)), which is also referred to as afterload (**Figure 2.3**). When faced with an increase in arterial load (due to pediatric CVD), the ventricle increases its contractility to maintain a physiologic level of cardiac output, satisfying the body’s oxygen demands and ensuring a highly efficient energy transfer between the ventricle and arteries (**Figure 2.3, green**). As the disease progresses further, the contractility of the ventricle can no longer compensate for further increases in arterial load, leading to “uncoupling” between the ventricle and the arteries and eventual heart failure (**Figure 2.3, purple**). A “coupled” ventricle preserves stroke volume and systolic function, and maintains normal filling pressures, whereas an “uncoupled” ventricle is dilated with a reduced stroke volume, has impaired systolic function, and elevated filling pressures [12], [50].

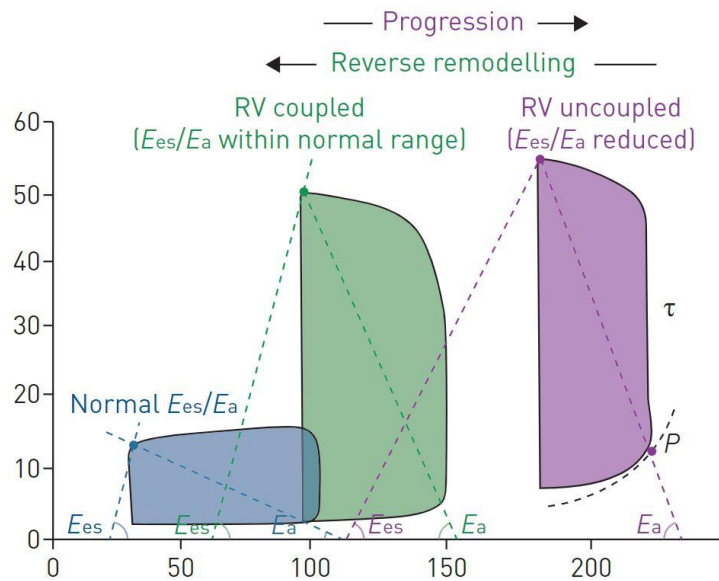


Figure 2.5 PV loops at three different stages: healthy (blue), diseased but coupled (green), diseased and uncoupled (purple), which is progressing towards ventricular failure. Adapted from [50].

While ventricular-arterial coupling is a key factor in many cardiovascular diseases, it is underutilized in clinical and research settings. Single-beat methods have been developed to

measure ESPVR without requiring altering preload [80], [81]. While these methods have been useful in yielding additional insight on ventricular-arterial coupling, they rely on some simplifications and have not been extensively validated in patients with severe disease [12]. To overcome these hurdles, we leverage computational modeling to virtually alter preload in a calibrated model and derive a patient-specific ESPVR value. This can then be used to yield insight into ventricular-arterial coupling in said patient.

2.4 Computational modeling

CVD causes changes in cardiovascular anatomy, structure, and function, in both the arteries and ventricles. A comprehensive understanding of these changes, which can be investigated in detail with computational modeling, is essential to improve our understanding of pediatric CVDs and their management. In this section, we aim to provide an overview of the computational modeling methods to achieve the key goals of this thesis, which are detailed in Chapter 1.

2.4.1 Central pulmonary and systemic arterial modeling

Computational fluid dynamics (CFD) is used to model blood flow in the arteries, where the incompressible Navier-Stokes equations are solved to characterize the 3-dimensional hemodynamics. The weak, or integral, form of the Navier-Stokes equations was solved using the finite element method within the open-source cardiovascular modeling software CRIMSON [82]–[84]. This numerical framework is used to solve partial differential equations of the Navier-Stokes equations in a discretized geometric domain, such as an unstructured mesh containing linear tetrahedral elements [85].

After construction of the geometric model and generation of a discretized mesh, boundary conditions and modeling assumptions must be specified. Boundary conditions need to be specified

in the inflow faces, outflow faces, and arterial walls of the geometric model. In the outflow faces, one of the most commonly used boundary conditions in arterial hemodynamics is the reduced-order 3-element Windkessel model [86], which captures the hemodynamic behavior – resistance and compliance – of distal vasculature.

For the inflow boundary condition, flow can be directly prescribed into the inlet of the model. However, this can lead to unphysiological hemodynamic behaviors since any change performed on the model, such as an introduction of a stenosis or changes in parameter values, will not affect the flow entering the geometric model. To overcome this, a lumped-parameter heart model can be coupled to the inlet face(s) of the 3D arterial model to capture the hemodynamic behavior of the heart. The lumped-parameter heart model, first introduced in [87], is driven by an elastance function which is derived from PV loops. Therefore, the relationship between pressure and volume is driven by the shape of the elastance waveform without directly prescribing either one. This allows us to capture the effects of parameter changes (i.e., autoregulation) [84], [88] or anatomical changes (i.e., surgical interventions) [89], [90] on central arterial hemodynamics more accurately. Of note, the use of a lumped-parameter heart model enables us to capture interactions between the ventricles and arteries.

Many 3D arterial models apply a no-slip boundary condition to the arterial wall, which models them as rigid structures. This modeling assumption is done to simplify the problem, but it prevents the researcher from studying the well-documented relationship between arterial stiffness and CVD. While this might not be important in specific CVDs, one could argue that capturing the arterial stiffness and motion would provide more physiologically accurate results even in problems where stiffness is not the central priority. Fluid-structure-interaction methods, such as the coupled momentum method [82], allows us to model the arterial wall as a deformable material. The

material properties of the arterial wall – thickness and stiffness – can be derived from patient-specific data on pressure and luminal area changes [91], [92].

Model validation involves iteratively calibrating model parameter until simulated results match clinically-measured data [93]. Following validation, models can be used to study disease-associated hemodynamics in depth. Models can also be modified to represent either disease progression or a proposed surgical intervention and measure their effects on arterial hemodynamics.

2.4.2 Ventricular modeling

Multi-scale, closed-loop biventricular models can be used to simulate hemodynamics and mechanics to study pediatric CVD. In these models, 3D governing equations are based on a quasi-static formulation and assume that the cardiac tissue behaves as an incompressible material [78], [79], [94], [95]. The LV and RV are represented using the finite element method and the 3D governing equations are solved using the open-source software FEniCS [96]. The mechanical behavior of a 3D biventricular model is described by an active stress formulation. In this active stress formulation, the stress tensor can be decomposed into active and passive stress components, represented with active contraction models and passive constitutive models, respectively.

Cardiac tissue is known to be an orthotropic, viscoelastic material [97], [98]. Numerous passive constitutive models have assumed a hyper-elastic orthotropic behavior [99]–[101], and some have included viscoelasticity [102]–[104]. Orthotropic viscoelastic models can better represent ventricular biomechanics, at the expense of a larger number of model parameters. For the sake of simpler model parameterization, in this work we have opted for a phenomenological transversely isotropic hyper-elastic model [95], [105].

The choice of active contraction constitutive models in ventricular biomechanics depends on the needs of the study [106]–[110]. Complex active contraction models that consider tropomyosin kinetics [111] or crossbridge cycling [109] can accurately capture ventricular active mechanics at the expense of more model parameters. However, the modified Guccione active contraction model [107] used in this work is computationally efficient, captures a wide range of myocardial responses, and successfully reproduced clinical data that satisfied the needs of our study.

A lumped-parameter circuit is used to represent the systemic and pulmonary circulations. Resistances and compliances represent the arterial and venous segments, whereas resistances and diodes represent the valves. The atria can be modeled using a time-varying elastance model [112]. Circulatory model parameters, active contraction parameters, and passive stiffness parameters are all calibrated until simulated and clinically-measured PV loops and arterial pressures are matched. After calibration, ventricular models can be used to understand the effects of pediatric CVD on ventricular function including preload, afterload, and contractility.

Chapter 3 Multi-Scale Closed-Loop Modeling Framework to Study PAH Pathophysiology

3.1 Original publication information

This chapter was originally published as a scientific article:

Tossas-Betancourt, C., Li, N. Y., Shavik, S. M., Afton, K., Beckman, B., Whiteside, W., Olive, M. K., Lim, H. M., Lu, J. C., Phelps, C. M., Gajarski, R. J., Lee, S., Nordsletten, D. A., Grifka, R. G., Dorfman, A. L., Baek, S., Lee, L. C., & Figueroa, C. A. (2022). Data-driven computational models of ventricular-arterial hemodynamics in pediatric pulmonary arterial hypertension. *Frontiers in Physiology*, 13. <https://doi.org/10.3389/fphys.2022.958734>

Changes made to the original document are mainly cosmetic to adhere to the format of this document.

3.2 Introduction

Pulmonary arterial hypertension (PAH), defined by a mean pulmonary arterial pressure greater than 20 mmHg [49], is a complex disease that causes functional and structural changes in the pulmonary circulation and right ventricle (RV). Ventricular-arterial interactions play an important role in the progression of PAH, where increases in resistance and decreases in compliance of the pulmonary circulation lead to structural remodeling and increased contractility of the RV, in an attempt to maintain normal cardiac outputs [50]. RV contractility can increase four- to five-fold until the ventricle cannot compensate for further increases in pulmonary

pressures, leading to “uncoupling” between the RV and pulmonary arteries. Consequently, RV stroke volume and ejection fraction decrease, ultimately leading to decompensated RV failure [12]. Given that ventricular-arterial interactions are a key determinant of the clinical course of PAH [51], there is a pressing need to identify metrics that consider these interactions to accurately describe PAH pathology.

Pediatric PAH is especially difficult to manage as diagnostic metrics are often derived from adult data due to the lack of clinical trials in the pediatric population [113]. Using adult population data to guide pediatric PAH treatment can be problematic as younger subjects present significant differences in cardiovascular structure and function [114] and show worse survival rates [115]. Furthermore, there are population-based differences in children with PAH compared to adults, such as impaired lung development and higher incidence of congenital heart disease [116]. Clinical trials designed to focus on pediatric PAH patients could help elucidate novel diagnostic metrics for this population.

Computational models based on patient-specific clinical data have widely been used to study mechanics and hemodynamics of cardiovascular diseases [14], [15], [117]–[119] including hemodynamics in the cardiopulmonary circulation [120]. Previous PAH modeling efforts have focused on either the pulmonary arteries [30], [121]–[123] or the RV [94], [124], [125]. The absence of high-resolution (3D) bi-directional (ventricular-arterial) hemodynamic interactions in these models restricts their ability to capture phenomena such as ventricular-arterial uncoupling. In this work, we aim to overcome this limitation by developing high-resolution (3D) models of both RV and pulmonary artery mechanics, a first step towards a fully 3D bi-directional model of the cardiopulmonary system.

The overall goals of this work are to (**Figure 3.1**): (1) develop and calibrate multi-scale closed-loop models of the cardiopulmonary circulation in PAH patients, and (2) use clinical and computational metrics to stratify patients according to disease severity. Two different models will be developed: a “High-Resolution Arterial Model”, whereby image-based 3D fluid-structure interaction (FSI) models of the large vessels are coupled to 0D models of ventricles and distal circulation; and a “High-Resolution Ventricular Model”, whereby image-based 3D models of passive and active ventricular mechanics are coupled to 0D models of arterial and pulmonary circulation. These computational models rely on the quality and consistency of clinical data. Data were acquired using diagnostic tools with varying tolerances, temporal and spatial resolutions, and physiological states (i.e., level of sedation), which led to inconsistencies. In this work, we also propose and implement strategies to mitigate data inconsistencies to inform and calibrate these computational models.

3.3 Materials and Methods

Clinical data were acquired prospectively from a cohort of 8 pediatric PAH patients treated at the University of Michigan (UM) C.S. Mott Children’s Hospital (ClinicalTrials.gov ID No. NCT03564522). This study was approved by the UM Institutional Review Board (HUM00117706), and informed consent was obtained from subjects or their parents/guardians. World Health Organization functional class (WHO-FC) was determined for each patient.

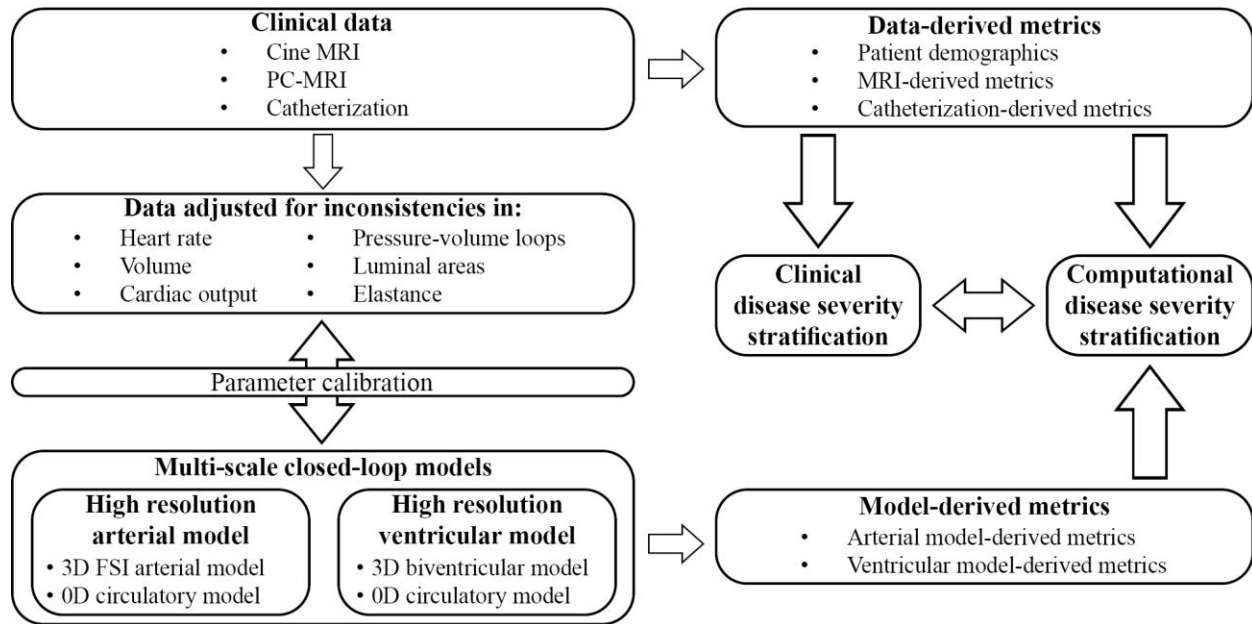


Figure 3.1 Workflow of study investigating the effects of PAH. Clinical data was acquired and adjusted to mitigate inconsistencies. Clinical and computational metrics (derived from the computational models) were used in the clinical disease severity stratification.

3.3.1 Clinical Data

Clinical data on anatomy, flow, and pressure, were acquired using MRI and catheterization. Both MRI and catheterization data were acquired with the patient at rest in the supine position. The mean time between MRI acquisition and catheterization was 4.4 days (range 0-29 days).

3.3.1.1 Magnetic Resonance Imaging

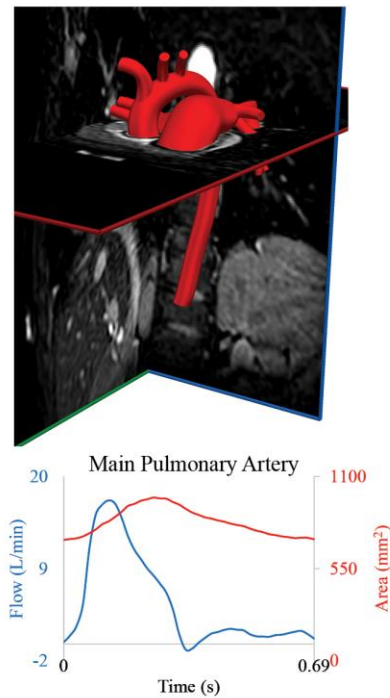
MRI was performed using a 1.5 Tesla scanner (Achieva or Ingenia; Philips, Best, the Netherlands). Three-dimensional diastolic vascular anatomy was obtained with a 3D steady state free precession (SSFP) sequence (TE: 2.2 ms, TR: 4.3-4.4 ms, flip angle: 90°, field of view: 260-350 mm, slice thickness = 1.4-1.6 mm, image resolution = 0.63-0.78 mm) with cardiac and respiratory gating (**Figure 3.2A**). Gated phase-contrast MRI (PC-MRI) (TE: 2.7-3.3 ms, TR: 4.1-5.1 ms, flip angle: 12°, field of view: 250-350 mm, slice thickness = 6 mm, image resolution = 1.4-1.6 mm) was performed to obtain dynamic data at 40 phases of luminal area and blood flow at

five anatomical locations: ascending aorta (AAo), descending thoracic aorta (DTA), main pulmonary artery (MPA), left pulmonary artery (LPA), and right pulmonary artery (RPA). Multi-slice (10-13 slices, slice thickness: 6-8 mm), multi-phase (30 phases) cine MR images (TE: 1.2-1.6 ms, TR: 2.5-3.1 ms, flip angle: 60°, field of view: 250-350 mm, image resolution = 1.6-1.8 mm) were acquired by positioning the scans in the short-axis planes perpendicular to the long-axis of the left ventricle (LV), capturing both the LV and RV from the cardiac base to the apex (**Figure 3.2B**).

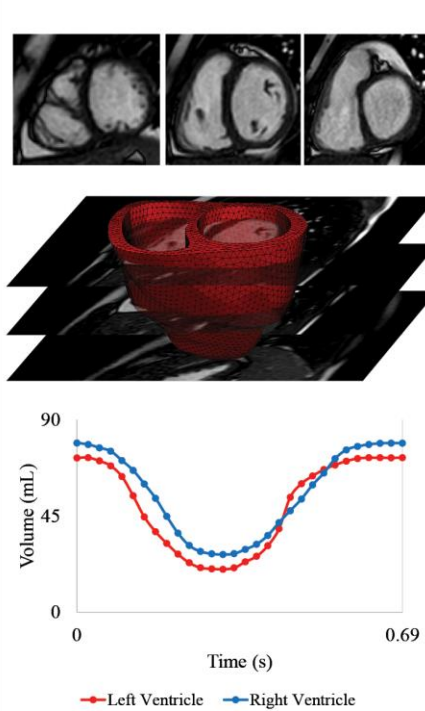
3.3.1.2 Catheterization

Right heart catheterization was performed in all subjects (**Figure 3.2C**) to measure invasive hemodynamics and assess PAH progression. Intracardiac pressures were measured in the right atrium, RV, and pulmonary arteries (MPA, and either LPA or RPA) using a balloon wedge catheter (Arrow, Reading, PA) or thermodilution catheter (Edwards Lifesciences, Irvine, CA). Pulmonary capillary wedge pressure was measured, and femoral arterial access was acquired for blood pressure monitoring and blood gas analysis. In select patients with suspected left heart disease, retrograde left heart catheterization was performed using a pigtail catheter (Merit Medical, South Jordan, UT) and direct pressures were measured in the LV, ATA, and DTA. Pulmonary vascular resistance index (PVRi) was calculated by dividing the pressure gradient (mean pulmonary arterial pressure – mean pulmonary capillary wedge pressure) over cardiac index, which was calculated by the Fick principle or thermodilution.

A. MRI - 3D SSFP & PC-MRI



B. MRI - Short Axis



C. Catheterization

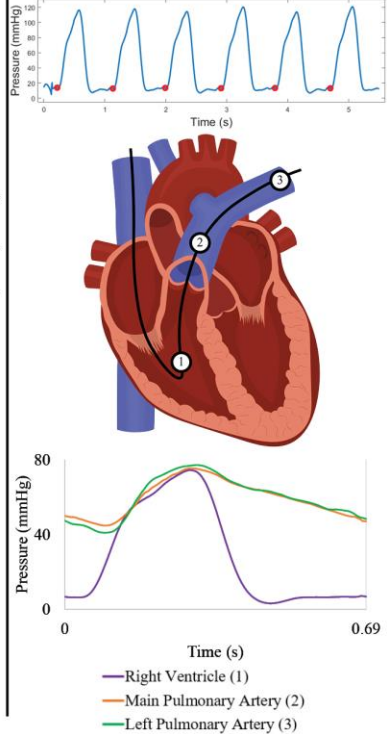


Figure 3.2 MRI was performed to acquire arterial anatomy and hemodynamics (A), and ventricular volumes (B). Catheterization was performed to acquire ventricular and arterial pressures (C).

3.3.2 Patient demographics and clinical metrics

Eight PAH patients (age: 11.8 ± 4.4 years; range 6-19 years) underwent catheterization and MRI examinations. **Table 3.1** summarizes mean and standard deviations of basic patient demographics and several key clinical metrics, derived from MRI and catheterization. Five patients were classified as WHO-FC I and three as WHO-FC II. Four patients were on dual PAH therapy, and four on triple PAH therapy.

3.3.3 Strategies for mitigation of inconsistencies in clinical data

Despite best efforts made to acquire MRI and catheterization data in close temporal proximity, the studies were on average 4.4 days apart. Furthermore, catheterization and MRI were performed under varying levels of sedation. This, together with the different tolerances and

temporal resolutions of MRI and catheterization, leads to inconsistencies in the data that must be addressed in order to use the data for simulations, where conservation laws of mass and momentum balance must be satisfied. Data inconsistencies include: (1) LV and RV volume waveforms segmented from cine MRI short-axis data do not match values obtained with PC-MRI, and (2) misaligned ventricular pressure-volume (PV) data. Additional examples of data inconsistencies are detailed in **Appendix A**.

Table 3.1 Summary of patient demographics and clinical metrics (MRI- and cath-derived).

	Subj.	Subj.	Subj.	Subj.	Subj.	Subj.	Subj.	Subj.	Std	
Patient Demographics	#1	#2	#3	#4	#5	#6	#7	#8	Avg	Dev
Age (years)	11	15	10	5	16	11	19	6	11.6	4.8
Gender (M/F)	F	F	M	F	F	M	F	F	N/A	N/A
BSA (m ²)	1.23	1.66	0.95	0.74	1.44	1.25	1.61	0.88	1.2	0.3
Height (cm)	154	175	123	106.7	152	152	165	121.9	143.7	23.8
Weight (kg)	33.2	56.3	26.9	18.7	49.8	35.2	56.2	23	37.4	14.9
WHO Functional Class	II	I	II	I	I	II	I	I	N/A	N/A
Number of PAH medications	3	2	3	2	2	3	2	3	2.5	0.5
Years since initial diagnosis	5	5	4	1	10	10	6	2	5.3	3.3
	Subj.	Subj.	Subj.	Subj.	Subj.	Subj.	Subj.	Subj.	Std	
MRI-derived metrics	#1	#2	#3	#4	#5	#6	#7	#8	Avg	Dev
Aorta - Flow Rate (L/min)	4.24	4.38	3.74	2.41	5.37	4.79	4.90	3.16	4.1	1.0
MPA - Flow Rate (L/min)	4.80	4.89	3.23	2.39	5.34	3.50	4.40	2.95	3.9	1.1
Averaged Cardiac Output (L/min)	4.52	4.63	3.49	2.40	5.36	4.15	4.65	3.06	4.0	1.0
Cardiac Index (L/min/m ²)	3.7	2.8	3.7	3.2	3.7	3.3	2.9	3.5	3.3	0.4
% of flow to LPA	45%	37%	51%	40%	47%	51%	41%	49%	0.5	0.1
Pulmonary Regurgitant Factor (%)	1%	1%	N/A	1%	1%	2%	8%	0%	2.0%	2.7%
Heart Rate (bpm)	91	77	79	66	83	74	70	73	76.6	7.7
Cardiac Cycle Length (s)	0.66	0.78	0.76	0.91	0.73	0.82	0.86	0.83	0.79	0.08
RV End-Diastolic Volume (mL)	120	141	84	78	114	123	241	90	123.9	52.1
RV End-Systolic Volume (mL)	60	67	33	39	44	60	145	39	60.9	36.1
RV Stroke Volume (mL)	60	74	51	39	71	63	96	51	63.1	17.5

RV End-Diastolic Volume Index (mL/m ²)	98	85	88	105	79	98	150	102	100.7	21.7
RV End-Systolic Volume Index (mL/m ²)	49	40	35	53	31	48	90	44	48.7	18.3
RV Stroke Volume Index (mL/m ²)	49	45	54	53	49	50	60	58	52.1	5.0
RV Ejection Fraction (%)	50	52	61	49	62	51	40	57	52.8	7.2
RV Mass (g)	30	36	23	16	35	21	72	13	30.7	18.7
RV Mass Index (g/m ²)	24	22	24	22	24	17	45	14	24.0	9.2
MPA Stroke Volume (mL)	56	63	41	37	69	48	65	41	52.5	12.4
LV End-Diastolic Volume (mL)	103	124	82	68	112	139	163	72	107.9	33.5
LV End-Systolic Volume (mL)	41	55	30	30	41	60	72	30	44.9	15.9
LV Stroke Volume (mL)	62	69	51	37	71	79	91	42	62.8	18.5
LV End-Diastolic Volume Index (mL/m ²)	84	75	86	92	78	111	101	82	88.6	12.3
LV End-Systolic Volume Index (mL/m ²)	33	33	32	41	28	48	45	34	36.7	6.9
LV Stroke Volume Index (mL/m ²)	50	42	54	50	49	63	57	48	51.6	6.4
LV Ejection Fraction (%)	60	55	63	55	63	57	56	58	58.4	3.3
LV Mass (g)	55	72	43	31	59	53	92	31	54.5	20.6
LV Mass Index (g/m ²)	45	43	45	42	41	42	57	35	43.9	6.2
Ascending Aorta Stroke Volume (mL)	53	60	51	39	73	67	78	44	58.1	13.8
Sedation	N	N	N	Y	N	Y	N	N	N/A	N/A
	Subj.	Subj.	Subj.	Subj.	Subj.	Subj.	Subj.	Subj.		Std
Cath-derived metrics	#1	#2	#3	#4	#5	#6	#7	#8	Avg	Dev
PA mean pressure (mmHg)	59.4	29.2	35.1	82.9	47.1	31.2	58.3	20.4	45.4	20.6
PA pulse pressure (mmHg)	30.6	18.0	35.4	66.2	36.9	26.6	48.0	24.1	35.7	15.3
PA systolic pressure (mmHg)	74.7	38.2	52.9	116.0	65.5	44.5	82.3	32.5	63.3	27.6
PVR Index (WU m ²)	16.2	7.3	5.9	23.2	9.9	4.9	16.0	3.3	10.8	6.9
Rp:Rs	0.8	0.4	0.32	0.77	0.55	0.33	0.8	0.2	0.5	0.2
PCWP (mmHg)	10	8	15	14	12	14	12	8	11.5	2.7
Cath Heart Rate (bpm)	69	65	78	66	72	65	66	86	71.0	7.6
Cath Cardiac Cycle Length (s)	0.87	0.92	0.77	0.91	0.83	0.92	0.91	0.70	0.9	0.1
PA Oxygen Saturation (%)	80	72	64	60	73	64	70	73	69.5	6.5

3.3.3.1 Ventricular volume waveforms

3.3.3.1.1 Ventricular volumes derived from short-axis cine MRI data

LV and RV volume waveforms were first obtained by manually segmenting each of the 30 phases of the cine MRI data using the software package CVI42 (Circle Cardiovascular Imaging, Calgary, Canada). Ventricular segmentation is a time-consuming task susceptible to inter- and intra-observer variability [126]. It required delineation of LV and RV endocardial surfaces from the apex to the mitral and tricuspid valve, respectively, for each of the 30 phases of the MRI data. In the short-axis cine MRI data, slice thickness (6-8 mm) is much larger than the in-plane image resolution (0.80-0.91 mm). Higher variability in RV segmentation is expected since its shape varies significantly throughout the slices [127], [128]. Furthermore, delineation of the basal regions of the ventricles can be challenging due to the 10-20% end-systolic shortening [129], [130] and the motion of the valves along the long-axis. Average RV and LV stroke volumes of 62.8 ± 18.5 mL and 63.1 ± 17.5 mL, respectively, were obtained.

3.3.3.1.2 Truncated ventricular volumes

A fixed plane below the tricuspid valve was used to define truncated volume data used in the high-resolution ventricular computational models. This truncation yielded average LV and RV stroke volumes of 43.0 ± 14.7 mL and 40.4 ± 14.9 mL, respectively (see **Appendix Table A.1** for values for each patient). These volumes are 31% and 36% smaller than those corresponding to the full ventricle. Then, the end-systolic phase was segmented using MeVisLab (www.mevislab.de) to define STL models of LV and RV. These end-systolic segmentations were adjusted to match the CVI42 ventricular volume data.

The discrepancy between full ventricular and truncated volumes used in the high-resolution computational arterial models is accounted for by different model parameters of the lumped

parameter heart model (Section 3.3.4.2). Conversely, the high-resolution computational ventricular models use the truncated definition of the ventricular volumes. The implications of this inconsistency will be discussed in the limitations.

3.3.3.1.3 Ventricular volumes derived from PC-MRI data

Integration of PC-MRI flow waveforms at AAO and MPA provide alternative definitions for LV and RV ventricular volume waveforms, respectively. Average PC-MRI-derived RV and LV stroke volumes of 53.8 ± 11.3 mL and 51.1 ± 10.8 mL, respectively, were obtained. This represents a difference of 19% and 23% relative to the values obtained via segmentation of the short-axis cine-MRI data. This difference could be due to patients holding their breath only for the short-axis cine-MRI sequence, which can increase stroke volume [131]. In Section 3.3.4.3.2, we describe how to combine the PC-MRI and short-axis cine MRI definitions of volume waveforms to improve the comparison between simulated and measured AAO and MPA flow waveforms.

3.3.3.2 Automated alignment of ventricular pressure and volume data

Ventricular pressure and volume waveforms were combined to form a PV loop. Given the difference in temporal resolution, pressure waveforms were down sampled to 30 phases to match the resolution of the volume data. Then, pressure and volume waveforms were aligned using the R-peaks of the ECG and a PV loop was plotted. However, in most cases, the shape of the resulting PV loop lacked defined isovolumetric contraction and relaxation phases (**Figure 3.3A**), which can even occur when PV loop data is acquired simultaneously with an interventional cardiac MRI. A biophysical heart model has been developed to align PV data [132], [133]. In this work, we developed an algorithm to systematically shift the pressure waveforms to determine optimally aligned PV loops.

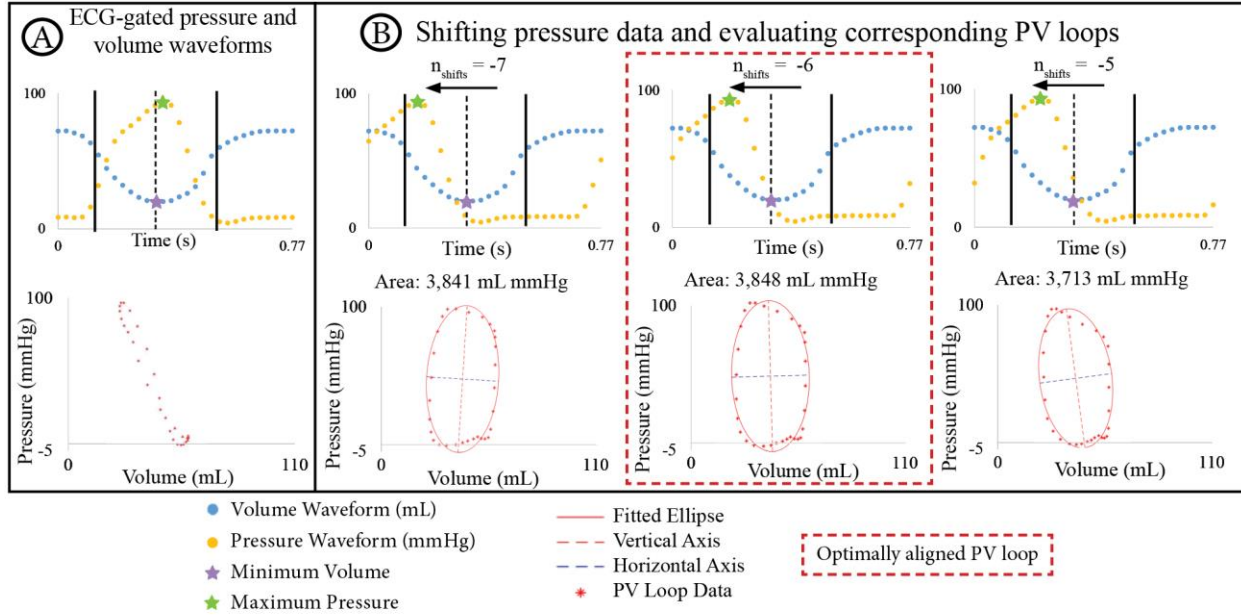


Figure 3.3 (A) PV loop built by aligning ECG-gated pressure and volume waveforms. (B) Optimization algorithm shifts data to define a new PV loop, an ellipse is fitted to each iteration. The optimally aligned PV loop is the iteration with the maximum area.

The basis of this algorithm is as follows: Pressure data was shifted by time increments $\Delta t = T/30$ s, where T is the cardiac cycle length, and 30 is the number of phases. Since maximum pressure and minimum volume must remain in close temporal proximity, the number of Δt increments (n_{shifts}) was limited to ± 7 (e.g., $n_{\text{shifts}} = \pm 1, 2, \dots, 7$). Positive and negative signs indicate forward and backwards shifting of the pressure, respectively. For each pair of volume and shifted pressure data, a new PV loop was defined, and an ellipse fitted to the data by least squares minimization [134]. The optimally aligned PV loop corresponded to the time shift which produced the fitted ellipse with the maximum area (**Figure 3.3B**). The optimization algorithm was used to determine the optimally aligned PV loops for both the LV and RV. While the choice of maximum area to identify the optimally aligned PV is arbitrary, it provides a systematic criterion to perform PV loop alignment for every subject.

The aligned PV loops were used to estimate ventricular stroke work, construct the elastance waveforms of the lumped parameter (0D) heart model used in combination with the high-

resolution arterial models (Section 3.3.4.2), and to calibrate the parameters of the high-resolution ventricular models (Section 3.3.5).

3.3.4 High-resolution arterial model

These models consist of a 3D FSI component representing the large systemic and pulmonary arteries, and 0D lumped-parameter models representing the heart (H) (see **Figure 3.4**) and the distal systemic and pulmonary circulations via 3-element Windkessel models (W) [135].

3.3.4.1 3D FSI arterial models

Anatomical models of the large systemic and pulmonary arteries were constructed from the diastolic phase of the 3D steady-state free precession MRI data, adjusted to match diastolic areas measured with PC-MRI [136], see **Appendix A**. Models were built using the open-source cardiovascular simulation software CRIMSON [85], rendering smooth analytical (NURBS) surfaces enclosing the volume of the vessels of interest. Models were then discretized into linear tetrahedral elements, and field-based adaptivity was used to refine the mesh in regions of high velocity gradients [137]. A mesh sensitivity analysis was performed to ensure mesh independence in flow and pressure waveforms, and determine the mesh sizes. The combined finite element mesh size for the aortic and pulmonary models ranged from 1,214,922 to 1,780,093 elements.

The arterial wall was modeled as a linear elastic membrane with spatially varying isotropic stiffness and wall thickness [138]. Luminal area and pressure data were used to derive linearized stiffness, defined as [91], [92]:

$$E = \frac{1.5 \cdot \Delta P \cdot R_i^2 \cdot R_o}{(R_o^2 - R_i^2) \cdot \Delta R} \quad (3.1)$$

where R_i and R_o are the diastolic luminal and outer vessel radius, respectively. $\Delta R (= R_{\text{systolic}} - R_{\text{diastolic}})$ is the variation in lumen radius, and $\Delta P = P_{\text{systolic}} - P_{\text{diastolic}}$ is the pulse pressure. A 15% ratio of wall thickness to vessel radius was used in the large systemic [139] and pulmonary [140] arteries. Linearized stiffness was assessed in the following 5 locations where arterial wall deformation was estimated using PC-MRI: AAO, DTA, MPA, LPA, and RPA. The stiffness values were then linearly interpolated along the vessel centerline. Stiffness in branches was set to match that of the closest large arterial vessel. Stiffness values in each location for each subject are detailed in **Appendix Table A.3**.

Once the parameters of 3D and 0D compartments of model are defined, multi-scale FSI simulations were performed using the CRIMSON flow solver to solve for the Navier-Stokes equations for an incompressible Newtonian fluid [83], [84], [138]. All simulations were performed using a time step size of 0.1 ms. Blood was modeled as an incompressible Newtonian fluid with density of $\rho = 0.00106 \text{ g/mm}^3$ and viscosity of $\mu = 0.004 \text{ g/mm}\cdot\text{s}$. Simulations were run until flow and pressure fields achieved cycle-to-cycle periodicity.

3.3.4.2 Lumped-parameter (0D) heart model

A lumped-parameter (0D) heart model (H) was defined using CRIMSON'S Netlist Editor Boundary Condition Toolbox [141] (**Figure 3.4**). The lumped-parameter heart model used in this work, developed by [87], captures how changes in either cardiac or arterial properties influence each other. This model was chosen as it was developed by our group, it is implemented in the CRIMSON flow solver, and it has been widely adopted by the 3D hemodynamic modeling field [88], [90], [142], [143]. Resistors (R_R) and capacitors (C_R) were used to represent the aortic and pulmonary artery roots. Mitral and tricuspid valves were modeled using diodes (D_{V1}) and inductors (L_{V1}) with set values. Aortic and pulmonary valves were modeled using dynamically controlled

resistors (R_{V2}) and inductors (L_{V2}) [144], [145]. These valve models made it possible to reproduce post-systolic flow reversal and non-zero diastolic flow, features both present in our patient cohort.

LV and RV contractility was represented via a time-varying pressure volume chamber representing ventricular elastance $E_V(t)$ and a dynamic source resistance (R_S) in series. An analytical 'two-Hill' function [144] was used to define a smooth ventricular elastance $E_V(t)$, whose parameters were adjusted to fit the clinical values of elastance $E_i = P_{V_i}/V_{V_i}$, $i = 1, \dots, 30$ defined from the optimally-aligned PV-loops for each patient (Section 3.3.3.2) (**Appendix Figure A.1**):

$$E_V(t) = k \left(\frac{g_1}{1 + g_1} \right) \left(\frac{1}{1 + g_2} \right) + E_{min} \quad (3.2)$$

where

$$g_1 = \left(\frac{t}{\tau_1} \right)^{m_1}, \quad g_2 = \left(\frac{t}{\tau_2} \right)^{m_2}, \quad k = \frac{E_{max} - E_{min}}{\max \left[\left(\frac{g_1}{1 + g_1} \right) \left(\frac{1}{1 + g_2} \right) \right]}. \quad (3.3)$$

k is a scaling factor, m_1 and τ_1 and m_2 and τ_2 control the slope and time translation of the ascending and descending portions of the elastance waveform, respectively.

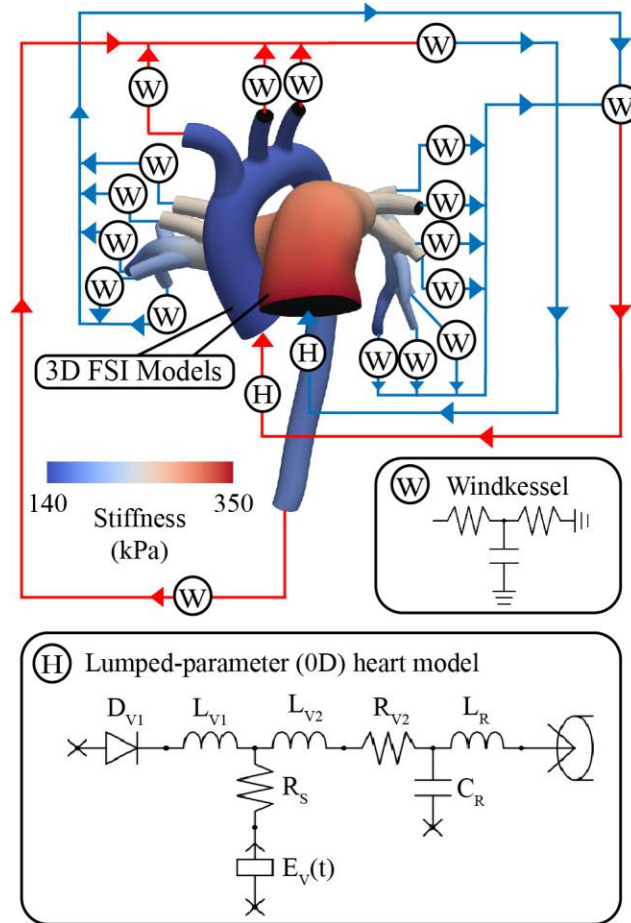


Figure 3.4 Multi-scale closed-loop model consisting of high-resolution (3D) arterial models of aorta and large pulmonary arteries, coupled to (0D) lumped parameter models of heart (H) and distal circulations (W).

3.3.4.3 Boundary condition design and calibration

Boundary condition design and calibration are achieved via a process which includes three stages of lumped parameter model circuit design, iterative tuning of parameters, and adjustment of truncated ventricular volume and elastance waveforms (**Figure 3.5A**). The boundary condition design consists of the following three stages [141]: Stage 1, open-loop arterial model with imposed aortic and MPA flows (**Figure 3.5B**); Stage 2, open-loop arterial model with a 0D heart model (**Figure 3.5C**); and Stage 3, closed-loop arterial model with a 0D heart model (**Figure 3.5D**). Within each stage, parameters were iteratively tuned until simulated results matched clinical data

on flow and pressure [93]. Calibrated parameters were transferred to the corresponding lumped parameter circuits of the subsequent stage.

Following the three-stage parameter calibration, simulated inflow waveforms did not match the shape of the measured clinical flow waveforms (even though the mean values did). Specifically, simulated inflow waveforms underestimated the length of systole, which led to an overestimated peak systolic flow (**Figure 3.5E, stage A**). To fix this discrepancy, PC-MRI data were used to re-define the ventricular volume during systole (**Figure 3.5E, stage B**). The adjusted volume waveforms were used to define a new ventricular elastance (**Figure 3.5E, stage C**), and simulations with the Stage 3 circuit design were re-run. The new computed inflow waveforms reproduced better the shape of the clinical waveforms (**Figure 3.5E, stage D**). A detailed description of the calibration process is given next.

3.3.4.3.1 Iterative tuning of lumped parameters.

Lumped parameter values (**Table 3.2**) were estimated using a fixed-point iteration algorithm [93]. The iterative algorithm leverages their 1D models to efficiently calibrate outflow boundary condition parameters in 3D patient-specific arterial models. This work was used to define the iterative formulas presented below that aim to match simulated results with clinical hemodynamic data.

Stage 1, open-loop arterial model with imposed aortic and MPA flows. 3-element Windkessel models were used to represent the resistance and compliance of the distal vascular bed. Windkessel resistances R_j and compliances C_j for each outlet branch j were iteratively tuned using:

$$R_j^{n+1} = R_j^n \frac{R_T^{n+1}}{R_T^n}, \quad C_j^{n+1} = C_j^n \frac{C_T^{n+1}}{C_T^n}, \quad (3.4)$$

where the total arterial resistance R_T and total arterial compliance C_T were iteratively estimated as:

$$R_T^{n+1} = R_T^n + \frac{P_{mean} - P_{mean}^n}{Q_{mean}^n}, \quad (3.5)$$

$$C_T^{n+1} = C_T^n \frac{P_{pulse}}{P_{pulse}^n}, \quad (3.6)$$

where n is the iteration counter. Simulated (P_{mean}^n, P_{pulse}^n) and measured pressures (P_{mean}, P_{pulse}) were compared at the DTA and MPA.

Table 3.2 Hemodynamic metrics and tuned parameters of the high-resolution arterial model.

Hemodynamic Metrics & Features	Tuned Parameter(s)
Pulmonary Arterial Mean Pressure	$R_T^{Pulmonary}$ $P_{initial}^{Pulmonary}$
Pulmonary Arterial Pulse Pressure	$C_T^{Pulmonary}$
Pulmonary Cardiac Output	$R_T^{Pulmonary}$ $P_{initial}^{Pulmonary}$
Shape of MPA Flow Waveform	K_S^{RV}
Systemic Arterial Mean Pressure	$R_T^{Systemic}$ $P_{initial}^{Systemic}$
Systemic Arterial Pulse Pressure	$C_T^{Systemic}$
Systemic Cardiac Output	$R_T^{Systemic}$ $P_{initial}^{Systemic}$
Shape of AAo Flow Waveform	K_S^{LV}

Stage 2, open-loop arterial model with a 0D heart model. Initial nodal pressures of the lumped-parameter heart models and Windkessel models for each branch were iteratively tuned:

$$P_{initial}^{n+1} = P_{initial}^n * average\left(\frac{Q_{mean}}{Q_{mean}^n}, \frac{P_{mean}}{P_{mean}^n}\right). \quad (3.7)$$

Simulated (Q_{mean}^n) and measured flow rates (Q_{mean}) were compared at the AAo and MPA. Coefficients of the dynamic source resistance (R_S) were tuned to match the decay curve of the inflow waveforms [144].

Stage 3, closed-loop arterial model with a 0D heart model. Systemic and pulmonary venous systems, represented via 3-element Windkessel models, were added to connect the arterial outlets

to the atria of the lumped-parameter heart models, creating a closed-loop circulation (**Figure 3.5D**). Windkessel resistances (Formulas (4) and (5)) and compliances (Formulas (4) and (6)), and initial nodal pressures of the lumped-parameter models (Formula (7)) were iteratively tuned.

For each patient-specific model, 30-70 lumped parameter values were calibrated until all relative errors between measured and simulated hemodynamics were below 10%. Relative errors were calculated as $|(H_i^{data} - H_i^{model})/H_i^{data}| * 100$, where $H_i = \{P_{mean}, P_{systolic}, P_{diastolic}, Q_{mean}\}$ for a cardiac cycle once simulated results achieved cycle-to-cycle periodicity. Calibrated lumped parameter model values are detailed in **Appendix A**.

3.3.4.3.2 Adjustment of volume and elastance waveforms

The systolic phase of the PC-MRI flow waveform was integrated over time to derive ejected volume. PC-MRI-derived stroke volume was scaled to match short-axis MRI stroke volume. End-diastolic volume was assigned directly from short-axis MRI data, and the scaled PC-MRI-derived volume guided the systolic phase of the ventricular volume waveform. The filling phase of the volume waveform remained unchanged (**Figure 3.5E, stage B**). Adjusted ventricular volume waveforms were used to re-derive elastance waveforms (**Figure 3.5E, stage C**). Adjusted ‘Two-Hill’ elastance parameter values are found in **Appendix Table A.3**.

The discrepancies between clinical and simulated MPA and ATA flow waveforms were evaluated using a L2-norm metric $S = \sum_{i=1}^n (data_i - simulation_i)^2$. Overall, following the PV-loop alignment and adjustments of the ventricular volume waveforms outlined earlier, reductions in L2-norm metric of $40\% \pm 18\%$ at the MPA and $10\% \pm 9\%$ at the AAo were achieved.

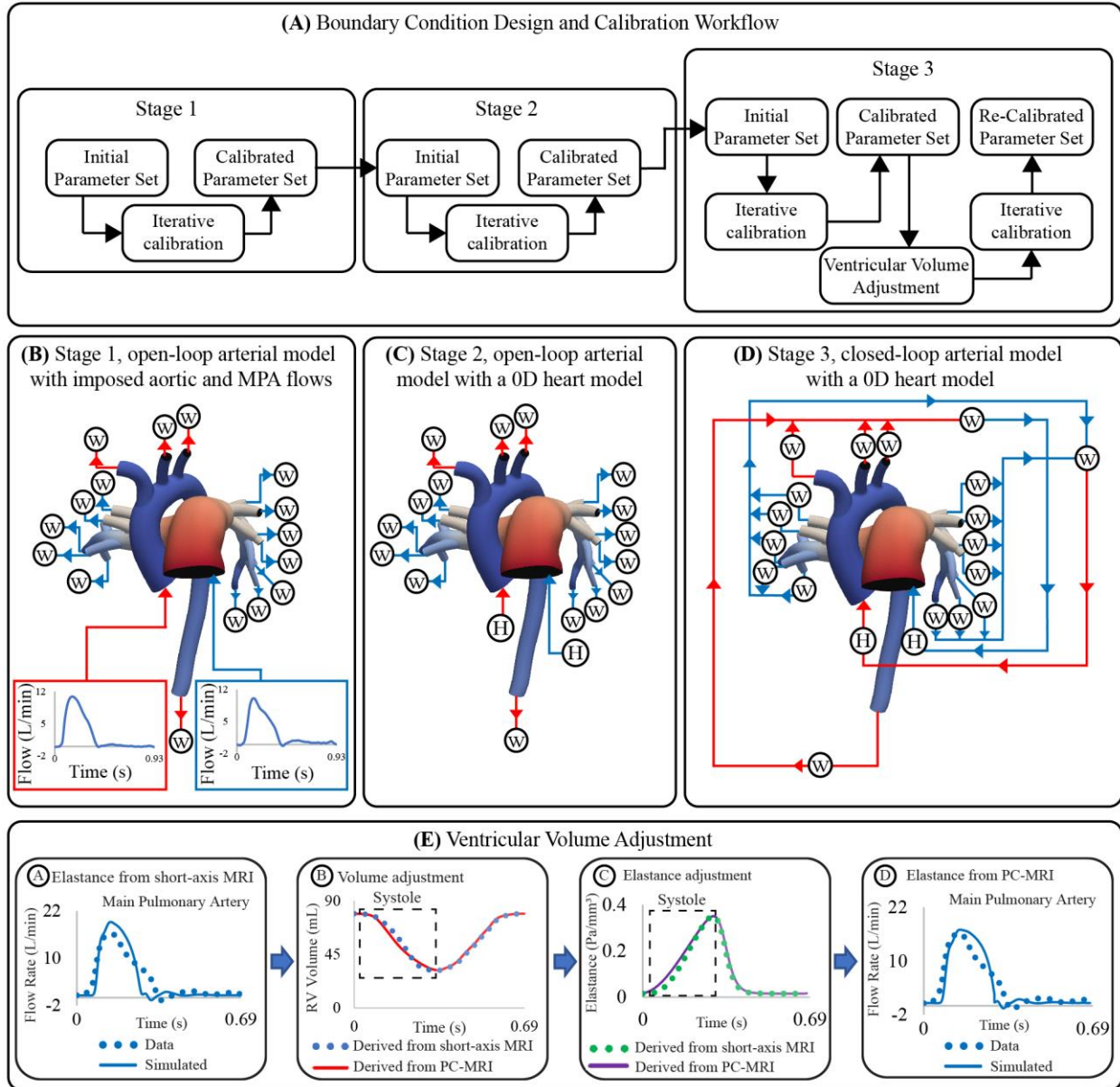


Figure 3.5 (A) Workflow for boundary condition design and calibration of high-resolution arterial models. (B-D) Stage 1-3 of boundary condition design, respectively. (E) Strategy for ventricular volume adjustment.

3.3.5 High-resolution ventricular model

In this model, truncated 3D biventricular geometries (see Section 3.3.3.1.2) were coupled to a 0D closed-loop circulatory model representing the distal systemic and pulmonary circulations, atria, and heart valves (**Figure 3.6**).

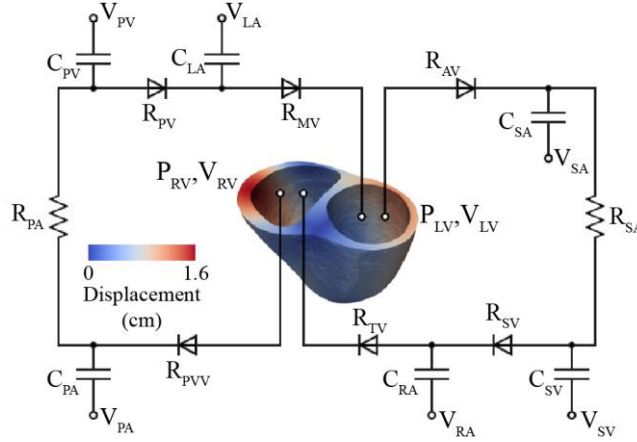


Figure 3.6 High-resolution (3D) ventricular model coupled to a 0D closed-loop circulatory model, which includes the systemic and pulmonary arteries, venous systems, atria, and valves.

3.3.5.1 3D biventricular models

Governing equations of the 3D biventricular models based on a quasi-static formulation and assuming that the cardiac tissue behaves as an incompressible material were solved using the open-source software FEniCS [96], as detailed in [78], [94], [95]. An active stress formulation was used to describe the mechanical behavior of myocardial tissue whereby the first Piola Kirchhoff stress tensor P was decomposed into active and passive components P_a and P_p ($P = P_a + P_p$), represented with an active contraction model and a passive constitutive model, respectively.

STL models of the truncated ventricles (Section 3.3.3.1) generated at the end-systolic phase define the unloaded configuration [146]. This truncation was performed to avoid modeling the basal regions of the heart, including the valves and atria, which are often poorly resolved in the short-axis MRI sequence and are represented with lumped-parameter circuits. The 3D biventricular model was divided into three material regions: LV free wall, septum, and RV free wall. Helix angles of the myocardial fibers were linearly varied along the transmural direction from 60° at the endocardium to -60° at the epicardium [147] using a Laplace-Dirichlet rule-based algorithm [148].

These models were discretized using GMSH [149] to define tetrahedral grids of 9,159 to 11,726 elements and 2,884 to 3,548 nodes. Mesh refinement studies were performed to ensure that hemodynamic results were independent of mesh size.

3.3.5.1.1 Active contraction model:

The active stress P_a was represented using a time-varying elastance model that depends on the length of the myocardial muscle fiber along the local myofiber direction [107],

$$P_a = T_{ref} \frac{Ca_0^2}{Ca_0^2 + ECa_{50}^2} C(t) \mathbf{e}_f \otimes \mathbf{e}_{f_0} \quad (3.8)$$

where T_{ref} is the reference tension, Ca_0 is the peak intracellular calcium concentration, and \mathbf{e}_f and \mathbf{e}_{f_0} are the local vectors that define the muscle fiber direction in current and reference configurations, respectively. The function $C(t)$ is given by

$$C(t) = \begin{cases} \frac{1}{2} \left(1 - \cos \left(\pi \left(\frac{t}{t_0} \right) \right) \right), & t < t_t \\ \frac{1}{2} \left(1 - \cos \left(\pi \frac{t_t}{t_0} \right) \right) \exp \left(\frac{t_t - t}{\tau} \right), & t \geq t_t \end{cases} \quad (3.9)$$

where t_0 is the time at peak tension, t_t is the time at which isovolumic relaxation of the muscle starts, and τ is a time constant associated with the relaxation duration. The length dependent calcium sensitivity ECa_{50} is given by

$$ECa_{50} = \frac{(Ca_0)_{max}}{\sqrt{\exp(B(l - l_0)) - 1}} \quad (3.10)$$

where $(Ca_0)_{max}$ is the maximum peak intracellular calcium concentration and l_0 is the sarcomere length at which no active tension develops.

In this work, we used an active contraction model based on that from [107] which led to the slope of RV ESPVR having a value of 1.32 ± 0.78 mmHg/mL, which is well aligned with values reported in literature [76], [150].

3.3.5.1.2 Passive constitutive model

In this model, the strain energy function was given by $W = 0.5 \cdot c(e^Q - 1)$, where Q is a quadratic function of the strain components defined in the material directions:

$$Q = b_{ff}E_{ff}^2 + b_{xx}(E_{ss}^2 + E_{nn}^2 + E_{sn}^2 + E_{ns}^2) + b_{fx}(E_{fn}^2 + E_{nf}^2 + E_{fs}^2 + E_{sf}^2). \quad (3.11)$$

Components of Green-Lagrange strain tensor E_{ij} with $(i, j) \in (f, s, n)$ denote the myocardial fiber (f), sheet (s), and sheet normal (n) directions. c is a coefficient scaling passive stiffness. b_{ff} , b_{xx} , and b_{fx} are material constants.

3.3.5.2 Lumped-parameter (0D) vascular models

The lumped-parameter models of systemic and pulmonary circulation are divided into arterial and venous segments with compliances (C_{sa} and C_{sv} , C_{pa} and C_{pv}) and resistances (R_{sa} and R_{sv} , R_{pa} and R_{pv}), respectively. Mitral and aortic valves are represented via diodes with resistances (R_{mv}) and (R_{av}), respectively. Tricuspid and pulmonary valves are represented via diodes with resistances (R_{tv}) and (R_{pvv}), respectively. Left and right atria were modeled using time-varying elastance functions, respectively.

3.3.5.3 Model calibration

3.3.5.3.1 Parameters of the lumped-parameter vascular models

Parameters were iteratively calibrated until the following simulated and clinical metrics matched within 10%: LV and RV end-diastolic and end-systolic volumes, LV and RV end-systolic

pressures, and systemic and pulmonary arterial mean and pulse pressures [78], [94], [151], see **Table 3.3**. Resting volumes of pulmonary and systemic veins ($V_{pv,0}$ and $V_{sv,0}$) were adjusted to match LV and RV end-diastolic volumes, respectively. However, it should be noted that the impact of tuning $V_{sv,0}$ and $V_{pv,0}$ in most hemodynamic metrics is high [152], leading to changes in ventricular end-systolic and end-diastolic pressures and volumes. Systemic and pulmonary arterial resistances (R_{sa} and R_{pa}) were adjusted to match systemic and pulmonary arterial mean pressures and flows, and LV and RV end-systolic volumes, respectively. Systemic and pulmonary arterial compliances (C_{sa} and C_{pa}) were adjusted to match systemic and pulmonary arterial pulse pressures, respectively. Therefore, LV and RV systolic pressures were also matched by simultaneously calibrating R_{sa} , R_{pa} , C_{sa} and C_{pa} . Parameters of the left and right atrial elastance waveforms were set based on a previous study [94].

3.3.5.3.2 Parameters of the 3D biventricular models

LV free wall and septum were assigned to have the same passive stiffness C_{LV} and contractility $T_{ref,LV}$ values, while RV free wall had distinct values of passive stiffness C_{RV} and contractility $T_{ref,RV}$. Passive stiffness parameters (C_{LV} and C_{RV}) were adjusted to match LV and RV end-diastolic pressures, respectively. LV and RV end-systolic volumes were matched by adjusting regional contractility parameters of the active contraction model $T_{ref,LV}$ and $T_{ref,RV}$, respectively. Parameters of the active contraction model (t_0 , t_i , and τ) were adjusted to match LV and RV volume and pressure waveforms. The parameter t_0 was adjusted to match the time to peak tension, t_i was adjusted to specify the start of the isovolumic relaxation phase and τ was adjusted to match the rate of relaxation of the myofibers.

Table 3.3 Hemodynamic metrics and tuned parameters of the high-resolution ventricular models.

Hemodynamic Metrics & Features	Tuned Parameter(s)
---	---------------------------

LV End-Systolic Volume	$T_{ref,LV} V_{pv,0} R_{sa}$
LV End-Systolic Pressure	$R_{sa} T_{ref,LV} C_{sa} V_{pv,0}$
LV End-Diastolic Volume	$V_{pv,0}$
LV End-Diastolic Pressure	$V_{pv,0} C_{LV}$
Systemic Arterial Mean Pressure	R_{sa}
Systemic Arterial Pulse Pressure	C_{sa}
RV End-Systolic Volume	$T_{ref,RV} V_{sv,0} R_{pa}$
RV End-Systolic Pressure	$R_{pa} T_{ref,RV} C_{pa} V_{sv,0}$
RV End-Diastolic Volume	$V_{sv,0}$
RV End-Diastolic Pressure	$V_{sv,0} C_{RV}$
Pulmonary Arterial Mean Pressure	R_{pa}
Pulmonary Arterial Pulse Pressure	C_{pa}
Time to Peak Tension	t_0
Start Time of Relaxation	t_t
Rate of Relaxation	τ

For each patient-specific model, 16 parameters related to the lumped-parameter vascular models, active contraction models, and passive constitutive models were calibrated and are detailed in **Appendix Table A.3**.

3.3.6 Metrics for disease severity stratification

Patients were stratified from lowest to highest disease severity, by a team composed of 3 pediatric cardiologists with extensive experience in treating PAH, based on the available clinical metrics (see **Table 3.4**). We explored the correlation between the disease severity stratification and clinical metrics and model-derived metrics (from both high-resolution arterial and ventricular models). For each metric, the correlation was assessed using Spearman's rank correlation coefficient ρ .

3.3.6.1 Clinical metrics

A total of 36 data-derived metrics were evaluated in the disease severity stratification study, including patient demographics (age, height, weight, etc.), indexed MRI-derived metrics

(ventricular volume indices, ventricular mass indices, cardiac index etc.), and catheterization-derived metrics (pulmonary arterial pressures, pulmonary vascular resistance, etc.), see **Table 3.1**.

Table 3.4 Stratification of patients from lowest (value of 1) to highest (value of 8) disease severity.

Clinical disease severity ranking (1:least, 8:most)	1	2	3	4	5	6	7	8
Subject Number	Subj. #8	Subj. #2	Subj. #3	Subj. #6	Subj. #5	Subj. #4	Subj. #1	Subj. #7

3.3.6.2 Model-derived metrics

A total of 21 model-derived metrics and parameters were included in the disease severity stratification study. The inclusion of the parameters and metrics was determined by the following criteria:

- Lumped-parameter model and 3D parameters with a direct counterpart in the clinical data (i.e., total arterial compliance and resistance, linearized arterial stiffness).
- All 3D ventricular model parameters (i.e., ventricular contractility and passive stiffness).
- Model metrics with well-established clinical meaning such as arterial pulse wave velocity and ventricular-vascular coupling (i.e., RV ESPVR, RV Ea, RV ESPVR/Ea).

Individual lumped parameters for which there were no direct measurements (i.e., proximal and distal resistances, venous circuit parameters, etc.) were excluded.

3.3.6.2.1 High-resolution arterial models

Stiffness derived at five anatomical locations (AAo, DTA, MPA, LPA, and RPA), peak LV and RV elastance, MPA-LPA, MPA-RPA, and AAo-DTA pulse wave velocities, and distribution of central and peripheral pulmonary vasculature resistance and compliance [153] were evaluated.

3.3.6.2.2 High-resolution ventricular models

RV end-systolic pressure volume relationship (ESPVR), arterial elastance (Ea), and (ESPVR/Ea) ratio were evaluated. For each calibrated subject, RV ESPVR was estimated by varying preload ($V_{sv,0}$) and calculating the slope between peak end-systolic elastance (**Figure 3.7**). RV Ea was estimated by dividing end-systolic pressure over stroke volume. Calibrated values of LV and RV contractility ($T_{ref,LV}$ and $T_{ref,RV}$) and passive stiffness (C_{LV} and C_{RV}) were also evaluated.

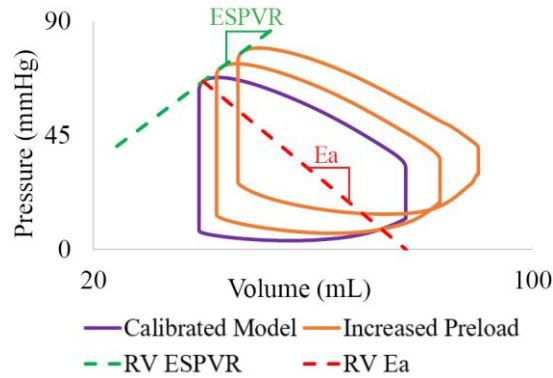


Figure 3.7 Metrics derived from the high-resolution ventricular models.

All clinical and model-derived metrics included in the disease severity stratification study are detailed in **Appendix Table A.3**.

3.4 Results

3.4.1 High-resolution arterial models

Following model parameter calibration (see **Table 3.2**), simulation results successfully reproduced patient-specific clinical hemodynamic data within 10% (**Figure 3.8**). Pressures were compared between our patient cohort and a cohort of healthy pediatric subjects [115]. Pulmonary arterial mean pressures (45.4 ± 19.3 mmHg), and pulmonary arterial pulse pressures (35.7 ± 14.3

mmHg) were higher than values measured in healthy pediatric subjects. Mean systemic arterial pressures (69.9 ± 11.6 mmHg) were similar to those measured in healthy pediatric subjects.

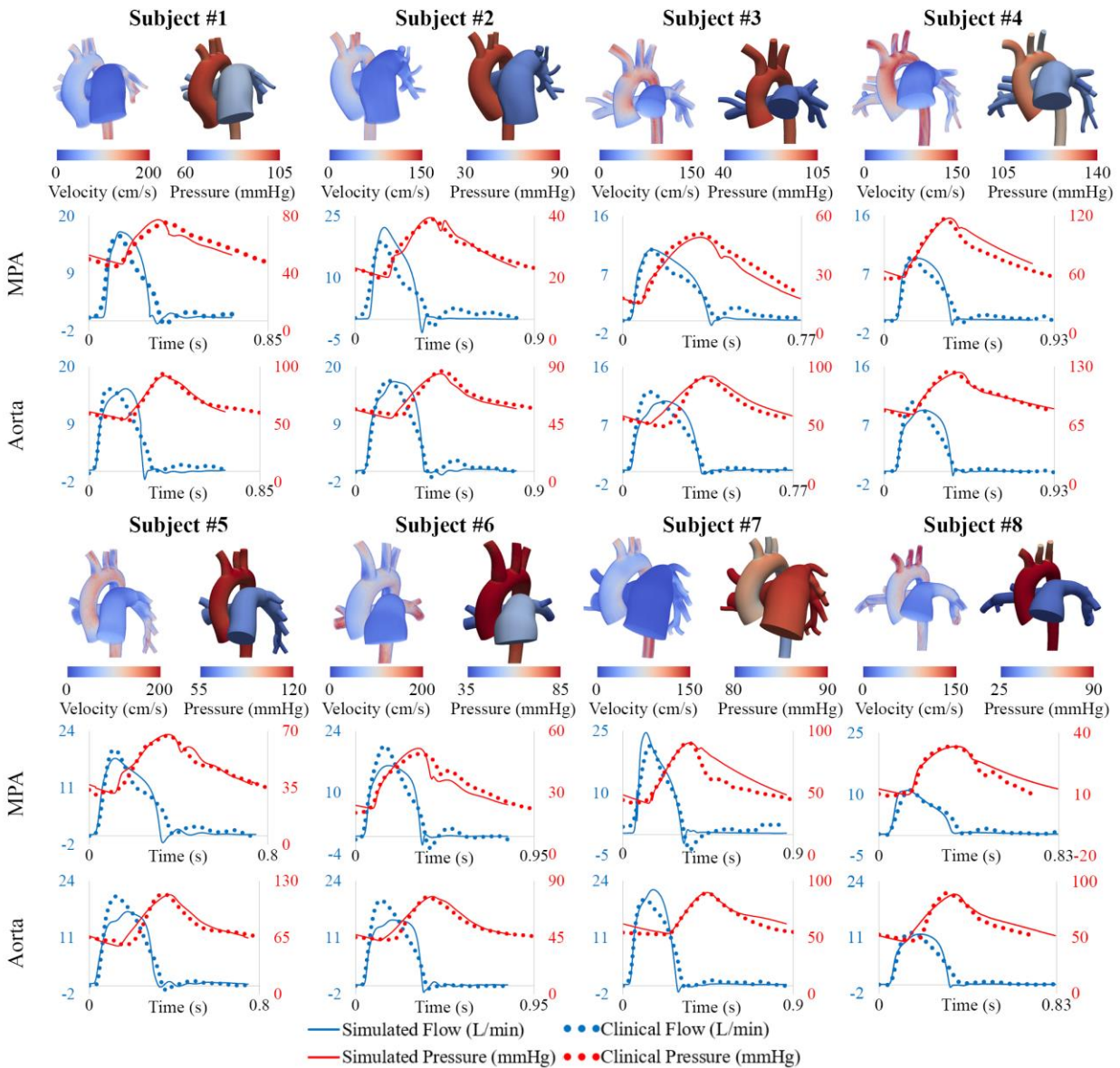


Figure 3.8 Velocity and pressure maps of the high-resolution arterial models at peak systole. Hemodynamic comparison shows agreement between simulated and clinical data.

The distribution of central and peripheral pulmonary vasculature resistance and compliance was obtained. Central (e.g., 3D) pulmonary arteries contributed to $8\% \pm 8\%$ and $56\% \pm 19\%$ of the total pulmonary resistance and compliance, respectively (**Figure 3.9**).

MPA stiffness (206.6 ± 159.7 kPa) was found to be higher and have a greater variability than AAO stiffness (146.7 ± 19.2 kPa), in line with the severity and disease heterogeneity of these patients. LPA, RPA, and DTA stiffness were estimated to be 163.0 ± 192.3 kPa, 130.4 ± 105.6 kPa, and 227.3 ± 66.4 kPa, respectively.

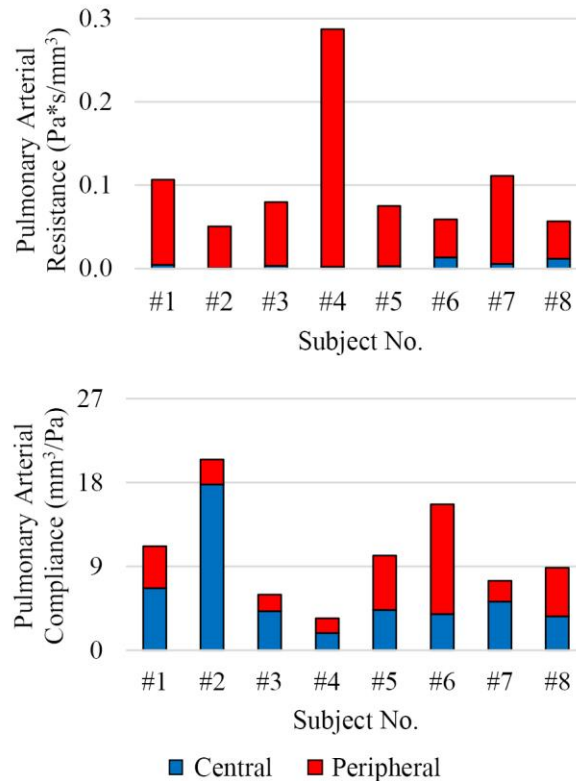


Figure 3.9 Distribution of total pulmonary arterial resistance and compliance between central (3D model, shown in blue) and peripheral (lumped-parameter models, shown in red) pulmonary vessels.

Pulmonary and systemic arterial pulse wave velocity were estimated to be 3.5 ± 1.5 m/s from the MPA to the LPA, 3.0 ± 0.9 m/s from the MPA to the RPA, and 3.9 ± 1.0 m/s from the AAO to the DTA. Pulmonary arterial stiffness and pulse wave velocity in our patient cohort were higher than in healthy pediatric subjects [154], confirming that our results capture arterial remodeling reflective of PAH.

Subject #4 had the highest pulmonary resistance, lowest pulmonary arterial compliance, highest pulmonary artery stiffness, highest MPA-LPA pulse wave velocity, and near systemic level

of pulmonary arterial pressure, indicating that this subject has the most severe form of pulmonary arterial dysfunction. Furthermore, Subject #4 was the only subject with a pulmonary arterial compliance index below the critical threshold value of 0.9 mL/mmHg/m², which has been correlated with a significant reduction in life expectancy [155].

3.4.2 High-resolution ventricular models

Following model calibration (see **Table 3.3**), simulated PV loops and arterial pressures were closely matched to clinical data (**Figure 3.10**). On average, RV end-diastolic (99.0 ± 44.6 mL) and end-systolic (58.5 ± 23.4 mL) volumes were larger than their LV counterparts (83.5 ± 23.4 mL and 43.0 ± 14.7 mL, respectively). RV stroke work (0.30 ± 0.17 J) was calculated to be 69% of LV stroke work (0.42 ± 0.14 J). RV ejection fraction ($42\% \pm 5\%$) was lower than LV ejection fraction ($51\% \pm 5\%$). Of note, RV ejection fraction in our patients was found to be significantly lower than in healthy pediatric subjects ($58\% \pm 5\%$) [154], indicating ventricular remodeling.

Calibrated ventricular models were used to derive arterial and RV elastance metrics: $ESPVR = 1.32 \pm 0.78$ mmHg/mL; $Ea = 1.84 \pm 0.78$ mmHg/mL; $ESPVR/Ea = 0.75 \pm 0.21$. RV $ESPVR$ in our cohort was found to be higher than in pediatric patients with repaired tetralogy of Fallot (0.32 ± 0.15 mmHg/mL) [156].

Subject #7 had the largest RV end-diastolic volume, largest RV end-systolic volume (Z-score = 5.4), lowest RV ejection fraction (Z-score = -4.0), and largest RV stroke work (0.71 J), suggesting that this patient had the most severe form of RV dysfunction [157], [158]. Subject #4, who has the most severe form of pulmonary arterial dysfunction (Section 3.4.1), has relatively normal RV volumes [154], suggesting that this patient has not undergone significant RV

remodeling. These results highlight the importance of simultaneously describing arterial and ventricular hemodynamics and biomechanics.

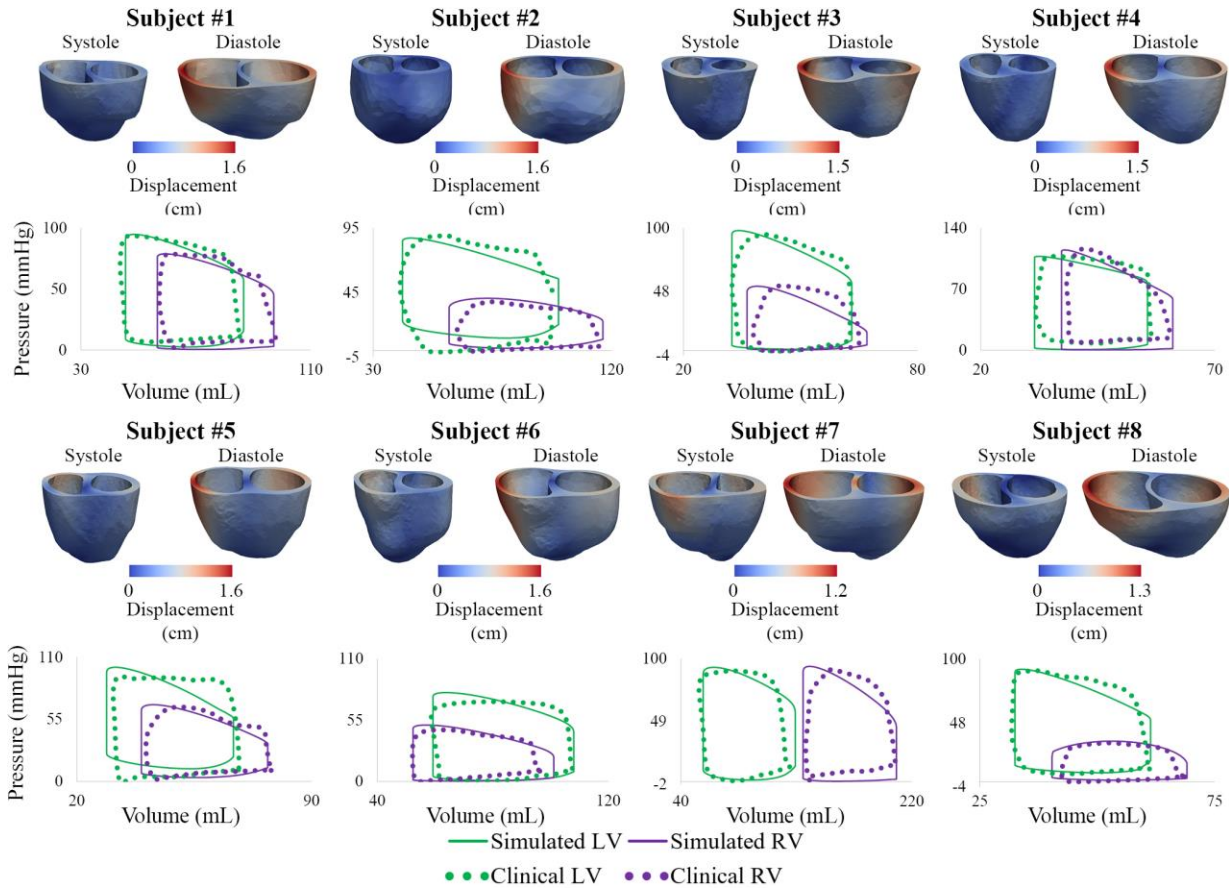


Figure 3.10 Displacement maps of ventricular models at end-systole and end-diastole. Comparison of LV and RV PV loops shows agreement between simulated and clinical data.

3.4.3 Metrics for disease severity stratification

The correlation between clinically assessed disease severity (**Table 3.4**) and each data- and model-derived metric were ranked using the absolute value of the Spearman's rank correlation coefficient ρ (**Table 3.5**). The analysis was adjusted for multiple comparisons by controlling for a 10% false discovery rate [159]. A metric is significantly correlated if its p-value is smaller than its Benjamini-Hochberg critical value (**Table 3.5**, iQ/m). After adjusting for multiple comparisons, 13 metrics were found to be significantly correlated, all of which were either catheterization-derived metrics (**Table 3.5**; orange) or model-derived metrics (**Table 3.5**; green). None of the

patient demographics (Table 3.5; black) or MRI-derived metrics (Table 3.5; purple) were significantly correlated with disease severity.

Table 3.5 Spearman’s rank correlation coefficients (ρ), p -values (p -val), and Benjamini-Hochberg critical value (iQ/m) of each data-derived and model-derived metric resulting from a comparison to clinical disease severity rankings are shown in two columns.

	Metric	ρ	p -val	iQ/m	Metric	ρ	p -val	iQ/m
Significantly Correlated Metrics	RPA Stiffness	0.929	<0.001	0.002	RV Systolic Pressure/LV Systolic Pressure	0.857	0.007	0.014
	R_pulmonary/R_systemic	0.929	<0.001	0.003	MPA Diastolic Pressure	0.833	0.010	0.015
	RV Stroke Work/LV Stroke Work	0.905	0.002	0.005	MPA-RPA Pulse Wave Velocity	0.833	0.010	0.018
	RV Contractility ($T_{Ref,RV}$)	0.905	0.002	0.007	LV Contractility ($T_{Ref,LV}$)	-0.810	0.015	0.019
	MPA Systolic Pressure	0.905	0.002	0.009	Total Pulmonary Arterial Resistance	0.810	0.015	0.021
	RV Stroke Work	0.881	0.004	0.010	PVR Index	0.810	0.015	0.023
	MPA Mean Pressure	0.881	0.004	0.012				
Non-Significant Metrics	MPA Stiffness	0.762	0.028	0.025	Age	0.333	0.420	0.063
	MPA Pulse Pressure	0.738	0.037	0.026	Pulmonary Capillary Wedge Pressure	0.286	0.493	0.065
	Pulmonary Arterial Compliance Index	0.738	0.037	0.028	LV End-Systolic Volume Index	0.286	0.493	0.067
	RV Mass Index	0.738	0.037	0.030	Percentage Flow to LPA	-0.286	0.493	0.068
	RV Ejection Fraction	-0.667	0.071	0.032	Catheterization Heart Rate	0.238	0.570	0.070
	MPA-LPA Pulse Wave Velocity	0.643	0.086	0.033	LV Passive Stiffness (C_{LV})	-0.214	0.610	0.072
	MPA Area Index	0.643	0.086	0.035	Height	0.214	0.610	0.074
	RV End-Systolic Volume Index	0.643	0.086	0.037	RV Emax	-0.143	0.736	0.075
	Systemic Arterial Diastolic Pressure	0.619	0.102	0.039	RV Passive Stiffness (C_{RV})	-0.143	0.736	0.077
	Total Pulmonary Arterial Compliance	-0.595	0.120	0.040	RV ESPVR/Ea	-0.119	0.779	0.079
	LPA Stiffness	0.595	0.120	0.042	DTA Stiffness	0.119	0.779	0.081
	RV ESPVR	0.571	0.139	0.044	Weight	0.119	0.779	0.082
	LV Stroke Volume Index	0.524	0.183	0.046	BSA	0.119	0.779	0.084
	LV Mass Index	0.476	0.233	0.047	AAo-DTA Pulse Wave Velocity	0.095	0.823	0.086
	LV End-Diastolic Volume Index	0.476	0.233	0.049	RV SV Index	0.095	0.823	0.088
	MPA Relative Area Change	-0.476	0.233	0.051	Central Pulmonary Arterial Compliance	0.071	0.867	0.089
	Central Pulmonary Arterial Resistance	-0.429	0.289	0.053	MPA Oxygen Saturation	-0.071	0.867	0.091
	RV Ea	0.429	0.289	0.054	AAo Stiffness	-0.048	0.911	0.093
	LV Emax	-0.405	0.320	0.056	MRI Heart Rate	-0.048	0.911	0.095
	Systemic Arterial Mean Pressure	0.381	0.352	0.058	Cardiac Index	0.048	0.911	0.096
RV End-Diastolic Volume Index	0.381	0.352	0.060	Systemic Arterial Pulse Pressure	0.024	0.955	0.098	
Systemic Arterial Systolic Pressure	0.333	0.420	0.061	LV Ejection Fraction	0.000	1.000	0.010	

Patient demographics are shown in black font, MRI-derived metrics are shown in purple font, catheterization-derived metrics are shown in orange font, and model-derived metrics are in green font.

Mean, systolic, and diastolic pulmonary arterial pressures were significantly correlated with clinically assessed disease severity. Pulmonary capillary wedge pressure, which is a measure of the post-capillary pulmonary circulation (i.e., pulmonary venous pressure and LV end-diastolic pressure), was weakly correlated to disease severity ($\rho = -0.071$). Systemic mean, systolic, and diastolic pressures were not significantly correlated to disease severity. There were 5 model-derived metrics (**Table 3.5; green**) strongly correlated with disease severity. RV contractility ($T_{ref,RV}$), RPA stiffness, and MPA-RPA pulse wave velocity were all significantly correlated metrics. Interestingly, LV contractility ($T_{ref,LV}$) was the only metric that had a negative, significant correlation with clinically assessed disease severity, suggesting that LV contractility decreases with PAH progression.

3.5 Discussion

Pediatric PAH is a complex disease with a heterogeneous population and multiple compounding factors that contribute to disease progression. It is thus important to identify metrics to stratify patients and to predict disease progression. Computational models enable the study of hemodynamics and biomechanics in the cardiopulmonary and systemic circulations and can be used to describe PAH pathophysiology. In this work, computational models were used to complement clinical data by providing high-resolution description of hemodynamics and biomechanics, including those that are not easy to assess in a clinical setting. To our knowledge, this is one of the first efforts to construct and calibrate two separate high-resolution closed-loop models of pulmonary and systemic arteries and ventricles using data from a pediatric PAH cohort.

Model calibration entailed tuning of numerous model parameters, identifying inconsistencies in clinical data, and developing strategies to mitigate these inconsistencies. Calibrated models could reproduce the following patient-specific data: cardiac output in the MPA

and AAO, pressure waveforms at the MPA and DTA, mean flows at the DTA, LPA, and RPA, and LV and RV PV loops. Following calibration, our models were used to derive metrics such as RV ESPVR, arterial elastance (E_a), $ESPVR/E_a$, ventricular contractility, central pulmonary arterial stiffness and pulse wave velocity, and distribution of pulmonary arterial resistance and compliance between central and peripheral vessels.

Numerous data-derived metrics were correlated with clinical stratification of disease severity. MRI-derived metrics were not significantly correlated with clinical disease severity stratification. The correlation in RV mass index ($\rho = 0.738$) can be attributed to the adaptive response of the RV (myocardial hypertrophy) to a sustained afterload increase, which can also be linked to the strong correlation seen in RV contractility ($T_{ref,RV}$). RV ejection fraction had a correlation value of $\rho = -0.667$, confirming that this commonly used non-invasive metric [160], [161] could help in patient stratification. Multiple catheterization-derived ($n = 8$) and model-derived ($n = 5$) metrics had significant correlations with disease severity clinical stratification (**Table 5**), suggesting the superior specificity of these metrics in capturing PAH disease severity over MRI metrics alone.

RV contractility ($T_{ref,RV}$) had a positive, significant correlation with disease severity, whereas LV contractility ($T_{ref,LV}$) had a negative, significant correlation. This reduction of LV contractility related to PAH progression is commonly attributed to impaired LV diastolic filling [162], [163] or LV atrophy [164]. However, pulmonary capillary wedge pressure (a surrogate for LV diastolic filling pressure) and pulmonary venous resting volume ($V_{pv,0}$) (LV preload parameter) both had weak correlations with disease severity, while LV mass index had a positive, moderate correlation. These suggest that LV diastolic filling and LV mass are not significantly affected by PAH progression. Our results imply, however, that only LV contractility is impaired due to PAH

progression which has been confirmed in a computational study comparing PAH patients and control subjects [165] and in an experimental study where the force-generating capacity of isolated LV cardiomyocytes was reduced in PAH patients [166].

Our models captured PAH-induced biomechanical adaptations, both in the central (i.e., increase in stiffness and pulse wave velocity) and peripheral (i.e., increase in PVR index) vessels, as well as in the ventricles (i.e., changes in contractility). Increases in pulmonary pressures (i.e., arterial load) were accompanied by increases in RV contractility for the cohort. This suggests that ventricular-arterial coupling was maintained. The weak correlation between model-derived RV ESPVR/Ea and disease severity further supports this observation for the cohort [12]. These findings confirm that computational models of ventricular-arterial interactions can provide additional insight on PAH pathophysiology.

3.5.1 Clinical Applications

The main clinical application areas of our work are two: (1) the potential for replacing or minimizing the number of invasive catheterization procedures in PAH patients, and (2) a more sensitive method for patient stratification.

3.5.1.1 Potential for minimization of catheter-based assessment in PAH

Computational models required catheterization data and extensive calibration efforts. However, once calibrated using a large cohort of patient data, these computational models could then be validated against new cohorts of patient data without directly inputting measures derived from invasive pressure. This would entail developing correlations between imaging markers such as MPA diameter and relative area change, RV volume, RV ejection fraction, shape of MPA flow waveforms, etc. [167]–[170]. Furthermore, our calibrated computational models were used to virtually increase ventricular preload to estimate RV ESPVR which obviates the need for an

invasive procedure. This model-derived estimation of RV ESPVR can then be used to provide a description of RV contractility and ventricular-arterial coupling (via ESPVR/Ea), which are both known to play key roles in PAH pathophysiology [50].

3.5.1.2 Patient stratification in PAH

Despite significant improvements in the understanding of PAH pathological hemodynamics [30], [120], [125], [165], hurdles remain in PAH patient stratification. In this work, computational models were combined with clinical data to stratify PAH patients according to disease severity, confirming well-established data-derived markers [161], [171]–[173] and elucidating model-derived markers that could aid in risk stratification.

PAH requires life-long medical care, and construction and calibration of each computational model typically requires nearly 1 month. This long calibration timeframe could be reduced with advances in data assimilation methods [174]–[176]. Therefore, patient-specific computational models could be used to provide insight on PAH pathophysiology and stratification and could ultimately help clinicians tailor a long-term management plan.

3.6 Limitations

A small number ($n = 8$) of pediatric PAH patients were included in this study, which affects the strength of the statistical analysis performed to correlate metrics with clinical disease severity stratification. Therefore, due to this small sample size, our analysis was used to broadly describe observed correlations rather than to identify optimal metrics to use in patient stratification. Furthermore, control subjects were not included in our study, which further hinders the ability to identify model parameters for patient stratification. Future extensions of this work will include a greater number of PAH patients as well as control subjects to provide a more robust patient stratification analysis.

A key data inconsistency not addressed in our work was the mismatch in cardiac output between high-resolution arterial and ventricular models. Arterial models were calibrated to match cardiac outputs from PC-MRI data, whereas ventricular models were calibrated to match stroke volumes from truncated ventricular segmentations which yielded lower cardiac outputs. This mismatch stems from truncating the ventricular geometries at the tricuspid valve. Even with this truncation of the ventricular geometries, our ventricular models produced lower RV ejection fraction than those seen in healthy pediatric subjects [154], and outputted metrics that correlated strongly with clinically assessed disease severity.

The number of parameters in our models is much larger than the amount of data used to calibrate our models, which leads to issues of parameter uniqueness and identifiability. However, our choices for the different components of the lumped-parameter circuits are based on well accepted, physiology-motivated, previously developed designs for heart and segments of the circulation [84], [87], [92]. The lack of data was offset by (arbitrary) modeling choices such as breakdown of flows proportional to surface areas, ratios of proximal to distal resistances in Windkessel models [177], literature values for certain components of heart models [84], [144].

A traditional parameter sensitivity analysis was performed, where the sensitivity of certain computed hemodynamic metrics to 10% changes in model parameters was obtained. The analysis was performed using both the arterial and ventricular models of Subject #6 (**Supplementary Tables 3.6 and 3.7**, respectively). The analysis showed that the ventricular models had a larger sensitivity to model parameters than the arterial models. However, this simple analysis does not address parameter identifiability, as it fails to consider correlation between parameters [178]. Therefore, a rigorous sensitivity analysis (outside the scope of this study) that overcomes these limitations is required to assess parameter uniqueness [174], [178]–[182]. This analysis would

therefore provide confidence in model-derived metrics and estimated parameters, and also quantify variability in parameters due to uncertainty in clinical data.

Clinically assessed disease severity rankings (**Table 3.4**) were used as the gold standard in our disease severity stratification analysis. However, these rankings were based on a combination of hemodynamic metrics and the clinical team's experience. Even though the clinical team is comprised of pediatric cardiologists with extensive experience in pediatric PAH management, conclusions drawn in our study could be affected by the subjective nature of the disease severity rankings.

Chapter 4 Hemodynamic Mechanisms Contributing to Renovascular Hypertension Caused by an Abdominal Aortic Coarctation

4.1 Original publication information

This chapter was originally published as a scientific article:

Tossas-Betancourt, C., van Bakel, T. M. J., Arthurs, C. J., Coleman, D. M., Eliason, J. L., Figueroa, C. A., & Stanley, J. C. (2020). Computational analysis of renal artery flow characteristics by modeling aortoplasty and aortic bypass interventions for abdominal aortic coarctation. *Journal of Vascular Surgery*, 71(2). <https://doi.org/10.1016/j.jvs.2019.02.063>

Changes made to the original document are mainly cosmetic to adhere to the format of this document.

4.2 Introduction

Suprarenal abdominal aortic coarctations (SAAC) are often associated with renal arterial stenoses and severe renovascular, or renin-mediated, hypertension [59]. In these circumstances, the increased blood pressure and development of collateral vessels circumventing the aortic and renal artery narrowings tend to increase mean renal blood flow toward normal. However, this response is inadequate and the abnormal release of renin persists. Whether the principal cause of the abnormal renin release is due to decreased renal artery pressure or abnormal renal artery flow waveforms is an unsettled issue.

The abnormal renin release and angiotensin generation coupled with secondary increases in aldosterone production make this form of hypertension refractory to most drug therapies. Lowering the systemic arterial pressure with drugs without treating the aortic and renal artery narrowings only results in further diminutions of intrarenal blood flow and continued excesses in renin production. Because of these medical failures, restoration of normal renal blood flow by open operative or endovascular interventions have evolved as the favored means of managing this disease.

The University of Michigan's history of treating occlusive lesions of the renal arteries and abdominal aorta in pediatric patients has extended for more than 4 decades [59], [183]–[187]. Postoperative blood pressure control in this experience has been optimal when treating patients with isolated renal artery stenoses, in contrast to less salutary outcomes when the renal artery procedures have been accompanied by a thoracoabdominal bypass (TAB) or patch aortoplasty (PA) for a coexisting abdominal aortic coarctation. Even after successful anatomic aortic and renal artery reconstructions, postoperative hypertension has been noted to persist [59], [188], [189].

It is hypothesized that the aortic reconstructive procedures may not normalize renal artery blood flow. A TAB from above a SAAC to below the renal arteries may cause turbulent and abnormal renal artery perfusion as retrograde aortic flow encounters antegrade flow in the region of the renal vasculature. In addition, performance of a PA, given the commonplace practice of oversizing the patch in younger patients to accommodate for later growth, may also result in abnormal renal blood flow and contribute to the persistence of the hypertensive state.

4.3 Methods

Aortorenal blood flow was retrospectively studied using patient-specific fluid-structure interaction (FSI) simulations in a child that was treated for a SAAC. Subsequently, the impact of

the most commonly undertaken surgical repairs (TAB and PA) on aortorenal blood flow was analyzed. The study was approved by the University of Michigan Board of Review (HUM00112350 and HUM00006223).

4.3.1 Patient history

A 9-year-old girl was referred to the authors' institution with a diagnosis of middle aortic syndrome and renin mediated hypertension. Her initial elevated blood pressures in the 130-150/90-95 mmHg range were only modestly improved to the 140/80 mmHg range following treatment with a beta-blocker and calcium channel blocker. In addition, she initially complained of lower extremity weakness and fatigue that was progressive with activity. Duplex Doppler ultrasonography estimated a pressure gradient of 58 mmHg across the SAAC. She was considered an appropriate candidate for surgical repair of the abdominal aortic coarctation.

4.3.2 Imaging data

Preoperative anatomy and hemodynamic data were obtained using duplex Doppler ultrasonography, computed tomography angiography (CTA) and phase contrast magnetic resonance imaging (PC-MRI). CTA imaging revealed a SAAC of 15 mm in length, with a 2.5 mm anterior-posterior diameter, and no renal artery involvement (**Figure 4.1**). The celiac artery (CA) and superior mesenteric artery (SMA) arose from the coarctation itself, and both exhibited ostial narrowings. Extensive collaterals circumvented the coarcted aorta, with an intact inferior mesenteric artery (IMA) being the dominant source of blood flow to the intestines. The internal mammary arteries were enlarged and communicated with the epigastric arteries that had multiple collaterals to the lower extremities and abdominal visceral organs. MRI examinations performed at 10-day and 1-year after the TAB provided postoperative data for analysis.

4.3.3 Thoracoabdominal bypass

The basis for choosing a TAB over a PA was that the 2.5 mm diameter of the coarctation and the involvement of the CA and SMA would have made an aortoplasty inordinately challenging and risky. In this case a midline abdominal incision was made from the xiphoid to the pubis, followed by medial visceral rotation of the left colon, to provide exposure of the entire abdominal aorta.

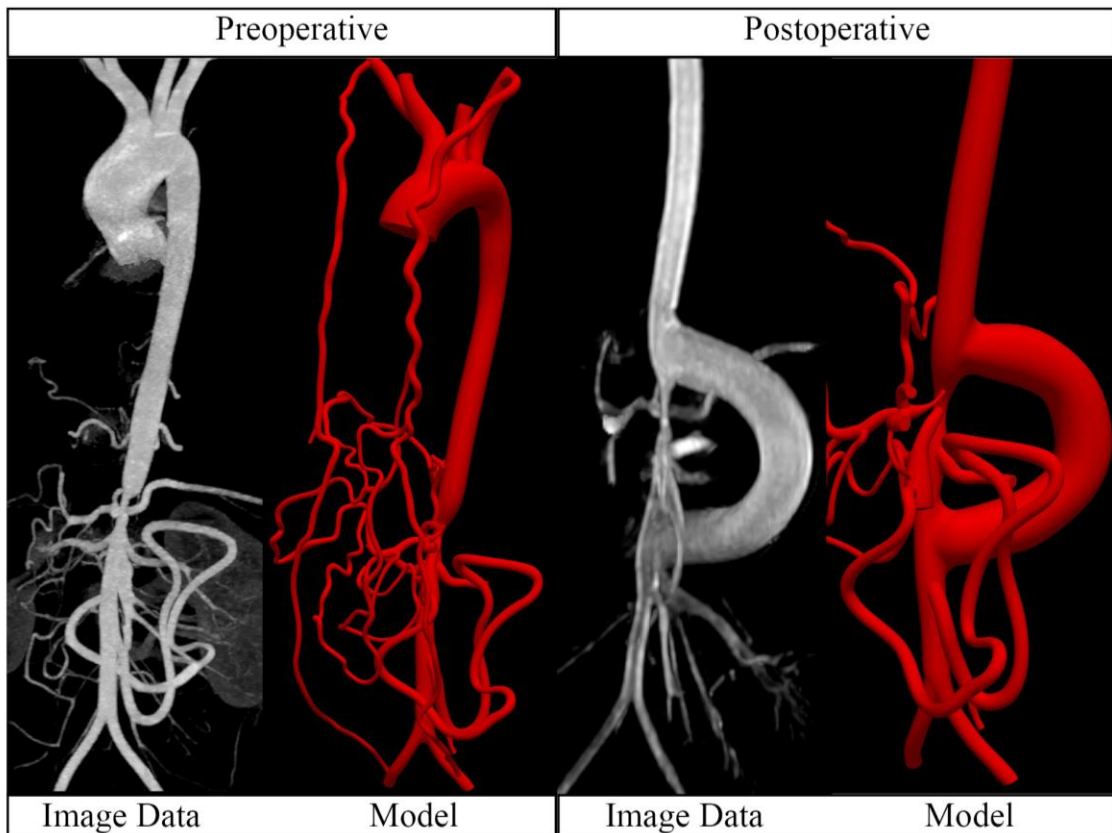


Figure 4.1 Preoperative (left) and postoperative (right) image data and corresponding computational models.

The supra celiac aorta was occluded with a Satinsky clamp, following which a 14 mm polytetrafluoroethylene (PTFE) bypass graft was anastomosed to a lateral aortotomy. The proximal aorta was occluded for 17 minutes during which time blood flow to the lower extremities and abdominal viscera, although reduced, was maintained through the preexisting large retroperitoneal and abdominal wall collaterals. The graft was then clamped just beyond its aortic

origin and antegrade aortic blood flow was restored following removal of the supraceliac aortic clamp. The graft was passed behind the left kidney and then anastomosed in an end-to-side manner to a lateral aortotomy just above the IMA (**Figure 4.1**). During the distal anastomosis, the infrarenal aorta was occluded for a time similar to that of the proximal anastomosis.

4.3.4 Kidney size

Preoperative and 10-day postoperative kidney volumes were measured using semi-automatic segmentation tools in Mimics version 21.0 (Materialise NV, Leuven, Belgium).

4.3.5 Computational modeling

Patient-specific FSI simulations [190] were performed to assess preoperative blood flow and compare the hemodynamic performance of TAB versus PA using a “virtual testing” paradigm [191]. First, a preoperative model was created and calibrated to match the anatomical and hemodynamic clinical data (**Figure 4.2**). Then, the calibrated preoperative model was adapted to reflect six surgical interventions (**Figure 4.3**), including three different TABs with 12 mm, 14 mm and 16 mm diameters, respectively (TAB-12mm, TAB-14mm and TAB-16mm); and three different PAs producing increases in aortic diameters of 0%, 30% and 50% (PA-0%, PA-30% and PA-50%) relative to the native aorta. Additionally, a control case was constructed by adjusting the preoperative model to produce a healthy anatomy without coarctation and collateral vessels (**Figure 4.4**). All models were constructed from the CTA image data using open-source cardiovascular modeling software CRIMSON [192]. Besides the vascular anatomy, each FSI model requires specification of arterial wall material properties (thickness and stiffness) as well as outflow boundary conditions at each branch. These boundary conditions represent the compliance and resistance of the distal vasculature not included in the anatomical model. The wall properties

and outflow boundary conditions were calibrated to match the simulation results with the clinically acquired flow and pressure data and achieve reasonable regional flow distributions (**Figure 4.2**) [193].

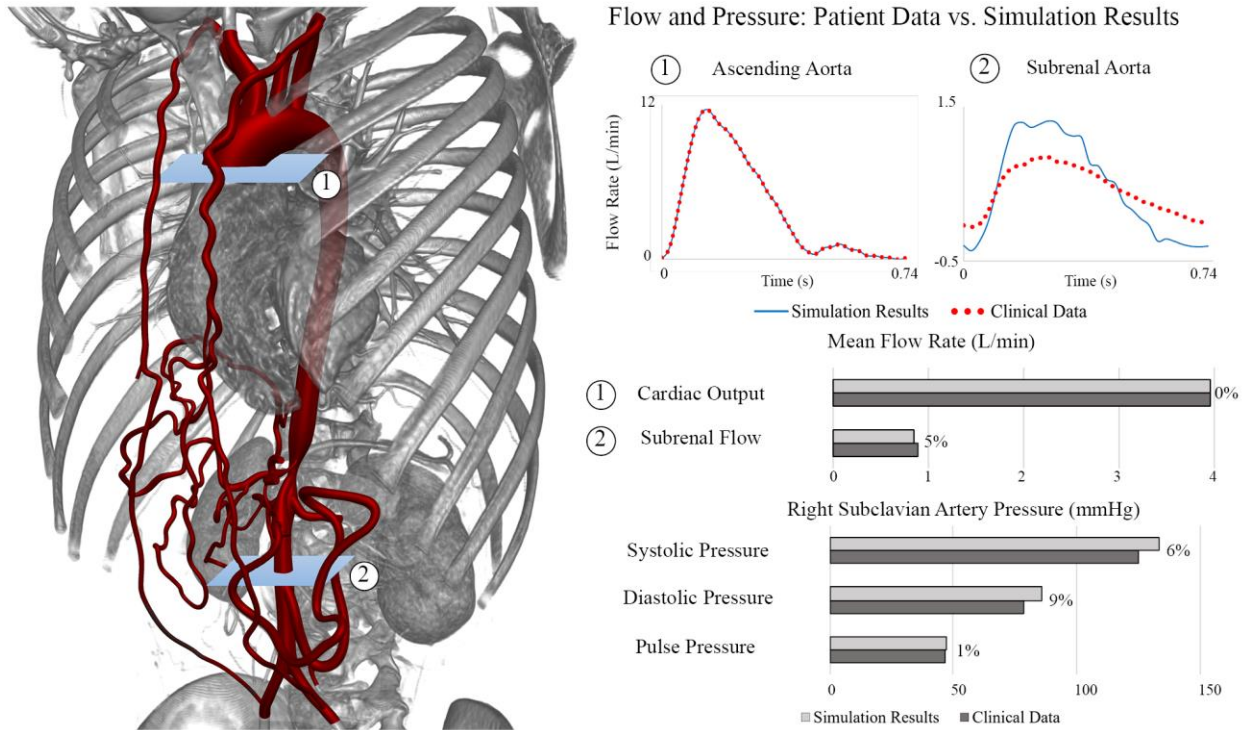


Figure 4.2 Left: Preoperative anatomy containing the PC-MRI planes (1 and 2) at which the flow measurements were acquired. Right: Comparison between the clinically measured flow and pressure data, and the simulation results in the validated preoperative model.

The methods for specification of the boundary conditions and material properties are reported in detail in the Appendix. In the control case, the boundary conditions were tuned to match the preoperative flow splits and a blood pressure appropriate for this patient’s size and age (96/65 mmHg) [194]. In the postoperative models, cardiac output and outflow boundary conditions were kept the same as preoperative; with the exception of the supra-aortic arteries, where the outflow boundary conditions were adjusted to reproduce literature data on regional flow splits [195].

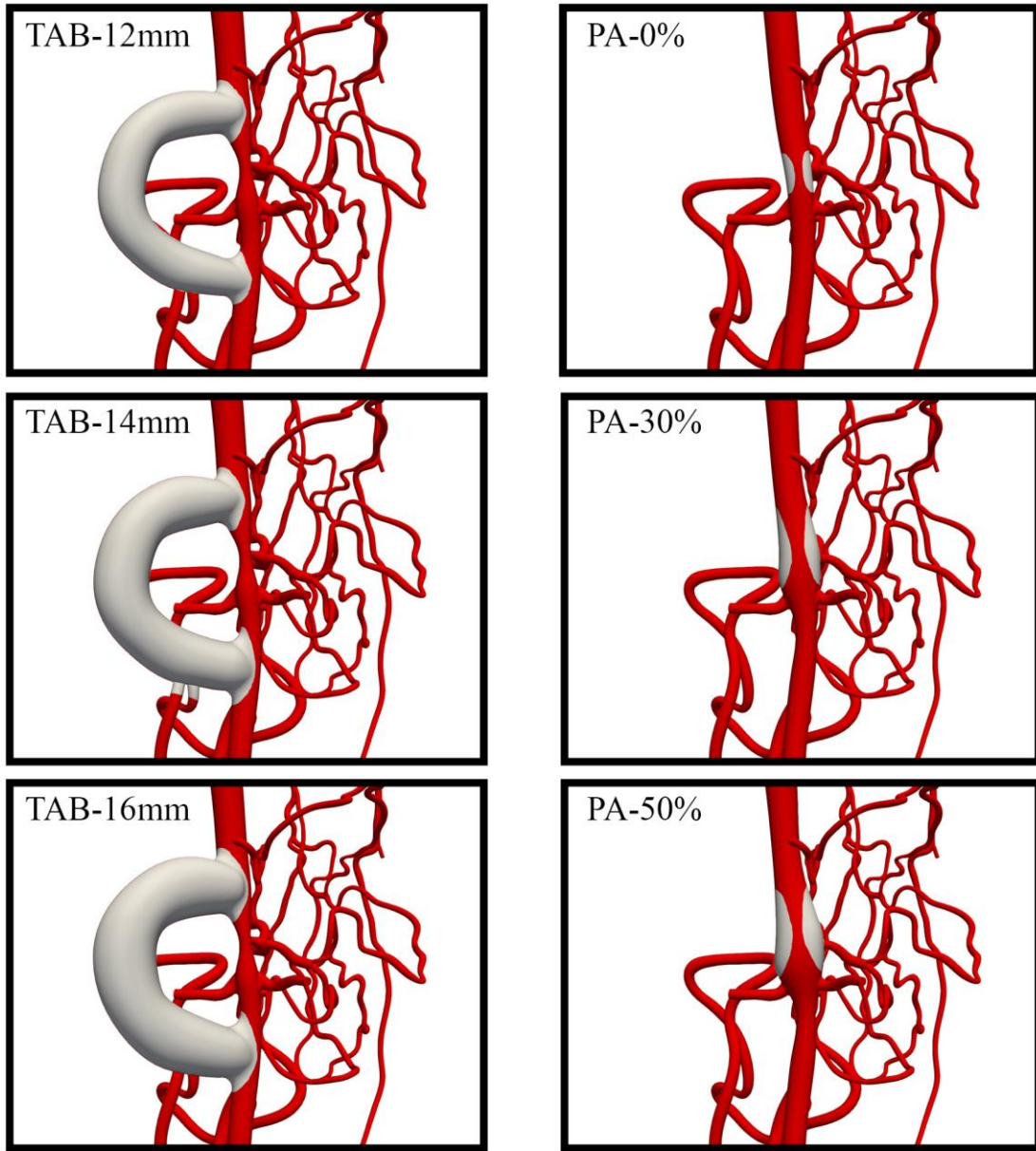


Figure 4.3 Close-up posterior views of the abdominal coarctation region and the renal arteries of all TAB (left) and PA (right) surgical options. Graft material of the bypass and patch is presented in gray.

Blood was modeled as an incompressible Newtonian fluid with a density of $1,060 \text{ kg/m}^3$ and a dynamic viscosity of $4.0 \text{ Pa}\cdot\text{s}$. Computations were performed using the CRIMSON Navier-Stokes flow solver on 160 cores at the University of Michigan high-performance computing cluster ConFlux. Simulations were run until cycle-to-cycle periodicity was achieved in the pressure fields,

this typically took three to five cycles. Computation time per cardiac cycle was approximately 48 hours.

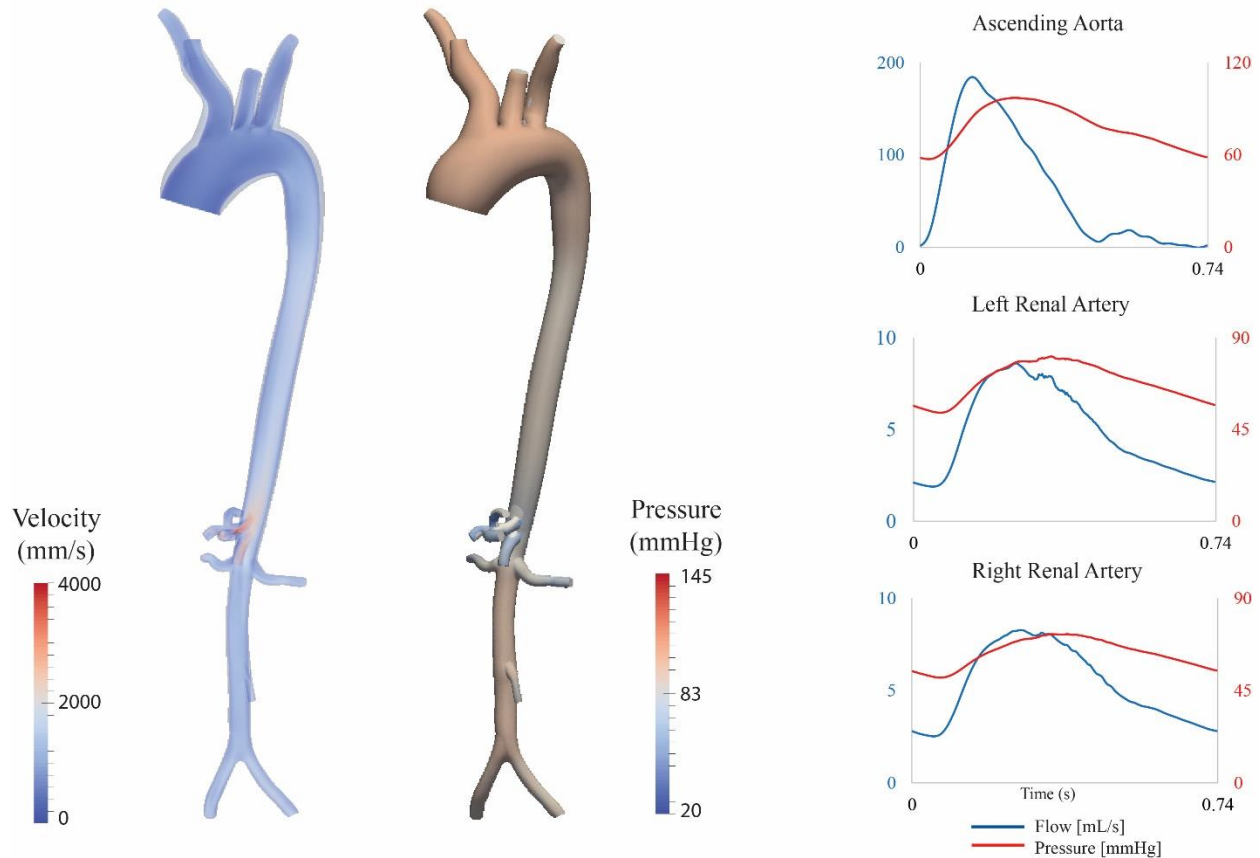


Figure 4.4 Left: 3D maps of preoperative hemodynamics in peak systole. Right: flow (blue) and pressure (red) waveforms in the ascending aorta, left renal artery, and right renal artery.

4.4 Results

4.4.1 Postoperative course

Complete resolution of the patient's lower extremity discomfort was evident in the early postoperative period. Her serum creatinine which ranged from 0.48 to 0.57 mg/dL preoperatively, decreased to 0.28 to 0.3 mg/dL postoperatively. However, she remained mildly hypertensive during her postoperative hospitalization, and at 1-year follow-up she remained on a low dose calcium channel blocker with resting blood pressures in the 110-115/65-70 mmHg range.

4.4.2 Preoperative simulation

The baseline preoperative model successfully reproduced the patient's hemodynamic data, as documented in a comparison between clinical data and simulation results at different locations in the circulation (**Figure 4.2**). The computed flows were all within 5% of the clinically measured data, and computed pressures were within 10%.

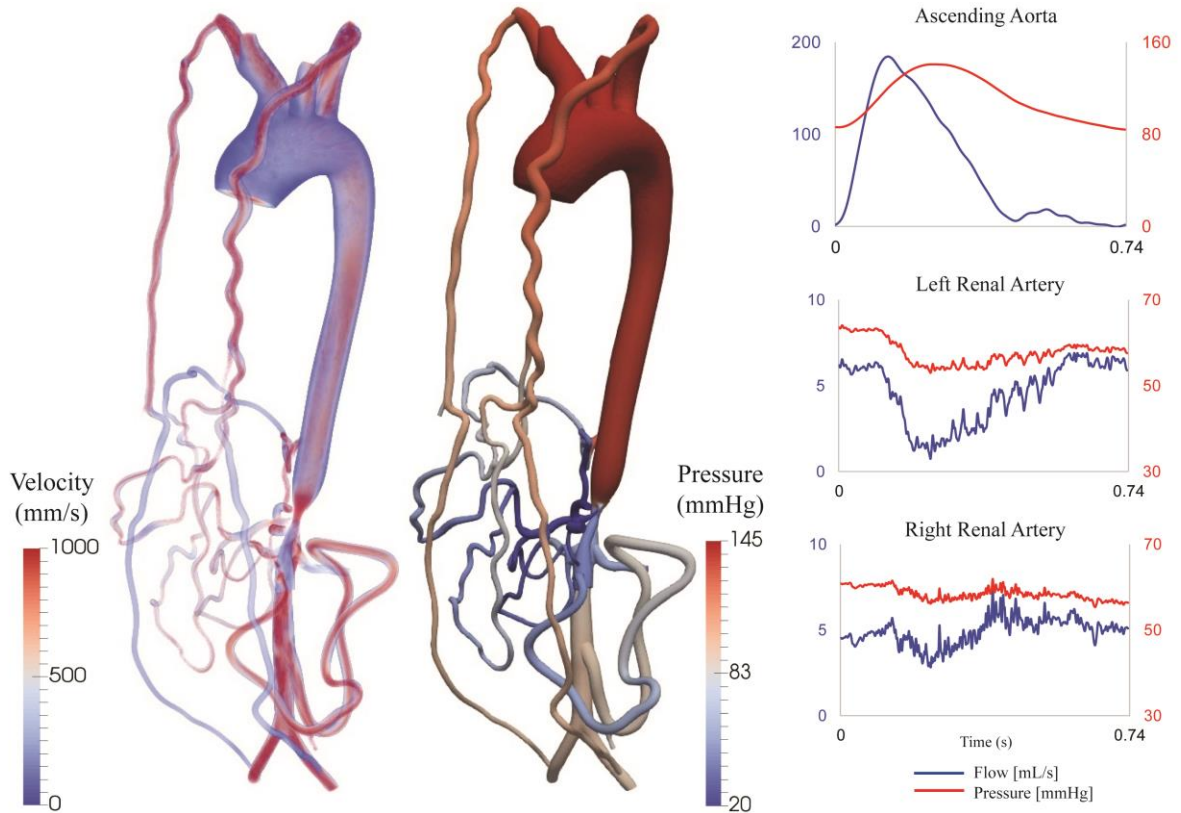


Figure 4.5 Left: 3D maps of preoperative hemodynamics in peak systole. Note the high velocities and large pressure gradient through the coarctation. Right: flow (blue) and pressure (red) waveforms in the ascending aorta, left renal artery, and right renal artery.

The FSI simulation results revealed a pressure gradient of 55 mmHg across the coarctation at peak-systole (**Figure 4.5**), which matched the pressure gradient derived from duplex Doppler ultrasonography (58 mmHg). Additionally, disturbed flow patterns were present distal to the coarctation which propagated into the renal arteries. Assessment of the renal artery flow and

pressure waveforms revealed diastolic dominated renal flows with high frequency oscillations (**Figure 4.5**). Renal artery pressure was markedly lower than ascending aortic pressure.

In the control case, systolic dominated renal flows without high-frequency disturbances were found. The results for the control anatomy are presented in **Figure 4.4**. A direct comparison of the pressure and flow waveforms between preoperative and control cases is reported in **Figure 4.6**.

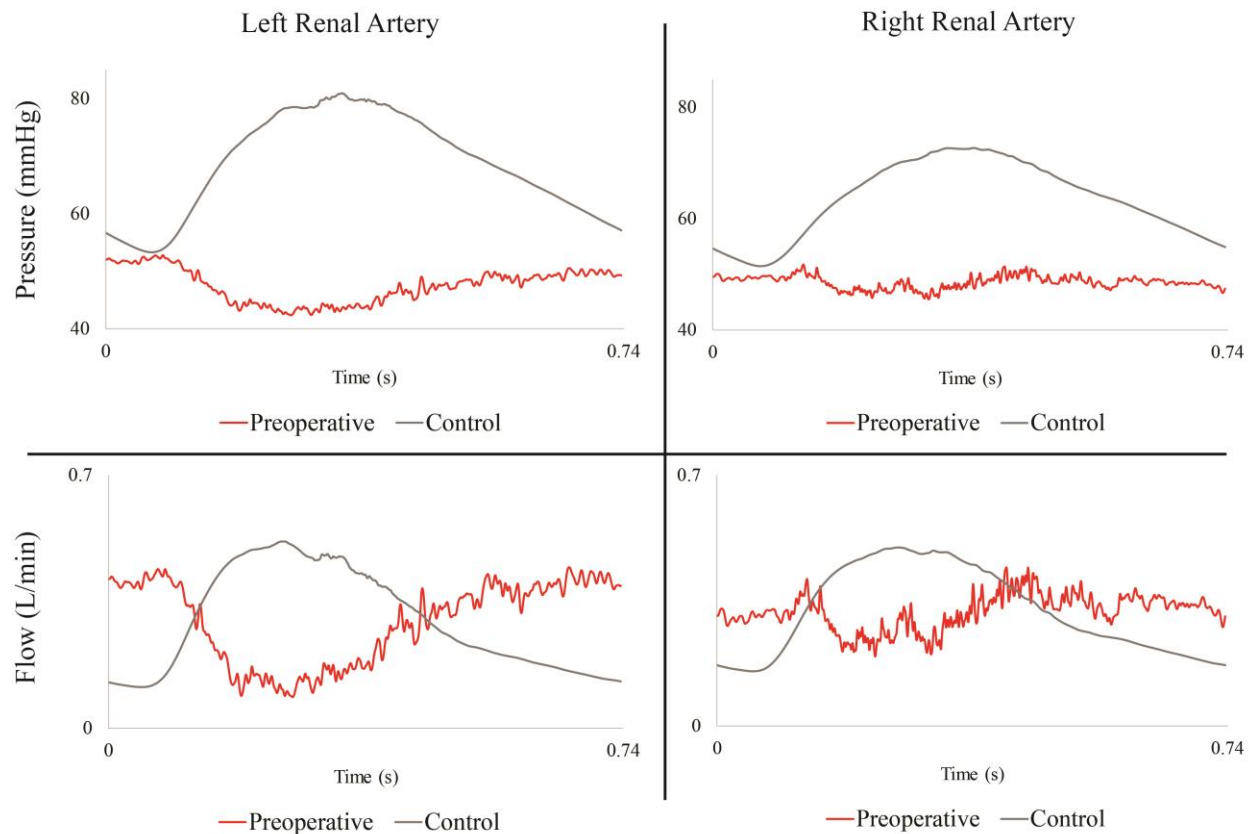


Figure 4.6 Comparison of the renal artery waveforms between the preoperative and control case shows that removal of the pathologic anatomy results in higher renal pressures, elimination of the high-frequency disturbances and systolic dominated waveforms.

4.4.3 Postoperative simulations

The computed mean flows at the outlets of the preoperative model and all six surgical repair models (**Table 4.1**) were revealing. All six interventions successfully reduced pressures at the ascending aorta (**Figure 4.7**) and increased renal artery flow rates (**Table 4.1**). Furthermore,

all surgical repairs resulted in systolic dominated flow waveforms (**Figure 4.8**), with a reduction of the high frequency flow and pressure disturbances in the renal arteries (**Figures 4.8 and 4.9**). Although most postoperative simulations retained some degree of the high frequency oscillations, the PA-0% eliminated the high frequency oscillations completely.

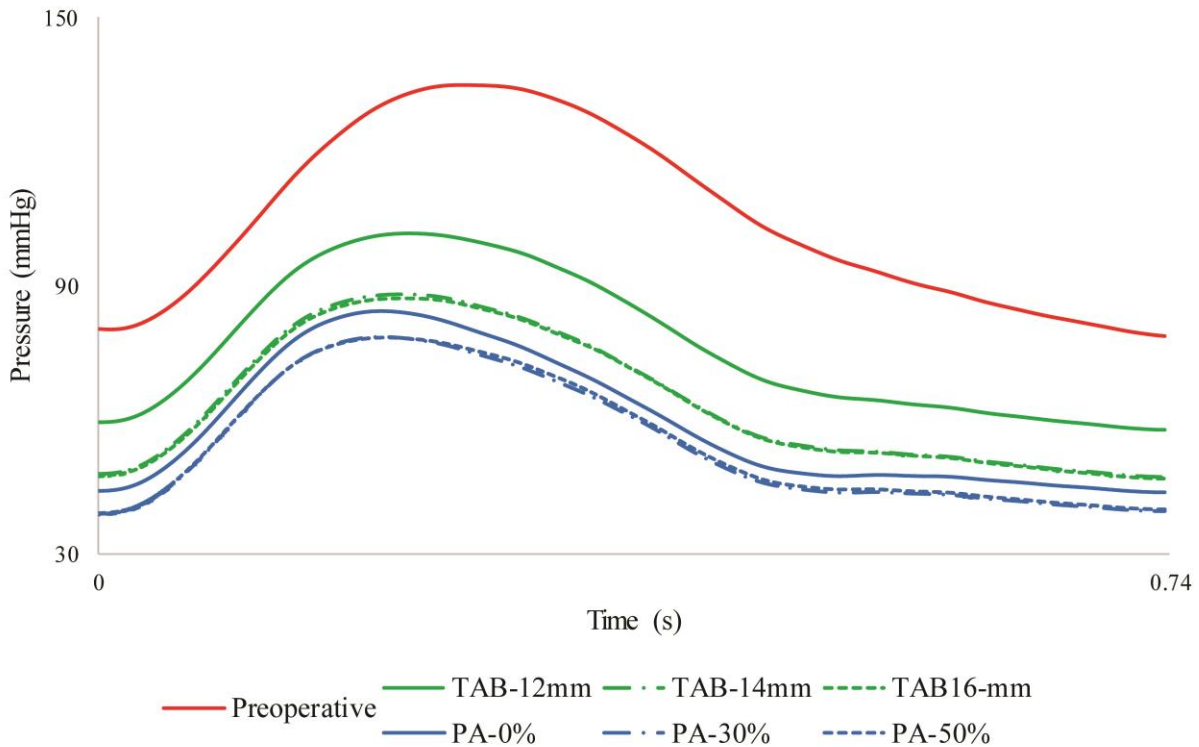


Figure 4.7 Ascending aortic pressure waveforms in all models. All postoperative models exhibited an important pressure reduction compared to the preoperative state. PA procedures resulted in a greater decrease of aortic pressure compared to TAB procedures.

The flow waveforms from the TAB-14mm simulation were compared with the PC-MRI data at 1-year follow-up (**Figure 4.10**). The patient’s cardiac output decreased during follow-up (-13%, from 3.9 to 3.2 L/min). The shape of the waveform changed as a result of a reduction in ventricular afterload following surgery. The computed (TAB-14mm) and 1-year follow-up PC-MRI data on flow through the bypass documented an excellent match: the percentages of cardiac

output through the bypass were 38% and 39% for the computations and the PC-MRI data, respectively.

Table 4.1 Simulated mean flow rates in mL/min.

Vessel	Preop	TAB-	TAB-	TAB-	PA-0%	PA-30%	PA-50%
		12mm	14mm	16mm			
Left Common Carotid Artery	275	351	319	308	321	344	356
Left Subclavian Artery	269	330	305	295	305	328	336
Right Common Carotid Artery	276	351	320	309	321	344	357
Right Subclavian Artery	274	325	306	296	305	328	331
Superior Mesenteric Artery	573	566	528	534	551	557	580
Left Gastric Artery	292	207	265	273	262	233	212
Splenic Artery	300	175	249	257	267	227	219
Hepatic Artery 1	98	50	94	101	94	80	60
Hepatic Artery 2	159	84	128	124	127	108	101
Left Renal Artery	291	394	370	374	353	360	360
Right Renal Artery	313	337	345	350	331	331	317
Inferior Mesenteric Artery	91	84	78	79	75	74	76
Left Iliac Artery	278	255	230	233	226	227	230
Right Iliac Artery	282	262	236	239	232	231	235
Renal Flow	605	732	715	724	684	691	677
		(+21%)	(+18%)	(+20%)	(+13%)	(+14%)	(+12%)
Mesenteric Flow	1421	1082	1263	1289	1301	1206	1173
		(-24%)	(-11%)	(-9%)	(-8%)	(-15%)	(-17%)
Cerebral Blood Flow	551	702	639	617	642	688	713
		(+27%)	(+16%)	(+12%)	(+17%)	(+25%)	(+29%)

4.4.4 Kidney size

Considerable changes in the kidney length were noted at 10-day follow-up. To accurately quantify the change in kidney size, volumetric measurements of both kidneys were obtained (**Figure 4.11**). Right and left kidney lengths increased from 3.4 to 3.85 cm (+13%) and from 3.8 to 4.6 cm (+21%), respectively. Right and left kidney volumes increased from 50.3 to 79.6 cm³ (+58%) and 51.5 to 92.0 cm³ (+79%), respectively. The observed increments in kidney volume reflected the calculated increases in right and left renal flow from the TAB-14mm FSI analysis (+9% and +26%, respectively).

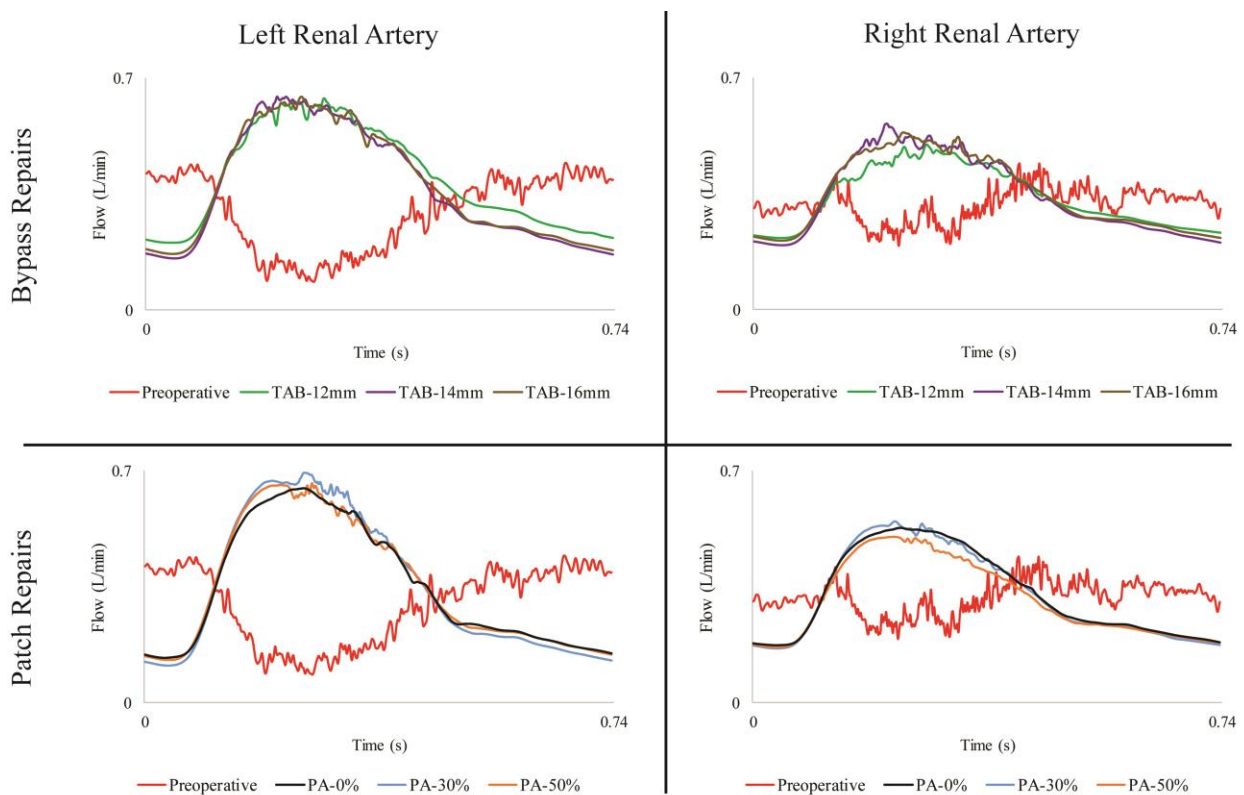


Figure 4.8 Renal flow waveforms in all models. Both TAB and PA resulted in restoration of systolic-dominated renal flows, reduction of high frequency disturbances and increased flow.

4.5 Discussion

Abdominal aortic coarctation is a rare vascular disease recognized most frequently in pediatric-age patients. The aortic narrowings are commonly associated with ostial stenoses of the celiac, superior mesenteric, and renal arteries [196]. This is clinically referred to as the middle

aortic syndrome, which manifests in most patients with drug therapy resistant arterial hypertension [197].

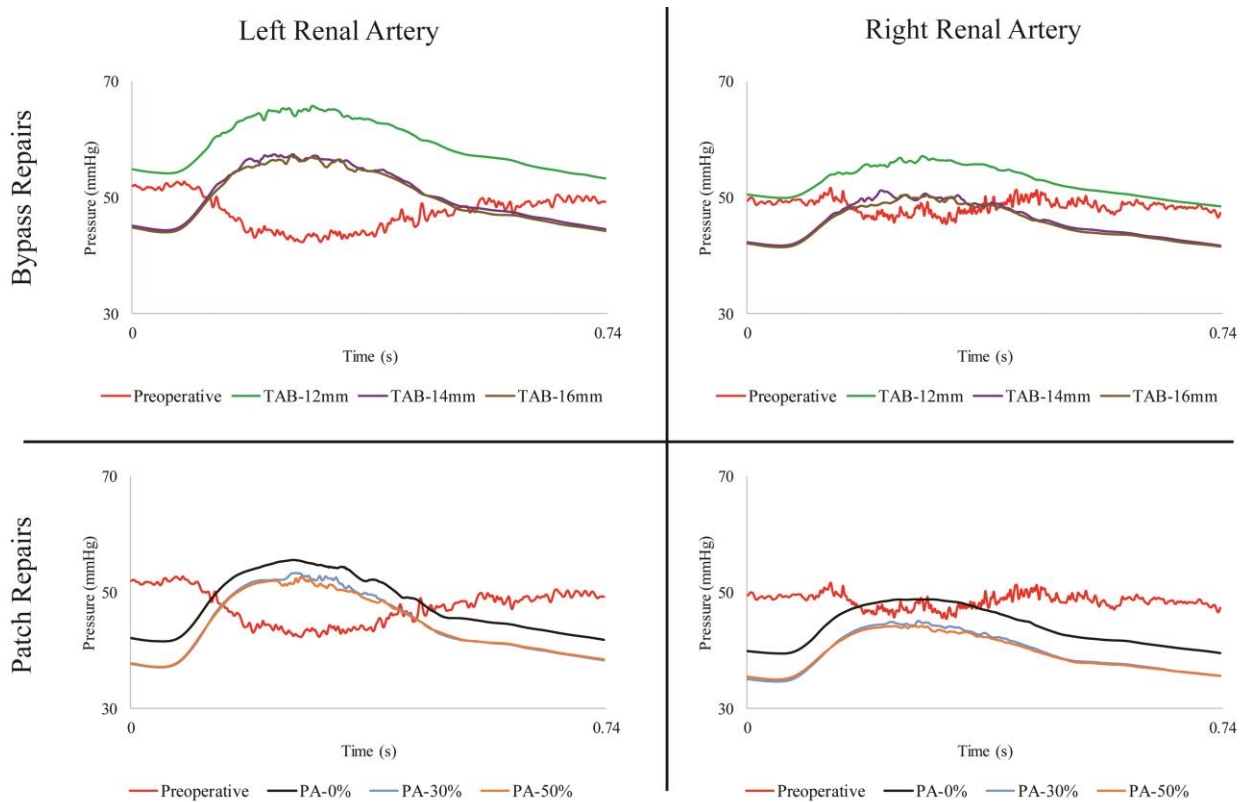


Figure 4.9 Renal pressure waveforms in all models. Most surgical repairs resulted in a reduction in renal artery pressures, associated with the large reductions in aortic pressures in all postoperative models.

Classic canine experiments noted that the location of the abdominal coarctation plays a key role in the presence of hypertension [57]. Hypertension is commonly observed in cases where the coarctation is suprarenal or involves the renal arteries. Conversely, hypertension is mostly absent when the coarctation is distal to the renal arteries. An investigation by Scott and Bahnson [198] of canine hypertension due surgically induced coarctation of the aorta that resulted in hypertension at five to seven weeks, noted that transposition of a kidney to a level above the coarctation and contralateral nephrectomy resulted in disappearance of hypertension. These earlier experiments suggest that disturbed aortorenal blood flow contributes to hypertension in abdominal coarctation.

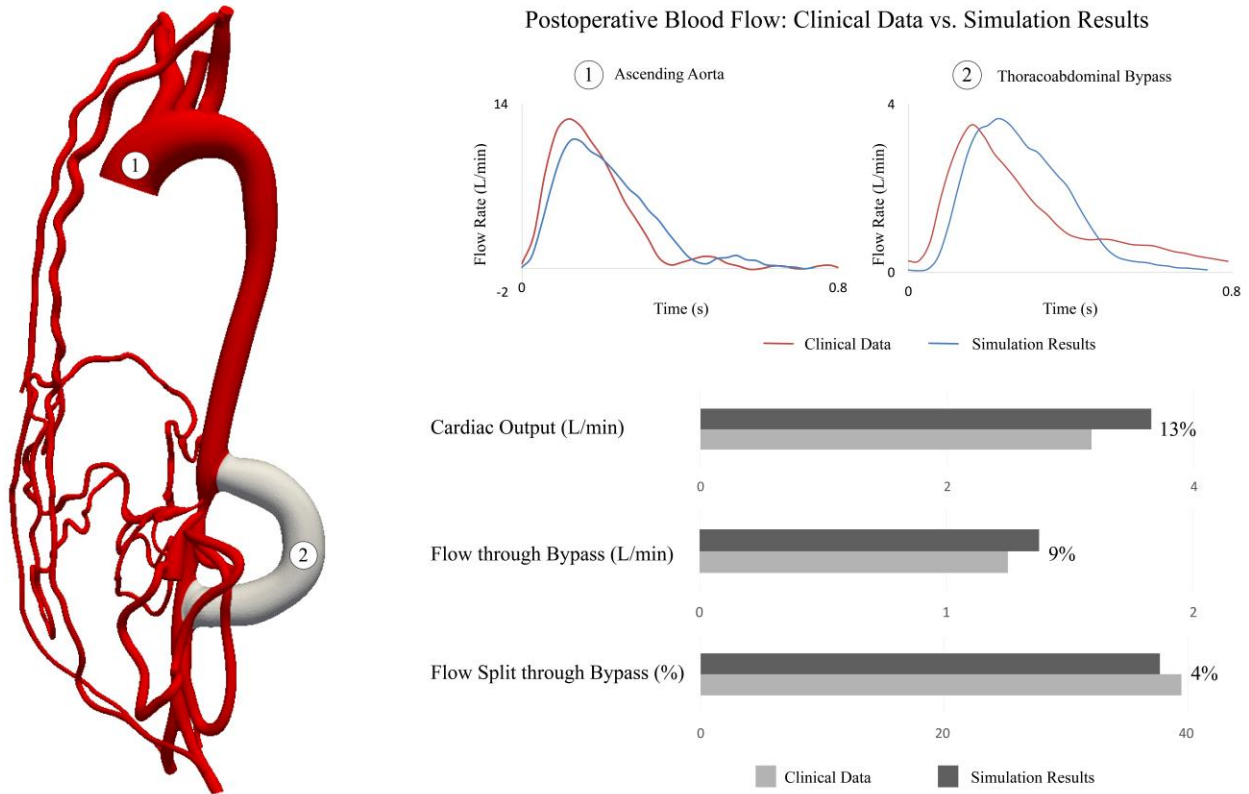


Figure 4.10 Comparison of the flow waveforms from the TAB-14mm simulation results and PC-MRI imaging data at 1-year follow-up.

When treating middle aortic syndrome, conventional surgical reconstructive procedures and catheter-based interventions are favored over long-term drug therapy [59], [188], [199]–[202]. Operative planning is usually derived solely from preoperative imaging [203]. Surgical decisions are often based on technical issues at hand, rather than aiming to restore normal aortorenal blood flow. Unfortunately, endovascular balloon dilation with or without stenting of abdominal aortic narrowings has had limited use with mixed early results and few long-term successes. Open operations, such as TAB and PA, have been the most common form of treating abdominal aortic coarctations. These operations often lead to improved hypertension control, yet most cases still depend on antihypertensive therapy to maintain normal blood pressures for gender and age.

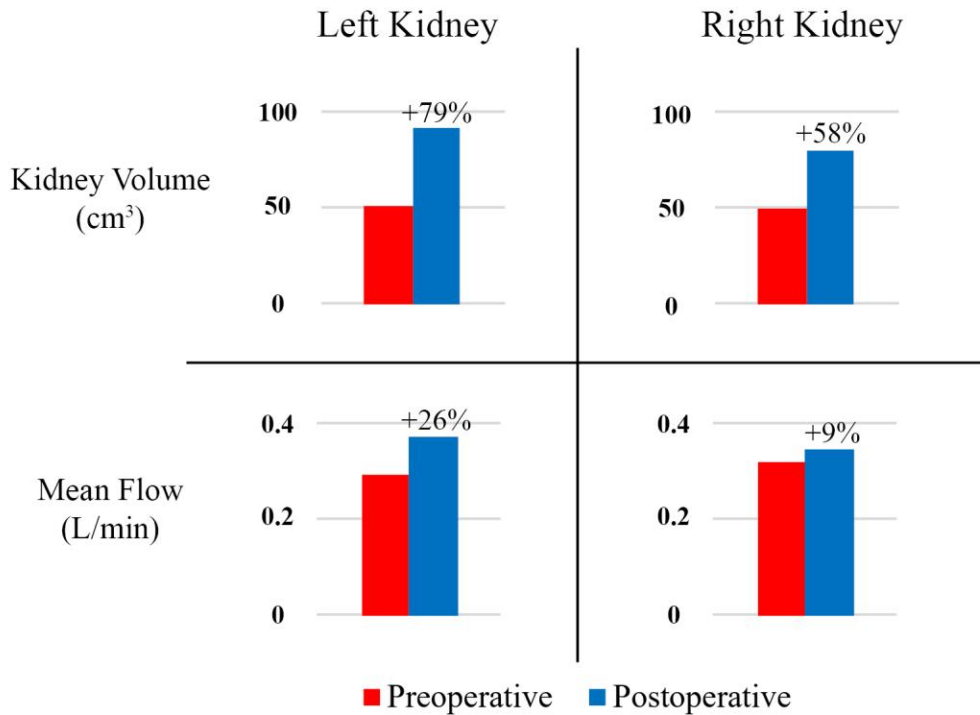


Figure 4.11 Comparison of the flow waveforms from the TAB-14mm simulation results and PC-MRI imaging data at 1-year follow-up.

Many factors go into decision making for performing a PA versus a TAB. A PA is favored in most instances of a limited aortic coarctation distant from the CA, SMA and renal arteries. When assessing the long-term benefits of PA in younger patients, the patch is intentionally oversized to account for the child's expected growth. Nevertheless, the appropriate degree of patch oversizing has not been established. Likewise, the effects on renal artery blood flow accompanying a disproportionately enlarged aorta following a PA are unknown.

A TAB is the procedure of choice when treating more severe coarctations with abdominal aortic diameters of only a few millimeters. In this case, a PA would have near-overlapping sutures from the lateral walls of the patch. In the past, the authors have recommended a wide range of TAB diameters related to age, with the intent that the bypass diameter would at least be 60% to

70% of the predicted adult aorta [59]. These recommendations may be logical, but as noted with PA oversizing, the science behind such is meager.

4.5.1 Clinical experience

Recently, the authors reviewed their experience with 155 children having renal artery stenotic disease and renovascular hypertension [187]. Hypertension outcomes were better in children treated with renal artery reconstructions alone compared to those requiring additional aortic procedures. The hypertension cure, improved, and failure rates in patients without aortic pathology (n=98) were 50%, 34% and 16%, respectively. These outcome rates were 33%, 59% and 8% in patients additionally treated with PA (n=28); and 35%, 50% and 15% in patients additionally treated with TAB (n=29). Given the poorer outcomes in patients undergoing concomitant aortic procedures, one must question whether abnormal aortorenal flow remains after surgery, and if differences exist between surgical repair with TAB and PA.

4.5.2 Computational modeling

Computational modeling is a widely used method in engineering fields that can be applied to study complex flow dynamics. Image-based computational tools have been developed for cardiovascular disease research [204], [205], medical device evaluation and, more recently, virtual planning of surgical interventions [42], [48], [89], [143]. While in other engineering fields the ‘virtual testing’ paradigm has largely replaced the traditional ‘build-and-test’ (e.g. trial and error) paradigm, this is not yet the case in the medical field. As evident in the current investigation, the value of computational modeling is apparent in preoperative determination of the therapeutic impact of different sizes of TAB and PA in patients with the midaortic syndrome.

Computational modeling in this investigation provided data of much higher spatial (up to 0.05 mm) and temporal (0.025 ms) resolution than available in any contemporary imaging test. This high-resolution data revealed an unexpected and potentially relevant finding of high frequency disturbances in the renal arteries preoperatively that could explain an increased renin release in the kidneys, resulting in secondary hypertension. Persistent high frequency disturbances were also found in the postoperative models and might explain the continuing hypertension following both TAB and PA interventions in patients undergoing concomitant renal artery reconstructions.

Besides characterization of preoperative aortorenal blood flow, this study also analyzed the impact of different TAB diameters and degree of PA oversizing. In total, six different surgical treatment options were studied: three TAB diameters and three levels of PA oversizing. All surgical interventions resulted in reduced aortic pressures and increased renal flows with restoration of systolic-dominated waveforms.

An unexpected finding of this investigation was that most surgical repairs resulted in a reduction in renal artery pressures (**Figure 4.9**). This acute response of the system, which does not account for any auto-regulatory processes following the surgery, is reflective of the large reductions in aortic pressures in all postoperative models (**Figure 4.7**).

Importantly, various degrees of high frequency disturbances persisted postoperatively, the exception being the treatment with a 0% PA which eliminated the high frequency disturbances completely. These results suggest that excessive PA oversizing and TAB lead to high frequency disturbances that may contribute to continued renin-mediated hypertension.

In the TAB operations, the high frequency disturbances could be explained by the turbulent mixing of antegrade flow through the remaining aortic stenosis and retrograde flow through the

TAB. Changing the TAB graft diameter did not significantly impact the persistence of high frequency disturbances. Such flow abnormalities could explain why the patient in the present case report, who had undergone a TAB repair, was still dependent on anti-hypertensive medication at 1-year follow-up. In an oversized PA, the dilated segment of the reconstruction induces flow disturbances. Flow clearly shows complex recirculation and vortices in the region of the patch (**Figure 4.12**), similar to what is observed in aneurysmal disease. The absence of dilation in the PA-0% case explains the lack of disturbances in this model. Furthermore, it may also explain the reduced hypertension cure rates of renal artery revascularizations in the authors' larger series of patients requiring concomitant aortic procedures.

Historically, renin-mediated hypertension has been linked to low perfusion pressure and low renal blood flow [203]. The high frequency flow oscillations observed in the present work have not been described in the earlier literature. The most likely explanation for this is that contemporary clinical measurement devices lack the temporal resolution necessary to detect such high frequency flow oscillations. It has been recognized that Doppler ultrasonography, CTA and MRI can all be helpful in the evaluation of renovascular disease, but none have, at present, high enough sensitivity to rule out renovascular disease in a child with a suggestion of that diagnosis [206].

4.6 Limitations

The stiffness properties of the aortic wall could not be calculated with the available data in this study. Therefore, in the present investigation, the assigned stiffness parameters were derived from a previous study from our laboratory which characterized aortic stiffness in a cohort of pediatric patients with aortic coarctation [207]. In that study, the aortic stiffness was calculated using strain measurements from MRI and invasive pressure measurements from catheterization.

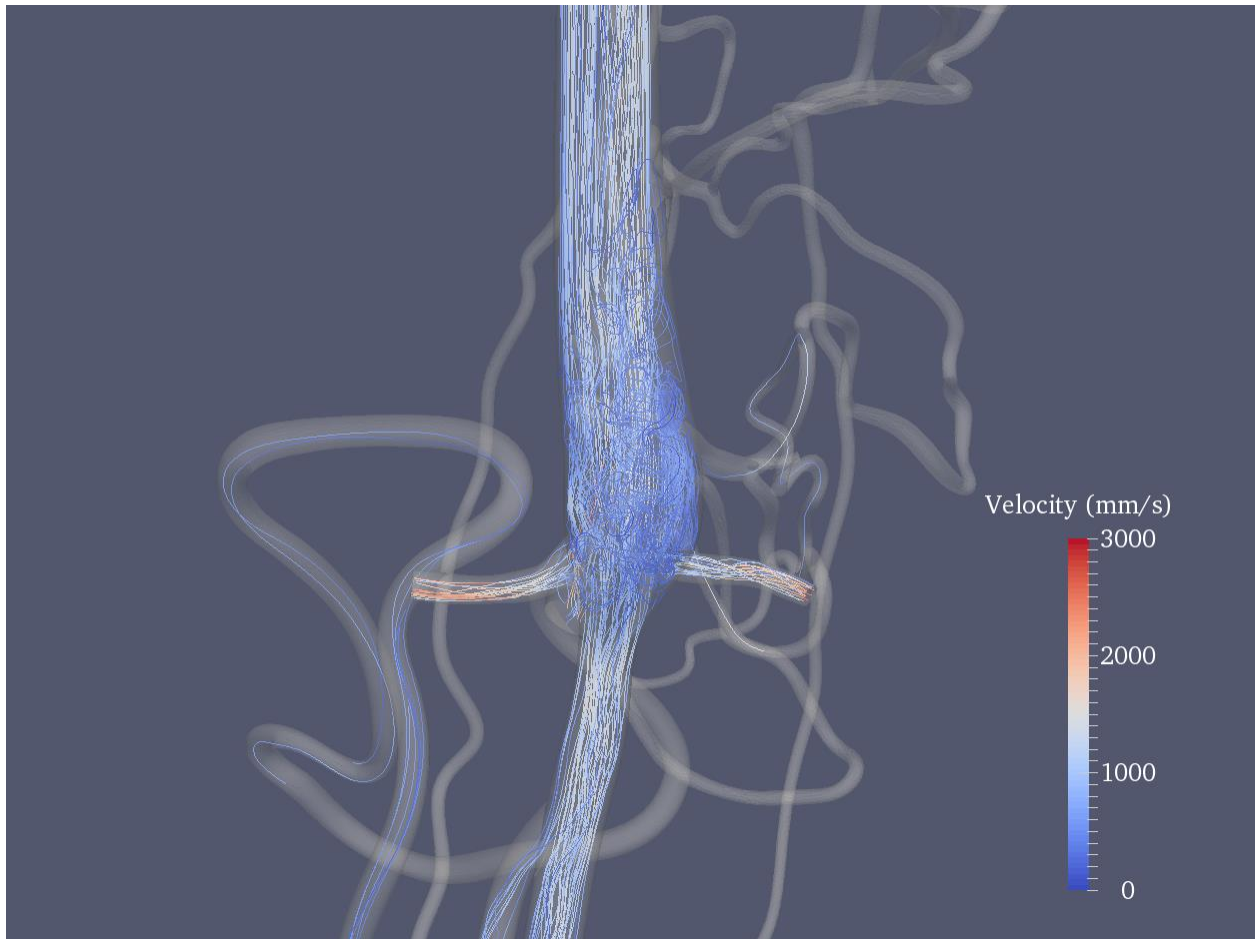


Figure 4.12 Velocity streamlines for the PA-50% model at mid-deceleration ($t=0.30$ s). Disturbed flow patterns are clearly evident in the region of the patch, propagating into the renal arteries.

This investigation analyzed aortorenal blood flow in a single patient with a suprarenal abdominal aortic coarctation. While the results for this patient were clinically-validated, performing the same analysis in patients with different anatomical features might result in different outcomes, including the presence of high-frequency disturbances in the renal arteries. Additionally, the causality between the high frequency disturbances and excessive renin release should be further investigated. Furthermore, we tested six different surgical interventions with arbitrary TAB and PA sizes. Performing a parametric study of other patch and bypass sizes and configurations could result in different outcomes

Furthermore, it is important to note that even though a specific intervention might theoretically render a better hemodynamic outcome, performance of the procedure itself may be inordinately challenging and risky, resulting in a technical failure and less successful outcome. Thus, acceptance of benefits defined by virtual testing must be tempered by clinical judgement and expertise.

Lastly, the results presented here do not take into account any of the vascular auto-regulations that undoubtedly occur after a vascular reconstruction. The magnitude of the waveforms, specifically the pressure, might change as a result of systemic vasoreactivity, although the high frequency disturbances are likely to persist.

4.7 Conclusions

This study has revealed the presence of high frequency disturbances in renal blood flow and pressure following operative interventions for SAAC. These previously unrecognized disturbances may be a fundamental contributor to continued abnormal release of renin, and thus the basis of the often-seen persistent post-operative hypertension in this patient population.

Considerable value resides in computational modeling of vascular surgery procedures. Patient-specific modeling provides high-resolution hemodynamic information for differing interventions, and allows preoperative planning for complex procedures, such as those accompanying aortic reconstructions in young patients with SAAC. Collaborative efforts between biomedical engineers and clinicians will be essential to providing accurate modeling and simulation of feasible surgical procedures in this setting.

Chapter 5 Interventional Planning for Endovascular Revision of a Lateral Tunnel Fontan

5.1 Original publication information

This chapter was originally published as a scientific article:

Ahmed, Y., Tossas-Betancourt, C., van Bakel, P. A., Primeaux, J. M., Weadock, W. J., Lu, J. C., Zampi, J. D., Salavitarbar, A., & Figueroa, C. A. (2021). Interventional planning for endovascular revision of a Lateral Tunnel Fontan: A patient-specific computational analysis. *Frontiers in Physiology, 12*. <https://doi.org/10.3389/fphys.2021.718254>

Changes made to the original document are mainly cosmetic to adhere to the format of this document.

5.2 Introduction

Hypoplastic left heart syndrome (HLHS), is a complex single ventricle congenital heart defect (CHD), characterized by the underdevelopment of the left heart, including left atrium, mitral valve, left ventricle, and aorta [208]. HLHS and/or HLHS-variants are estimated to affect 1,025 babies born in the United States each year [209]. In-hospital mortality rate is between 1 and 2%, while current data suggests 30-year survival of nearly 85% [210]. While management of single ventricle lesions has significantly improved over the last decades, HLHS and/or HLHS-variants remain one of the leading causes of death in neonates with CHD [211].

The current treatment paradigm for HLHS and/or HLHS-variants consists of multiple staged reconstructive surgeries, aimed at creating a Fontan circulation in which venous blood is

redirected into the lungs and oxygenated blood is pumped into the systemic circulation, supported by a single ventricle (i.e., the morphological right ventricle) [212]. Stage 1 Norwood procedure is typically performed at birth (**Figure 5.1A**). Alternatively, a less invasive hybrid Norwood (i.e., patent ductus arteriosus stenting and pulmonary artery banding) can be performed. A stage 2 superior cavo-pulmonary connection, which, depending on patient anatomy and/or institutional preference can either be a bi-directional Glenn or Hemi-Fontan procedure (**Figure 5.1B**), is performed at 4 to 6 months of age. Finally, stage 3 Fontan completion, creating a total cavo-pulmonary connection, is performed at 14 to 48 months of age. At our institution the preferred surgical approach for stage 3 Fontan completion in over 90% of cases consists of an intra-atrial lateral tunnel Fontan procedure [213], [214] (**Figure 5.1C**).

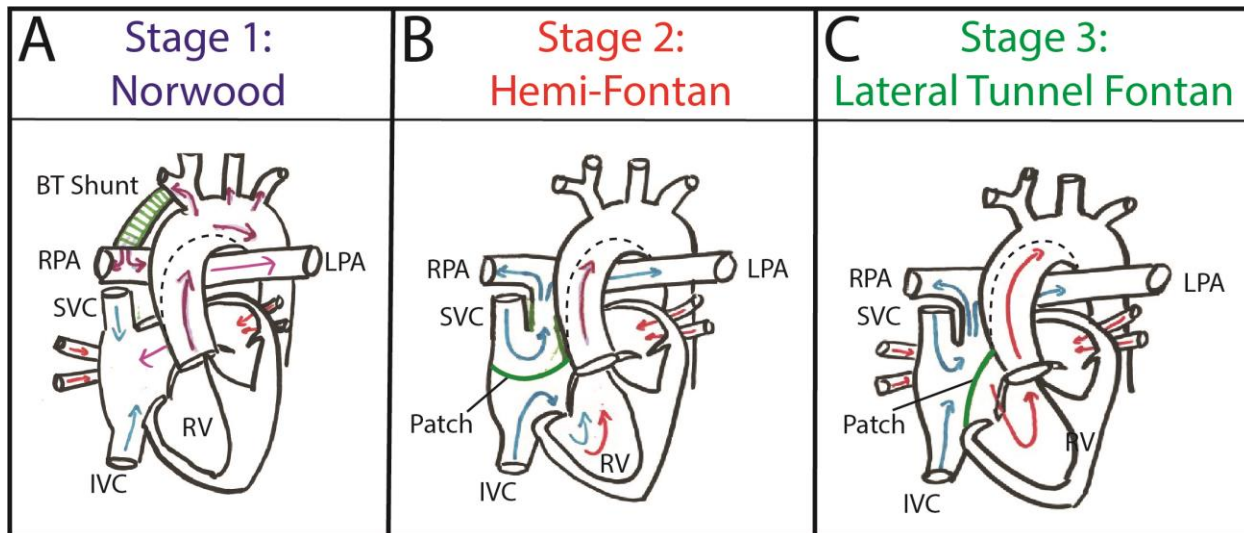


Figure 5.1 Patients with hypoplastic left heart syndrome typically undergo staged palliation consisting of 3 consecutive surgeries. (A) Stage 1: Norwood, (B) Stage 2: Hemi-Fontan, and (C) Stage 3: Lateral Tunnel Fontan.

Up to two-thirds of HLHS and/or HLHS-variants patients require surgical or transcatheter reintervention within 20 years of the initial staged surgeries, underlining the need for adequate lifetime surveillance [215]–[217]. Notable complications following the multi-stage surgical approach are arrhythmias, enlarged right atrium, prolonged pleural drainage, seizure, and protein-losing enteropathy (PLE) [218]. While surgical revision of the Fontan pathway can be performed

with low morbidity and mortality, minimally invasive therapeutic options in HLHS and/or HLHS-variants patients can be used to treat patients in frail condition [219]. Patient surveillance typically involves regular pediatric cardiology evaluations with echocardiograms and electrocardiograms. In addition, cardiac catheterization is utilized to assess if a patient is a candidate for each subsequent stage of the single ventricle palliation and to evaluate if there are significant anatomic or hemodynamic abnormalities post-surgery.

Computational fluid dynamics (CFD) is a well-established technique that has been widely used to study hemodynamics of cardiovascular diseases [15], and can be used to assess the hemodynamic effect of planned surgical interventions [42], [220]–[228]. In this work, we evaluated the feasibility of an endovascular repair considered by the pediatric cardiology team at the University of Michigan C.S. Mott Children’s Hospital to treat a 2-year-old patient with single ventricle CHD presenting with a dilated Fontan pathway and associated PLE. CFD tools were combined with clinical data on anatomy, flow, and pressure to construct a pre-intervention fluid-structure interaction (FSI) model. Then, this model was modified by introducing a custom bifurcated endograft to connect the inferior vena cava (IVC) with the superior vena cava (SVC) and pulmonary arteries. Different indices of hemodynamic performance pre- and post-intervention were obtained to assist the clinical team with determining the course of treatment for this patient.

5.3 Methods

This study was approved by the University of Michigan Institutional Review Board (HUM00155491).

5.3.1 Patient’s history

A 2-year-old female with complex HLHS-variant single ventricle CHD (double outlet right ventricle, hypoplastic left ventricle and aortic arch, and malposed great arteries) presented at our institution with new-onset failure to thrive, pleural effusions, fluid overload and hepatomegaly with concern for PLE. Previously, this patient had undergone pulmonary artery band placement in the neonatal period, followed by a Hemi-Fontan procedure at 6 months of age. At 20 months of age, the patient underwent a Lateral Tunnel Fontan procedure. Concomitantly, a fenestration to the right atrium was created to alleviate pressure in the Fontan pathway, as is common practice at our institution.

As part of the initial work-up for new-onset PLE, an invasive cardiac catheterization was performed, which revealed elevated mean pressures of ~15 mmHg in the Fontan pathway. The patient was found to have low arterial oxygen saturation (81%) and borderline low cardiac index of 2.4 L/min/m². Angiography showed hepatic venous reflux, and severe dilation of the inferior segment of the Fontan pathway between the IVC and branch pulmonary arteries with inefficient swirling flow.

5.3.2 Rationale for proposed endovascular repair

Following thorough evaluation of the patient, the dilation in the Fontan pathway was believed to be the cause of the increased pressures, hepatic venous reflux, subsequent hepatomegaly and new-onset PLE. Revision of the Fontan pathway was indicated, aiming to decrease its size, relieve the hepatic venous reflux, and improve flow to the pulmonary arteries. Due to the frail condition of the patient, the clinical team considered open surgical Fontan revision not to be a suitable option. Instead, a minimally-invasive endovascular revision was considered. This approach entails the deployment of a custom-made endograft to redirect blood flow through the Fontan pathway. A collaboration between biomedical engineering and pediatric cardiology

aimed to understand the viability of the proposed endovascular approach, by combining CFD tools with the available clinical data.

5.3.3 Clinical data acquisition

A magnetic resonance imaging (MRI) study was performed using a 1.5 T Ingenia scanner (Philips, Best, the Netherlands) with the patient under deep sedation. A free-breathing, ECG-gated, respiratory navigator gated, 3D mDIXON (1.4 mm isotropic voxel size) sequence was performed to acquire the vascular anatomy. The diastolic phase of the 3D MRI data was used to reconstruct the cardiovascular anatomy. Cardiac-gated phase-contrast MRI (PC-MRI) was performed at the SVC, IVC, left pulmonary artery (LPA), and right pulmonary artery (RPA). Flow and luminal area waveforms (consisting of 40 phases, voxel size 1.2 mm, slice thickness 6 mm) were processed from the PC-MRI data using the CVI₄₂ software (Circle Cardiovascular Imaging, Calgary, Canada). Invasive catheterization was performed to acquire pressure waveforms at the IVC, Fontan pathway, SVC, LPA and RPA.

5.3.4 Computational analysis

A pre-intervention 3D model of the Fontan pathway, including the IVC, SVC, LPA, RPA and fenestration to the right atrium was constructed (**Figure 5.2A**) using the open-source cardiovascular simulation software CRIMSON [85]. Lumen center lines, and 2D segmentations of the vessel lumen (**Figure 5.2B**) were used to create a computer aided design (CAD) model of the cardiovascular anatomy using lofting and blending operations (**Figure 5.2C**). The CAD model was then discretized into a finite element mesh composed of tetrahedral elements (**Figure 5.2D**).

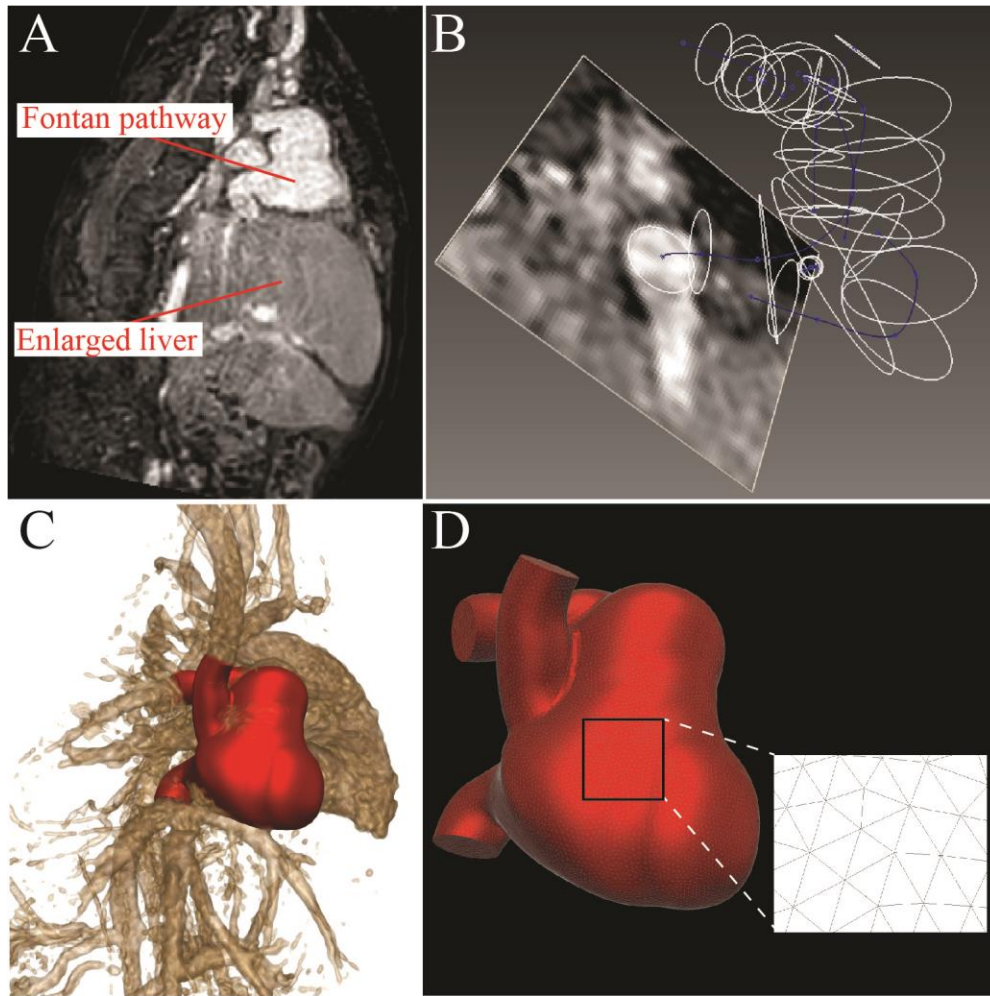


Figure 5.2 A model of the Fontan pathway was constructed from MRI data (A). Path lines and vessel contours were used to delineate and loft the vessels (B), which were blended to create an anatomical model (C), and subsequently discretized to create a FE mesh.

To model the endovascular repair, the pre-intervention model was modified by introducing a custom bifurcated endograft that connects the IVC, SVC, and pulmonary arteries. The custom bifurcated endograft consist of a 10 mm graft (main body) spanning between the IVC and the ostium of the pulmonary arteries, and an 8 mm limb was deployed into the SVC (**Figure 5.3**). The proposed endovascular repair also included excluding the fenestration between the Fontan pathway and the right atrium. The bifurcated endograft was assigned a stiffness of 12 MPa and thickness of 0.22 mm [229].

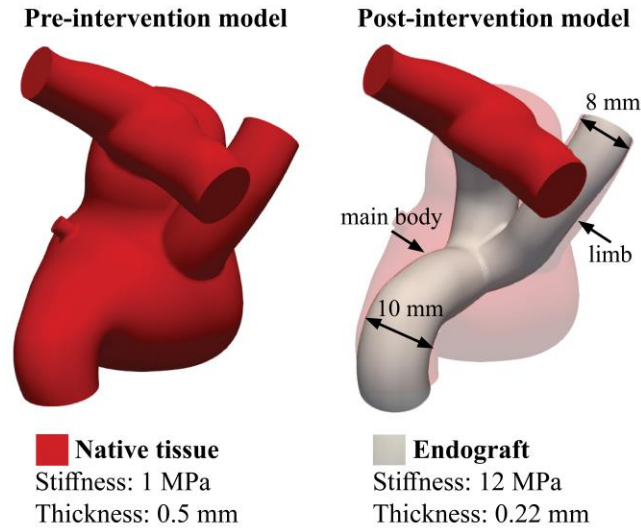


Figure 5.3 Distribution of stiffness and thickness of the pre- and post-intervention models. The introduction the endograft blocks the fenestration, which was therefore excluded from the post-intervention model.

5.3.4.1 Multi-scale modeling approach

A 3D-0D open-loop modeling approach was adopted to describe hemodynamics pre- and post-intervention (**Figure 5.4**). Lumped-parameter models (LPM) (0D) were used to represent inflow and outflow boundary conditions [86]. This approach made it possible to simulate pre- and post-intervention conditions without directly imposing any of the measured pressure and flow waveforms. The parameters of the 3D-0D open-loop model are calibrated to reproduce pre-intervention hemodynamic data such as regional flow splits, IVC pressure, and backflow volume per beat, which was believed to contribute to the patient’s hepatomegaly and PLE. These parameters remain unchanged for the post-intervention model. Therefore, any differences in global hemodynamics between the models are the direct consequence of the different geometry and material properties of such model.

For the inflow, a single ventricle heart model (red box) was placed in series with 3-element Windkessel models representing the upper body vasculature (UBV, green box), and lower body vasculature (LBV, brown box), respectively. For the outflows, 3-element Windkessel models were

coupled to the LPA, RPA, representing the pulmonary circulation (blue boxes) and the fenestration (purple box).

The single ventricle heart model contains circuits representing the right atrium (RA), tricuspid valve (TV), right ventricle (RV), aortic valve (AV), and aortic root (AR). The TV was modeled using a diode and inductor in series. The active contraction of the ventricle was modeled using a ‘two-Hill’ time-varying elastance function [144]:

$$E_{RV}(t) = k \left(\frac{g_1}{1 + g_1} \right) \left(\frac{1}{1 + g_2} \right) + E_{min}$$

where

$$g_1 = \left(\frac{t}{\tau_1} \right)^{m_1}, \quad g_2 = \left(\frac{t}{\tau_2} \right)^{m_2}, \quad k = \frac{E_{max} - E_{min}}{\max \left[\left(\frac{g_1}{1 + g_1} \right) \left(\frac{1}{1 + g_2} \right) \right]}$$

k is a scaling factor used to ensure that the minimum and maximum elastance values of the ‘two-Hill’ elastance match the values of the clinically-measured minimum and maximum elastance. Minimum elastance was calculated by dividing ventricular end-diastolic pressure (7 mmHg) over end-diastolic volume (31 mL), whereas the maximum elastance was calculated by dividing ventricular end-systolic pressure (105 mmHg) over end-systolic volume (16 mL). m_1 and τ_1 control the slope and time translation of the ascending portion of the elastance waveform, respectively. m_2 and τ_2 control the slope and time translation of the descending portion of the elastance waveform, respectively. The aortic valve was represented through a dynamically-controlled resistor and inductor, see [230]. The final values of the heart model parameters are reported in **Table 5.1**.

The resistance and capacitance values of these models were iteratively tuned until the mean flow at the IVC, SVC, LPA, RPA, retrograde volume per beat at the IVC, LPA, and RPA, and the

pressure waveform at IVC were matched to the available clinical data. The values of the LPM parameters are reported in **Table 5.2**.

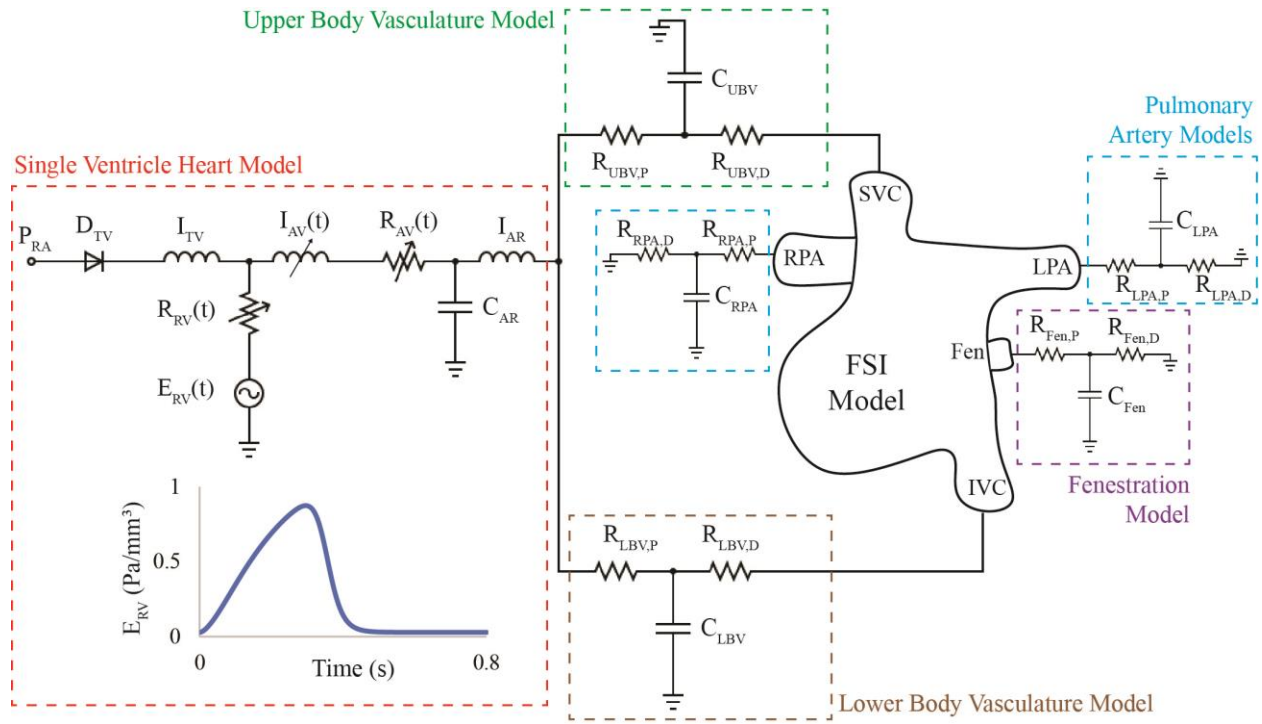


Figure 5.4 3D-0D open loop model of the HLHS patient includes an FSI model of the Fontan circulation containing venae cavae, pulmonary arteries and fenestration, and lumped-parameter network of models.

Wall deformation of the 3D anatomy was modeled using the coupled momentum method [231]. The stiffness of the 3D model was simultaneously tuned, together with the Windkessel model parameters of the circuits, to match the backflow measured at the IVC, LPA, and RPA within 7% of the clinical data. The calibrated wall stiffness and thickness were 1 MPa and 0.5 mm, respectively (**Figure 5.3**).

Pulsatile FSI simulations were conducted using CRIMSON’s Navier-Stokes flow solver on 60 cores of the University of Michigan’s high-performance computing (HPC) cluster ConFlux. Blood was modeled as an incompressible Newtonian fluid with a density of 1.06 g/cm³ and a dynamic viscosity of 4.0 Pa·s. Simulations were run until cycle-to-cycle periodicity in hemodynamic results was achieved. Mesh refinement was performed using an adaptive field-based

technique [137] until the hemodynamic results were independent of mesh size. The reported results of the pre-intervention and post-intervention models use refined meshes consisting of 1,754,964 and 1,813,505 elements, respectively.

Table 5.1 Parameter values and units for components of the single ventricle heart model. The time constants are expressed in terms of the cardiac cycle length ($T = 0.8$ s).

Elastance waveform parameters							
E_{MAX} [Pa mm ⁻³]	E_{MIN} [Pa mm ⁻³]	T [s]	τ_1 [s]	m_1 []	τ_2 [s]	m_2 [s]	
0.875	0.03	0.8	0.4944T	2.6	0.5493T	18	
Heart model parameters							
P_{RA} [Pa]	R_{TV} [Pa s mm ⁻³]	I_{TV} [Pa s ² mm ⁻³]	C_{AR} [Pa mm ⁻³]	I_{AR} [Pa s ² mm ⁻³]			
629	1.1x10 ⁻⁵	1.0x10 ⁻⁵	0.5	2.0x10 ⁻⁶			
Parameters for $I_{AV}(t)$, $R_{RV}(t)$, and $R_{AV}(t)$							
A_{ANN} [mm ²]	P_{OPEN} [Pa]	P_{CLOSE} [Pa]	K_{VO} [Pa ⁻¹ s ⁻¹]	K_{VC} [Pa ⁻¹ s ⁻¹]	M_{RG} []	M_{ST} []	L_{EFF} [mm]
60	0	1333	0.2	0.2	0.5	1.0	15
ρ [g mm ⁻³]	K_S [s mm ⁻³]						
0.00106	1.5x10 ⁻⁶						

5.3.5 Energy dissipation

Energy dissipated (E_{diss}) was computed using the energy fluxes [232],

$$E_{diss} = E_{in} - E_{out}$$

where,

$$E_{in} = \sum_i^{N_{inlets}} Q_i \left(P_i + \frac{1}{2} \rho V_i^2 \right),$$

$$E_{out} = \sum_j^{N_{outlets}} Q_j \left(P_j + \frac{1}{2} \rho V_j^2 \right).$$

N_{inlets} and $N_{outlets}$ are the number of inlet (SVC and IVC) and outlet (LPA, RPA, and fenestration) faces in the model, respectively. Flow rates (Q) were integrated over each face, and velocities (V) and pressures (P) were spatially averaged over each vessel face. The blood density (ρ) was 1.06 g/cm³. The energy efficiency was defined as,

$$E_{eff} = \frac{E_{out}}{E_{in}}$$

Energy dissipated was nondimensionalized using the formula given by [233],

$$e_{diss} = \frac{E_{diss}}{\epsilon_0}$$

where,

$$\epsilon_0 = \frac{\rho * Q^3}{BSA^2}$$

The body surface area (BSA) of the patient was 0.51 m².

Table 5.2 Calibrated parameter values of Windkessel models.

Vessel	R _P (Pa·s·mm ⁻³)	C (mm ³ ·Pa ⁻¹)	R _D (Pa·s·mm ⁻³)
Upper Vasculature	0.1047	4.0000	0.1684
Lower Vasculature	0.1847	0.9000	0.0884
Left Pulmonary Artery	0.0040	7.1974	0.3995
Right Pulmonary Artery	0.0054	9.3408	0.2668
Fenestration	0.2517	1.3703	1.4265

5.4 Results

5.4.1 Pre-intervention model

The pre-intervention FSI model successfully reproduced patient-specific hemodynamic data, see **Figure 5.5**. Simulation results matched IVC, SVC, LPA, and RPA flow data within 2%. Retrograde volume per beat, a key hemodynamic parameter in understanding the observed symptoms in this patient, was matched within 7% of clinical data acquired at the IVC, LPA, and RPA. Systolic, diastolic, and mean pressures were matched within 5% of clinically acquired pressures at the SVC, IVC, LPA, and RPA.

The sum of the inlet and outlet energy fluxes was 2.39 x 10⁷ g mm² s⁻³ and 2.11 x 10⁷ g mm² s⁻³, respectively. Therefore, the energy flux dissipated in the system was 0.27 x 10⁷ g mm² s⁻³, resulting in an energy efficiency of 88%. The nondimensionalized energy dissipation was 3.46 x 10⁸. Furthermore, assessment of velocity field streamlines showed re-circulation within the

Fontan pathway (**Figure 5.6**), specifically in the enlarged pouch, which contribute to the observed dissipation of energy.

5.4.2 Post-intervention model

When comparing pre- and post-intervention hemodynamics, the endovascular repair led to a 6% and 7% mean pressure increase and 29% and 43% pulse pressure increase at the IVC and SVC, respectively (**Figure 5.7**). Pressures at the pulmonary arteries were increased slightly in the post-intervention model (4% mean pressure increases for both RPA and LPA).

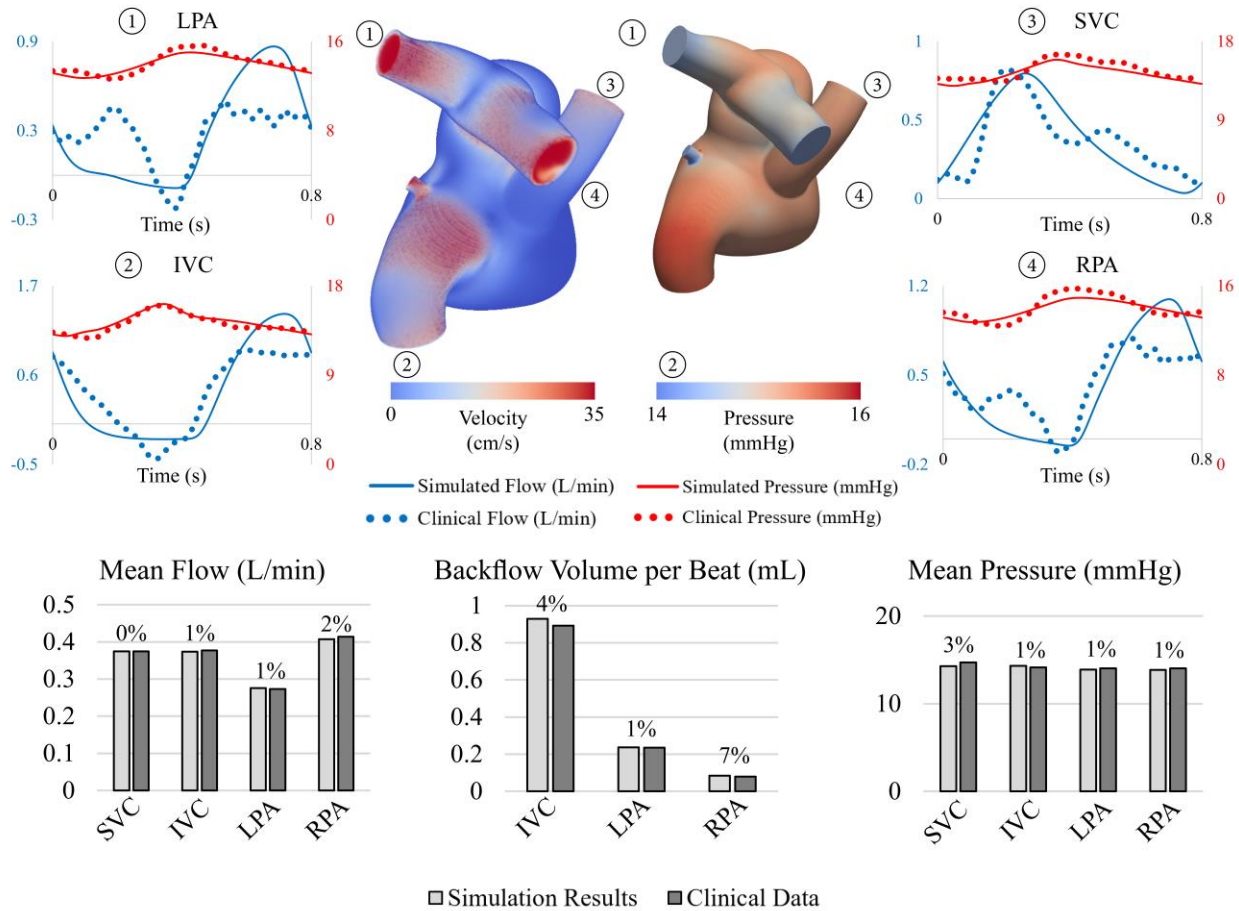


Figure 5.5 Top: Velocity volume rendering and pressure contour at systole. Comparison between flow and pressure waveforms at the LPA, IVC, SVC, and RPA show good agreement. Bottom: Comparison between simulated results (light gray) and clinical data (dark gray).

The endograft repair also resulted in a 5% decrease in mean flows at the IVC and SVC. This decrease in mean inflow, together with the increase in pressure, reveals that the proposed endovascular Fontan revision has a larger intrinsic resistance to flow than the pre-intervention anatomy. This higher resistance is likely due to the smaller luminal diameters of the considered endografts. Furthermore, the exclusion of the fenestration in the post-intervention model led to a 4% in mean flow at the pulmonary arteries. The backflow volume per beat at the IVC, which was suspected to contribute to the hepatomegaly, increased by 6%, while a more notable increase in backflow was observed at the pulmonary arteries (17% and 22% increase at the RPA and LPA, respectively).

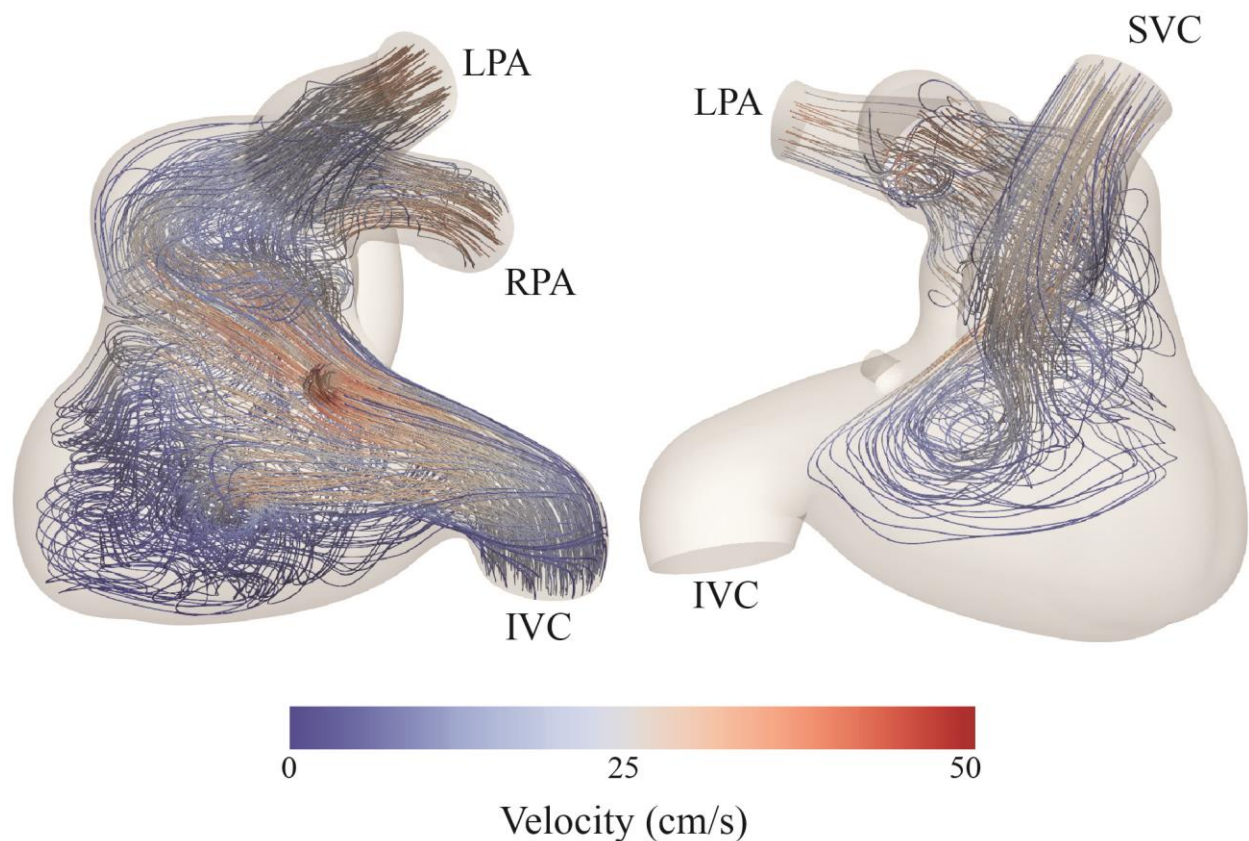


Figure 5.6 Velocity streamlines depict swirling flow and low velocities in the dilated portion of the Fontan pathway.

Energy flux dissipated within the post-intervention model was 54% smaller than in the pre-intervention model ($0.13 \times 10^7 \text{ g mm}^2 \text{ s}^{-3}$ vs $0.27 \times 10^7 \text{ g mm}^2 \text{ s}^{-3}$). Furthermore, the dimensionless

energy flux dissipated within the post-intervention model (1.85×10^8) was 47% smaller than in the pre-intervention model (3.46×10^8). This suggests that the post-intervention model is more efficient in preserving energy from the venae cavae to the pulmonary arteries.

5.5 Clinical decision making

Our hemodynamic assessment using CFD revealed that the proposed endovascular Fontan revision failed to reduce the pressure in the Fontan pathway and alleviate hepatic venous reflux. In fact, an increase in backflow volume and pressure was observed in the IVC and pulmonary arteries. Since these outcomes were deemed unfavorable for the patient, the clinical team decided to forgo the proposed intervention.

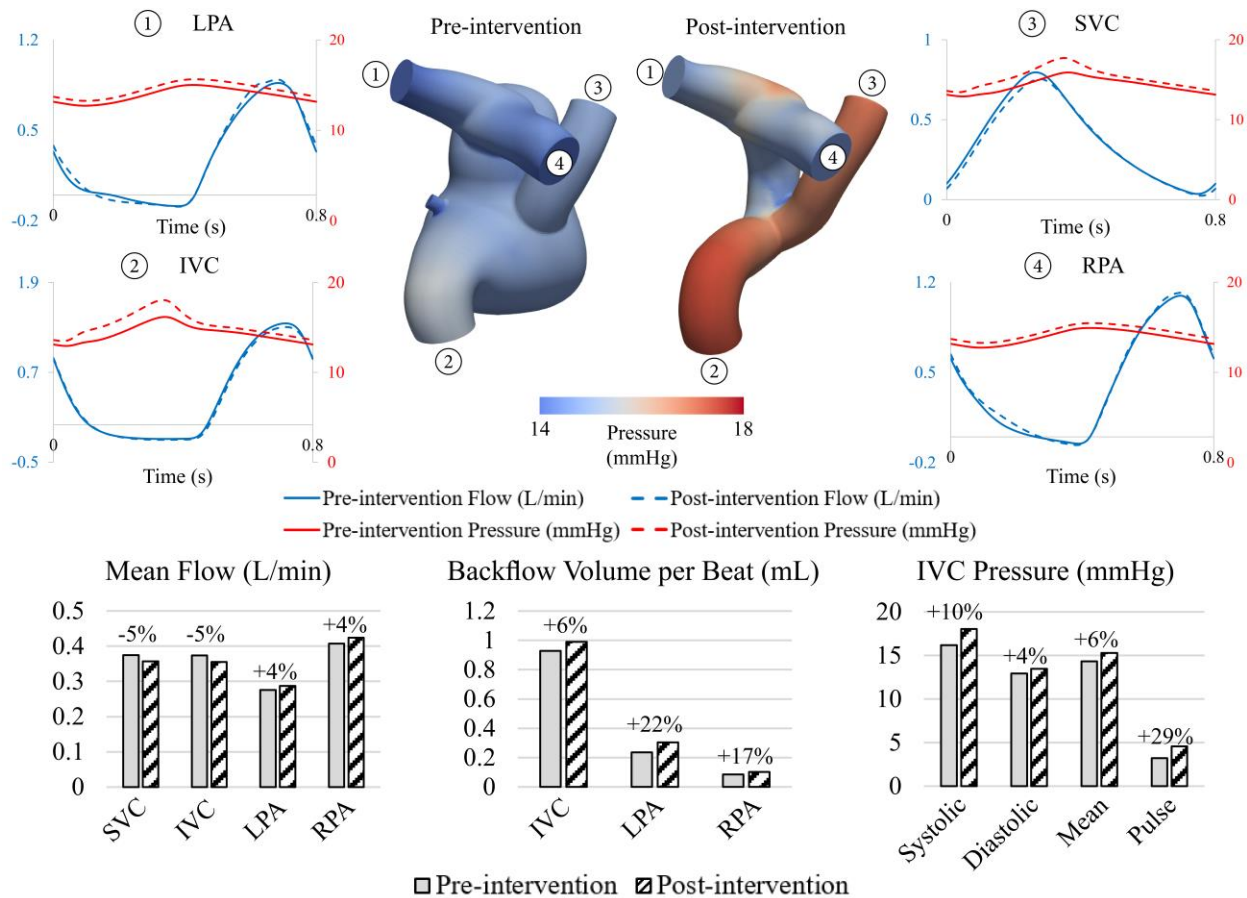


Figure 5.7 Comparison between pre- and post-intervention hemodynamics. Endovascular intervention led decreases in mean flow and increases in mean pressure at IVC and SVC and increases in backflow at the IVC.

Besides the predicted limited hemodynamic benefit of a transcatheter Fontan revision in this patient, this procedure would likely be highly technically challenging. Our initial concept was to modify commercially available covered stents and implant these stents in rapid succession to exclude the dilated portion of the Fontan pathway while maintaining flow from the SVC and IVC to the pulmonary arteries. We also considered using bifurcating endovascular grafts. However, these would also likely require customization/modification to fit the anatomy. Given the patient's age and size, it is unlikely that the peripheral vascular anatomy would accept the typical sheath sizes necessary for endovascular grafts. Lastly, besides limitations in equipment, we need to account for the expected somatic growth of this patient. As the patient grows, we would anticipate redilation of stents would be required and with stent dilation and migration, an endovascular leak could occur. Therefore, technical challenges further steered clinical decision making away from transcatheter Fontan revision in this patient.

5.6 Discussion

Fontan patients are faced with numerous complications during their lifetime, often requiring multiple reinterventions. A comprehensive preoperative assessment, which includes in-depth hemodynamic analysis, is therefore paramount in deciding adequate course of treatment. Patient-specific CFD modeling tools can be used to non-invasively describe the effects of planned interventions. Our group has demonstrated the clinical applicability of advanced computational modeling tools in prospectively aiding surgical planning [234], as well as evaluating the effect of several surgical interventions to treat cardiovascular disease [221], [235]–[237]. CFD in surgical planning for single ventricle CHD has been widely used [238]–[240], where authors successfully validated their post-operative models, built during surgical planning, with clinical data. While these studies employed advanced modeling techniques, such as coupling of 3-element Windkessel

models, and imposing pulsatile flow waveforms, the focus of these studies was on energy dissipation and pulmonary flow distribution, which justifies the choice of boundary conditions. However, in our study, we use a heart model at the inlet boundary [230]. A heart model allows the virtual intervention to not only affect inlet pressures, but also affect the inlet flow waveforms. The pulsatile nature of our model has been previously shown to result in a more accurate assessment of energy dissipation and hepatic flow distribution [241]. While work by [240] emphasized that, for prospective surgical planning applications, parameter fitting and validation could be an issue, all of our modeling assumptions have been informed by the available pre-operative clinical data to ensure a proper analysis.

In this work, we explored the feasibility of an endovascular Fontan revision of a 2-year-old CHD patient presenting with complications following Fontan palliation. The patient-specific workflow used in this study combined CFD modeling tools with clinical data to successfully represent the patient hemodynamics and subsequently simulate the proposed endovascular revision. To accurately capture the hemodynamic effects of the proposed endovascular repair, a 3D-0D open-loop modeling approach was adopted. This approach made it possible to simulate pre- and post-intervention conditions without directly imposing any of the measured pressure and flow waveforms. Parameters of the 3D-0D open-loop model were calibrated to reproduce pre-intervention hemodynamic data and remained unchanged for the post-intervention model. Therefore, any differences in global hemodynamics between the models are the direct consequence of the different geometry and material properties of the endograft. While a more complex design of the LPMs could have been employed to represent the different vascular beds, this would have led to a larger number of parameters to be estimated.

The proposed endovascular revision, while resulting in a locally more efficient pathway from the venae cavae to the pulmonary arteries (54% reduction in energy flux dissipated compared to pre-intervention conditions), led to an overall increase in resistance on the venous circulation, which resulted in increases in mean and pulse pressure at the IVC and SVC, and an increase in hepatic venous reflux. These findings are most likely explained by the combination of a decrease in luminal area and increase in structural stiffness following endograft introduction, leading to a loss of compliance in the Fontan pathway. It has previously been demonstrated that introducing a stiff endograft can adversely impact cardiac and arterial hemodynamics [90]. Even though the present work is focused on the Fontan pathway, a low-pressure system, our computational results show increases in pressure, similar to those encountered following TEVAR deployment in the thoracic aorta. These findings underline the importance of adequately assessing the hemodynamic impact of surgical interventions.

Computational tools have promising potential in the field of interventional planning, however, there are several aspects limiting widespread clinical use. First, virtual surgical planning is time consuming and computationally expensive. The analysis performed in this work was completed over a span of several months and required considerable computing power on a dedicated HPC. Second, the operator-dependent nature of the 3D model construction process could potentially result in variability in the geometric model shape and volume. This could subsequently lead to variability in certain hemodynamic indices such as energy dissipation, pressure, and flow. Third, while we were able to virtually assess the performance of the proposed endovascular Fontan repair, we could not validate our findings with post-intervention clinical data. This was due to the fact that the clinical team decided against pursuing the proposed endovascular revision, driven by the results of our analysis and by feasibility issues. Fourth, since the discussed work is an analysis

conducted on a single patient, it is difficult to translate these findings to other patients. Finally, this study does not account for hemodynamic adaptations in the system (baroreflex effects, metabolic adaptations) or long-term growth and remodeling, although such CFD applications are currently being developed.

Chapter 6 Conclusion

In this thesis, we leveraged computational modeling to improve our understanding of pediatric CVD and its treatment. Specifically, we tackled problems related to three pediatric CVDs – pulmonary arterial hypertension, renovascular hypertension caused by an abdominal aortic coarctation, and hypoplastic left heart syndrome – which were separated into individual chapters in this thesis (Chapters 3, 4, and 5, respectively). Conclusions and future steps for each chapter are detailed in the subsections below.

6.1 Pulmonary arterial hypertension (Chapter 3)

6.1.1 Summary of contributions and conclusions

Computational models, based on clinical data, were used to study hemodynamics and biomechanics in a cohort of pediatric PAH patients. Ventricular-arterial coupling is recognized as a critical contributor to PAH pathophysiology [12], but it is under-researched due to the difficulty and risk associated with measuring functional metrics related to ventricular contractility in the clinic. To overcome this, computational models were used to virtually estimate ventricular contractility and derive functional metrics that describe ventricular-arterial coupling, such as the ratio between ventricular and arterial elastances (i.e., $ESPVR/Ea$). Two different multi-scale, closed-loop models were used: (A) a high-resolution arterial model, implemented using the open-source software CRIMSON [85], and (B) a high-resolution ventricular model, implemented using the open-source software FEniCS [96].

Although the role of hemodynamics in PAH pathophysiology is well understood, significant hurdles remain in patient stratification partially due to a large number of variables that can be used in determining disease severity and large patient variability, which can involve multiple comorbidities [79], [242]. Patient stratification in the clinic is currently performed by combining non-invasive and invasive functional parameters into formulas that can predict patient prognosis. While this approach has led to numerous risk assessment calculators that have improved patient mortality and morbidity, these risk assessment tools mainly consider simple hemodynamic metrics – cardiac index, arterial and atria pressures – and have been validated primarily on adult populations [53], [54], [243]. Therefore, metrics from clinical data and our computational models were used in our work to assess disease severity. Computational models leverage highly-resolved patient-specific hemodynamic data and well-established physiological and physical principles to output comprehensive metrics used in the disease severity assessment.

Our disease severity assessment revealed that several computational and clinical metrics, based on pediatric data, significantly correlate with disease severity. Out of the evaluated metrics, 5 model-derived metrics were significantly correlated with disease severity. Of note, LV contractility was the only metric with a negative, significant correlation, suggesting that LV contractility decreases with progressive PAH. Furthermore, ventricular-arterial coupling ratio (E_{es}/E_a) was not significantly correlated with disease severity, suggesting that ventricular-arterial coupling was maintained in this patient cohort. These significantly-correlated model-derived hemodynamic metrics can help improve patient stratification in this population.

6.1.2 Future directions

Future steps will involve validating the clinical and computational metrics that were significantly correlated with disease severity. The project detailed in Chapter 3 is part of an

ongoing prospective clinical trial to acquire hemodynamic data in two patient cohorts – PAH patients and control subjects. Therefore, the significantly correlated clinical and computational metrics identified in Chapter 3 will be used to compare the two cohorts and evaluate whether significant differences exist between these cohorts. This would confirm the value that these identified metrics, particularly the non-invasive metrics, could add to the diagnosis of PAH patients.

As part of the ongoing clinical trial, longitudinal hemodynamic data will be acquired twice in each recruited patient and separated by about two years. This will allow us to track the patient’s prognosis and hemodynamic progression. Computational models will be calibrated to match clinically-acquired data from each patient at both timepoints. The progression of clinical and computational metrics will be compared to patients’ prognoses, allowing us to validate whether these metrics can help predict prognosis in this patient population.

High-resolution arterial and ventricular models were not coupled bidirectionally; therefore, parameter calibration in one model does not affect results in the other. The work presented in Chapter 3 serves as the first step towards the ultimate goal of studying ventricular-vascular coupling in PAH using high-resolution 3D ventricular and arterial models. To achieve this goal, 3D ventricular and arterial models should be strongly coupled where information is continually exchanged to ensure that changes in one model affect hemodynamics in the other, and vice-versa, as it transpires in a PAH patient.

Overall, the computational models used in this work can be used in the future to minimize the number of catheterizations performed in this population for diagnosis of PAH. Information from studies that relate imaging markers with pulmonary arterial pressures [167]–[170] can be incorporated in our models to achieve this goal.

6.2 Renovascular hypertension caused by an abdominal aortic coarctation (Chapter 4)

6.2.1 Summary of contributions and conclusions

In Chapter 4, we conducted a retrospective analysis of a 9-year-old patient with persistent renovascular hypertension after a successful repair of an abdominal aortic coarctation. The model was validated by matching computed and clinically-measured data on flow and pressure. After validation, our model revealed the presence of high-frequency hemodynamic disturbances that originated in the AAC and propagated into the renal arteries. The validated preoperative model was then modified to represent six surgical interventions commonly performed to restore renal hemodynamics. Although surgical correction of the AAC restored renal hemodynamics, high-frequency hemodynamic disturbances remained in the abdominal aorta and renal arteries in most postoperative models.

Our understanding of the RAAS fails to explain the persistence of renovascular hypertension after renal perfusion pressure and renal flow are restored, as is the case in most patients with surgically-repaired AACs. Therefore, we hypothesize that high-frequency disturbances in renal hemodynamics following AAC repair contribute to initiating the RAAS, even in the presence of adequate mean levels of renal perfusion pressures, leading to renovascular hypertension. If high-frequency renal hemodynamic disturbances are proven to trigger the RAAS, our proposed project (see future directions) could motivate a reevaluation and redesign of commonly used surgical interventions and endovascular grafts in the treatment of AAC and renovascular hypertension. Theoretically, a compliant material could be bonded to the inner surface of an thoracoabdominal bypass endovascular graft to dampen the high-frequency hemodynamic disturbances.

6.2.2 Future directions

Our next steps are to test our hypothesis by performing a longitudinal, prospective study that combines an experimental canine AAC model, subject-specific hemodynamic data, and computational modeling. We secured institutional funding to carry out this project. To confirm whether an experimental canine model could reproduce the high-frequency renal hemodynamic disturbances observed in Chapter 4, we constructed a population-based canine computational model. A baseline computational model of an aorta of a 20-30 kg dog was built and validated using population-based data on diameters [244], blood flow [245], pressure [246], and tissue properties [247] (**Figure 6.1**). The baseline model was then modified by introducing (A) an AAC and (B) an AAC and TAB repair. Renal hemodynamic disturbances were observed in the isolated AAC and TAB repair models. Therefore, these results confirm that the proposed canine model will be an adequate surrogate of AAC-related hemodynamics in pediatric patients.

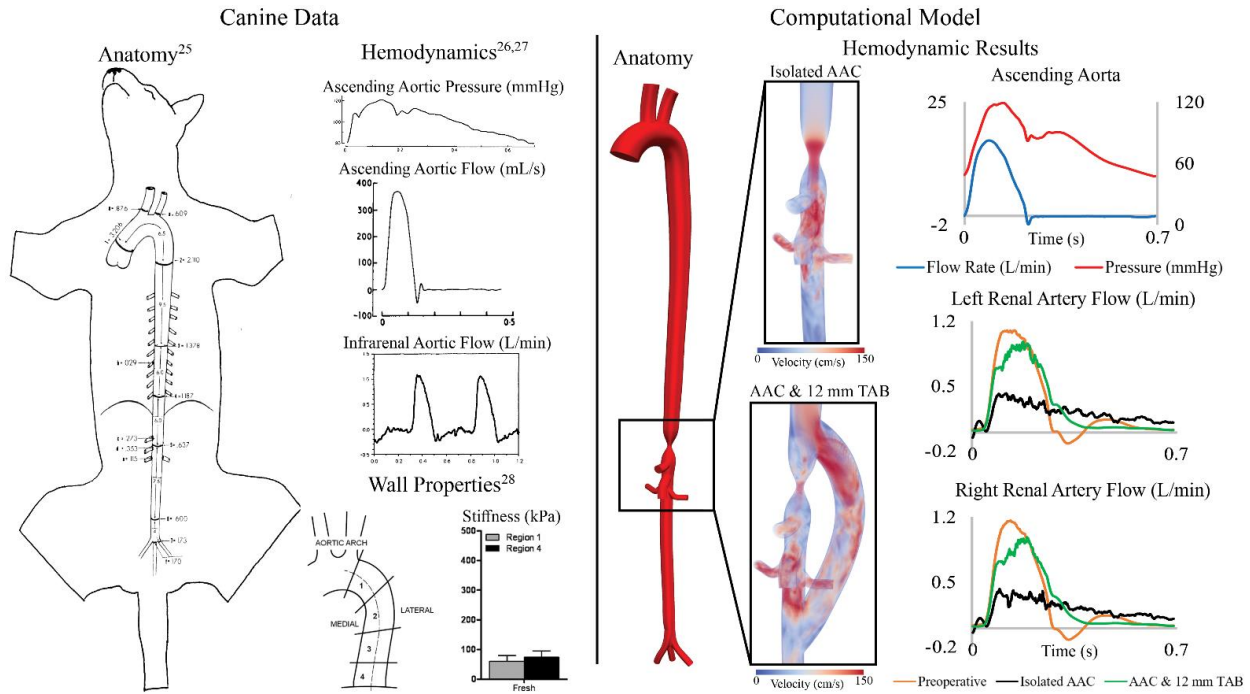


Figure 6.1 Left: Canine data for anatomy, hemodynamics, and arterial wall properties. Right: Results corresponding to a 60% diameter reduction AAC model and 12 mm TAB repair. Highly disturbed flow is seen in the isolated AAC and TAB repair models.

The experimental portion of this future project will involve acquiring longitudinal data on aortorenal hemodynamics and renin production in a canine model of AAC. Experimental data will be obtained four times throughout the study period: in Weeks 1, 3, 5, and 7 (**Figure 6.2**). Banding and TAB repairs will occur in Weeks 1 and 3, respectively. This experimental setup will enable us to measure hemodynamics and renin levels at baseline (Week 1), after AAC (Week 3), and after restoring mean levels of renal perfusion pressure while high-frequency renal hemodynamic disturbances persist (Weeks 5 and 7).

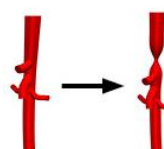
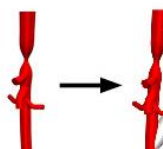


Actual Time	1 week	3 weeks	5 weeks	7 weeks
Relative Time	1 week	2 weeks p/ coarctation	4 weeks p/ coarctation 2 weeks p/ TAB graft	6 weeks p/ coarctation 4 weeks p/ TAB graft
Goal	Study Intact Control & Create Coarctation 	Study Coarctation Effect & Create TAB 	Study Coarctation & TAB Follow-up #1 	Study coarctation & TAB Follow-up #2 
Actions	Anesthesia #1 MRI @BioEngineering facility then Renin assays Arterial catheterization then Create coarctation @Jobst research lab	Anesthesia #2 MRI @BioEngineering facility then Renin assays Arterial catheterization then Create TAB @Jobst research lab	Anesthesia #3 MRI @BioEngineering facility then Renin assays Arterial catheterization @Jobst research lab	Anesthesia #4 MRI @BioEngineering facility then Renin assays Arterial catheterization @Jobst research lab

Figure 6.2 Timeline for the experimental portion of the study. Data acquisition will include anatomical and flow measurements from MRI, pressure measurements from catheterization, and renin concentration from venous assays.

After the experimental portion of the study is completed, computational models will be constructed and validated with data from each canine at each of the four timepoints. The computational results will be used to analyze and quantify high-frequency content in renal

hemodynamics. High-frequency renal hemodynamic disturbances and renin release will subsequently be assessed to understand if a relationship exists between the two, confirming our hypothesis.

6.3 Hypoplastic left heart syndrome (Chapter 5)

6.3.1 Summary of contributions and conclusions

In Chapter 5, a case study was conducted on a 2-year-old HLHS patient who had undergone the three stages of Fontan reconstruction surgery but presented with numerous complications such as elevated venous and pulmonary arterial pressures, hepatic venous reflux, and subsequent enlarged liver and protein-losing enteropathy. A pediatric cardiology team was considering an endovascular revision of the Fontan pathway to decrease the size of the inferior vena cava, relieve the hepatic venous reflux, and streamline flow to the pulmonary arteries. The clinical team collaborated with us to understand the viability and hemodynamic effects of the proposed endovascular intervention.

We created and validated a preoperative computational model using patient-specific hemodynamic data. We then virtually introduced the proposed endovascular graft to study its effects on hemodynamics around the Fontan pathway. Our computational models revealed that the proposed endovascular intervention increased venous and pulmonary arterial pressures and aggravated hepatic venous reflux while slightly improving flow delivered to the pulmonary arteries. Since the clinical team deemed these simulated results as detrimental to the patient, they decided to forgo the proposed intervention and continue to manage the patient with drug therapy. This study highlights the impact that computational modeling can have on surgical planning. If the clinical team had gone with the traditional surgical planning paradigm, which does not include

computational modeling, they would have likely performed a surgery that aggravated the patient's already poor condition.

6.3.2 Future directions

Computational modeling has the potential to make critical advancements in surgical planning, but numerous aspects are limiting its widespread clinical use. For example, surgical planning via computational modeling is a time-consuming endeavor. The analysis performed in Chapter 5 was completed over several months, requiring extensive efforts to iteratively calibrate model parameters until simulated results match clinical data. This limits the use of computational modeling for elective surgeries without time constraints. Therefore, future directions should focus on developing semi-automated, user-friendly workflows to accelerate model construction and validation and provide hemodynamic assessments [248], [249], amplifying the footprint of computational modeling in the surgical planning field.

6.4 General conclusions

The computational models used in this work were leveraged to tackle issues associated with three pediatric CVDs. Furthermore, these models were used to study hemodynamic mechanisms contributing to CVD (renal hemodynamic disturbances and ventricular-arterial coupling), aid in patient stratification, and aid in surgical planning. The findings of this work motivate exciting future studies that can increase the impact of computational modeling in the study of CVD.

Appendices

Appendix A Supplementary Strategies to Mitigate Data Inconsistencies

In Appendix A, we will be discussing additional strategies for mitigation of inconsistencies in clinical data.

A.1 Heart rate

The average heart rate derived from catheterization (71.0 ± 7.6 bpm) was 7% lower than that of PC-MRI (76.6 ± 7.7 bpm). This inconsistency can be attributed to a higher level of sedation during catheterization than MRI [250]. PC-MRI heart rate was deemed more representative of baseline physiologic conditions. Therefore, heart rates from the 5 PC-MRI anatomical locations were averaged and used to determine the cardiac cycle lengths for the high-resolution arterial and ventricular simulations.

A.2 Cardiac Output

Systemic and pulmonary cardiac outputs measured at the level of the AAO and MPA differed by 5% (4.12 ± 0.98 L/min and 3.94 ± 1.06 L/min, respectively), which are within reported thresholds [251]. Representative cardiac outputs were obtained for each patient by averaging the systemic and pulmonary measurements. PC-MRI flow waveforms were then scaled accordingly. In Subjects #3, #6, and #7, pulmonary cardiac outputs measured at the MPA were underestimated due to dilation of the MPA causing flow swirling. These underestimated pulmonary cardiac outputs were excluded from the calculations. Averaged cardiac outputs were used to inform the arterial hemodynamic simulations.

A.3 Inferring left ventricular pressure

Since LV pressure data were not measured in most patients, femoral artery and RV pressure waveforms were combined to infer LV pressure. The shape of the LV pressure waveform was assumed to be identical to that of the RV for each patient. To account for the pulse pressure amplification down the aorta, LV systolic pressure was scaled to be 88% of the measured femoral artery systolic pressure [252], whereas the LV diastolic pressure was scaled to match the measured pulmonary capillary wedge pressure. The inferred LV pressure waveforms were then used to generate pressure-volume (PV) loop data in both arterial and ventricular models.

A.4 Reference diastolic geometry for arterial models

The luminal areas obtained with the diastole-gated 3D SSFP MRI data differed from the 2D PC-MRI diastolic areas at the same location. To ensure consistency between areas when creating the geometric models of the aorta and pulmonary arteries (Section 3.4.1), the 3D SSFP areas were scaled to match the 2D PC-MRI diastolic areas [136].

Table A 1 Truncated ventricular volumes (mL) and ejection fractions (%).

	Subject #1	Subject #2	Subject #3	Subject #4	Subject #5	Subject #6	Subject #7	Subject #8
LV End-Diastolic Volume	86.9	97.6	63.1	56.5	69.5	107.5	125.4	61.6
LV End-Systolic Volume	43.7	40.3	32.5	31.7	30.9	58.7	54.1	31.8
LV Stroke Volume	43.2	57.3	30.6	24.8	38.7	48.8	71.3	29.7
LV Ejection Fraction	50%	59%	48%	44%	56%	45%	57%	48%
RV End-Diastolic Volume	98.4	115.3	65.0	60.4	77.9	98.7	206.9	68.9
RV End-Systolic Volume	57.4	61.9	37.8	38.4	40.7	52.2	137.4	42.5
RV Stroke Volume	41.0	53.4	27.3	22.1	37.3	46.5	69.5	26.4
RV Ejection Fraction	42%	46%	42%	37%	48%	47%	34%	38%

Table A 2 Patient-specific arterial wall stiffness ($g/(mm*s^2)$) calculated from PC-MRI and catheterization data.

	Subject #1	Subject #2	Subject #3	Subject #4	Subject #5	Subject #6	Subject #7	Subject #8
AAo	127,574	180,633	154,465	138,415	167,320	130,646	152,662	122,186
DTA	169,414	308,193	238,162	157,593	303,267	197,317	305,197	139,850
MPA	134,684	100,562	78,534	324,986	148,831	203,111	578,998	83,227
LPA	72,714	95,205	87,093	119,442	163,005	62,534	663,449	40,599
RPA	134,106	74,463	60,022	136,412	85,163	122,672	394,979	35,551

Table A 3 Patient-specific elastance waveform parameter values.

	Subject #1	Subject #2	Subject #3	Subject #4	Subject #5	Subject #6	Subject #7	Subject #8
LV Emax (Pa/(mm ³))	0.236	0.334	0.451	0.637	0.336	0.177	0.168	0.370
LV Emin (Pa/(mm ³))	0.015	0.015	0.010	0.030	0.019	0.009	0.009	0.022
LV m_1	1.8	2.0	2.2	2.2	1.5	1.5	1.9	2.2
LV τ_1	0.31	0.36	0.38	0.40	0.32	0.33	0.39	0.37
LV m_2	18.0	24.0	16.0	24.0	24.0	24.0	20.0	22.0
LV τ_2	0.35	0.41	0.42	0.44	0.35	0.37	0.43	0.41
RV Emax (Pa/(mm ³))	0.146	0.102	0.174	0.504	0.168	0.130	0.082	0.148
RV Emin (Pa/(mm ³))	0.010	0.001	0.005	0.036	0.015	0.010	0.005	0.005
RV m_1	1.6	2.0	1.7	2.3	1.6	2.0	1.7	2.1
RV τ_1	0.28	0.38	0.38	0.44	0.35	0.35	0.37	0.39
RV m_2	20.0	24.0	14.0	22.0	20.0	24.0	16.0	24.0
RV τ_2	0.35	0.43	0.42	0.49	0.39	0.39	0.41	0.43

Table A 4 Calibrated parameter values of patient-specific closed-loop ventricular models.

Ventricular Model Parameters	Subj. #1	Subj. #2	Subj. #3	Subj. #4	Subj. #5	Subj. #6	Subj. #7	Subj. #8	Avg	Std Dev
C_{LV} (Pa)	20	20	20	20	20	30	20	30	23	4
C_{SEPTUM} (Pa)	20	20	20	20	20	30	20	30	23	4
C_{RV} (Pa)	15	15	15	15	15	25	15	15	16	3
$T_{0,LV}$ (kPa)	85	125	140	105	110	95	90	110	107.5	17.1
$T_{0,SEPTUM}$ (kPa)	85	125	140	105	110	95	90	110	107.5	17.1
$T_{0,RV}$ (kPa)	135	60	60	260	110	125	200	34	123.0	71.5
C_{sa} (Pa)	0.006	0.010	0.004	0.005	0.005	0.009	0.012	0.004	0.007	0.003
C_{pa} (Pa)	0.007	0.014	0.004	0.003	0.006	0.010	0.009	0.001	0.007	0.004
C_{sv} (Pa)	0.30	0.30	0.27	0.30	0.30	0.30	0.30	0.30	0.30	0.01
C_{pv} (Pa)	0.09	0.09	0.08	0.09	0.09	0.09	0.09	0.06	0.09	0.01
R_{sa} (kPa*ms/mL)	160	120	240	460	180	130	110	250	206.3	107.7
R_{pa} (kPa*ms/mL)	115	10	85	425	60	65	90	13	107.9	124.6
$V_{sa,0}$ (mL)	607	610	700	610	610	610	607	575	616	34
$V_{pa,0}$ (mL)	555	500	500	500	100	400	555	525	454	141
$V_{sv,0}$ (mL)	3680	3450	3510	3550	3300	3465	3200	3380	3442	140
$V_{pv,0}$ (mL)	550	375	405	525	100	470	325	550	413	142

Left Ventricular Passive Stiffness (C_{LV}), Septum Passive Stiffness (C_{SEPTUM}), Right Ventricular Passive Stiffness (C_{RV}), Left Ventricular Maximum Tension ($T_{0,LV}$), Septum Maximum Tension ($T_{0,SEPTUM}$), Right Ventricular Maximum Tension ($T_{0,RV}$), Systemic Arterial Compliance (C_{sa}), Pulmonary Arterial Compliance (C_{pa}), Systemic Venous Compliance (C_{sv}), Pulmonary Venous Compliance (C_{pv}), Systemic Arterial Resistance (R_{sa}), Pulmonary Arterial Resistance (R_{pa}), Systemic Arterial Resting Volume ($V_{sa,0}$), Pulmonary Arterial Resting Volume ($V_{pa,0}$), Systemic Venous Resting Volume ($V_{sv,0}$), Pulmonary Venous Resting Volume ($V_{pv,0}$)

Table A 5 The disease severity stratification analysis used the aggregate of patient demographics, data-derived metrics (MRI- and cath-derived), and model-derived metrics.

Patient Demographics	Subj. #1	Subj. #2	Subj. #3	Subj. #4	Subj. #5	Subj. #6	Subj. #7	Subj. #8	Avg	Std Dev
Age (years)	11	15	10	5	16	11	19	6	11.6	4.8
BSA (m ²)	1.23	1.66	0.95	0.74	1.44	1.25	1.61	0.88	1.2	0.3
Height (cm)	154	175	123	106.7	152	152	165	121.9	143.7	23.8
Weight (kg)	33.2	56.3	26.9	18.7	49.8	35.2	56.2	23	37.4	14.9
MRI-derived metrics	Subj. #1	Subj. #2	Subj. #3	Subj. #4	Subj. #5	Subj. #6	Subj. #7	Subj. #8	Avg	Std Dev
Cardiac Index (L/min/m ²)	3.7	2.8	3.7	3.2	3.7	3.3	2.9	3.5	3.3	0.4
% of flow to LPA	45%	37%	51%	40%	47%	51%	41%	49%	0.5	0.1
Heart Rate (bpm)	91	77	79	66	83	74	70	73	76.6	7.7
RV End-Diastolic Volume Index (mL/m ²)	98	85	88	105	79	98	150	102	100.7	21.7
RV End-Systolic Volume Index (mL/m ²)	49	40	35	53	31	48	90	44	48.7	18.3
RV Stroke Volume Index (mL/m ²)	49	45	54	53	49	50	60	58	52.1	5.0
RV Ejection Fraction (%)	50	52	61	49	62	51	40	57	52.8	7.2
RV Mass Index (g/m ²)	24	22	24	22	24	17	45	14	24.0	9.2
LV End-Diastolic Volume Index (mL/m ²)	84	75	86	92	78	111	101	82	88.6	12.3
LV End-Systolic Volume Index (mL/m ²)	33	33	32	41	28	48	45	34	36.7	6.9
LV Stroke Volume Index (mL/m ²)	50	42	54	50	49	63	57	48	51.6	6.4
LV Ejection Fraction (%)	60	55	63	55	63	57	56	58	58.4	3.3
LV Mass Index (g/m ²)	45	43	45	42	41	42	57	35	43.9	6.2
MPA Diastolic Area (mm ²)	586.9	477.2	308.4	493.2	281.8	529.2	879.1	382.4	492.3	176.9
MPA Relative Area Change	35%	29%	75%	31%	38%	20%	12%	43%	35%	18%
Cath-derived metrics	Subj. #1	Subj. #2	Subj. #3	Subj. #4	Subj. #5	Subj. #6	Subj. #7	Subj. #8	Avg	Std Dev
Pulmonary arterial mean pressure (mmHg)	59.4	29.2	35.1	82.9	47.1	31.2	58.3	20.4	45.4	20.6
Pulmonary arterial systolic pressure (mmHg)	74.7	38.2	52.9	116.0	65.5	44.5	82.3	32.5	63.3	27.6
Pulmonary arterial diastolic pressure (mmHg)	44.1	20.2	17.4	49.8	28.6	17.9	34.4	8.3	27.6	13.4
Pulmonary arterial pulse pressure (mmHg)	30.6	18.0	35.4	66.2	36.9	26.6	48.0	24.1	35.7	15.3
Systemic arterial mean pressure (mmHg)	68.1	65.1	66.2	97.2	77.6	56.9	65.0	63.5	69.9	11.6
Systemic arterial systolic pressure (mmHg)	94.0	87.0	91.0	124.9	114.3	71.1	89.1	89.8	95.1	15.7
Systemic arterial diastolic pressure (mmHg)	53.6	52.3	49.6	75.0	56.6	46.6	52.9	47.2	54.2	8.4
Systemic arterial pulse pressure (mmHg)	40.4	34.7	41.4	49.9	57.6	24.5	36.2	42.5	40.9	9.3
PVR Index (WU m ²)	16.2	7.3	5.9	23.2	9.9	4.9	16.0	3.3	10.8	6.9
Rp:Rs	0.8	0.4	0.32	0.77	0.55	0.33	0.8	0.2	0.5	0.2
Pulmonary Capillary Wedge Pressure (mmHg)	10	8	15	14	12	14	12	8	11.5	2.7
Pulmonary Arterial Oxygen Saturation (%)	80%	72%	64%	60%	73%	64%	70%	73%	70%	6%

Heart Rate (bpm)	69	65	78	66	72	65	66	86	71.0	7.6
RV Systolic Pressure/LV Systolic Pressure (%)	79%	44%	58%	93%	57%	63%	92%	36%	65%	20%
RV Stroke Work (mmHg mL)	2227	2002	2015	3277	1727	2561	4758	1166	2467	979
RV Stroke Work/LV Stroke Work (%)	88%	51%	48%	98%	72%	61%	95%	42%	69%	21%
Pulmonary Arterial Compliance Index (mL/mmHg/m ²)	0.63	0.40	0.66	1.26	0.75	0.53	0.80	0.42	0.68	0.26
Arterial model-derived metrics	Subj. #1	Subj. #2	Subj. #3	Subj. #4	Subj. #5	Subj. #6	Subj. #7	Subj. #8	Avg	Std Dev
LV Max Elastance (Pa/(mm ³))	0.236	0.334	0.451	0.637	0.336	0.177	0.168	0.370	0.339	0.145
RV Max Elastance (Pa/(mm ³))	0.146	0.102	0.174	0.504	0.168	0.130	0.082	0.148	0.182	0.125
AAo Stiffness (kPa)	127.6	180.6	154.5	138.4	167.3	130.6	152.7	122.2	146.7	19.3
DTA Stiffness (kPa)	169.4	308.2	238.2	157.6	303.3	197.3	305.2	139.9	227.4	66.4
MPA Stiffness (kPa)	134.7	100.6	78.5	325.0	148.8	203.1	579.0	83.2	206.6	159.7
LPA Stiffness (kPa)	72.7	95.2	87.1	119.4	163.0	62.5	663.4	40.6	163.0	192.3
RPA Stiffness (kPa)	134.1	74.5	60.0	136.4	85.2	122.7	395.0	35.6	130.4	105.6
AAo-DTA Pulse Wave Velocity (m/s)	2.79	5.36	3.61	4.39	5.10	2.98	4.14	3.00	3.92	0.92
MPA-LPA Pulse Wave Velocity (m/s)	3.51	3.14	2.19	6.30	2.93	1.88	5.58	2.31	3.48	1.52
MPA-RPA Pulse Wave Velocity (m/s)	4.05	2.64	2.06	3.82	2.64	1.86	4.57	2.04	2.96	0.97
Total Pulmonary Arterial Resistance (Pa*s/mm ³)	0.11	0.05	0.07	0.28	0.08	0.06	0.11	0.05	0.10	0.07
Central Pulmonary Arterial Resistance (Pa*s/mm ³ *10 ⁻³)	4.4	0.6	3.5	2	2.8	13.2	5.7	6.9	4.9	3.6
Total Pulmonary Arterial Compliance (mm ³ /Pa)	11.16	20.49	5.98	3.45	10.17	17.41	7.46	21.90	12.25	6.45
Central Pulmonary Arterial Compliance (mm ³ /Pa)	6.66	17.81	4.19	1.88	4.34	5.62	5.25	16.67	7.80	5.61
Ventricular model-derived metrics	Subject #1	Subject #2	Subject #3	Subject #4	Subject #5	Subject #6	Subject #7	Subject #8	Average	Std Dev
LV Passive Stiffness (Pa)	20	20	20	20	20	30	20	30	23	4
RV Passive Stiffness (Pa)	15	15	15	15	15	25	15	15	16	3
LV Active Contractility (T _{ref, LV}) (kPa)	85	125	140	105	110	95	90	110	107.5	17.1
RV Active Contractility (T _{ref, RV}) (kPa)	135	60	60	260	110	125	200	34	123	71.5
RV ESPVR (mmHg/mL)	1.32	0.64	1.22	3.19	1.63	1.22	0.70	0.63	1.32	0.78
RV Ea (mmHg/mL)	1.96	0.73	1.69	4.86	1.80	1.03	1.32	1.33	1.84	1.20
RV ESPVR/Ea	0.67	0.89	0.72	0.66	0.91	1.18	0.54	0.47	0.75	0.21

Table A 6 Normalized sensitivity values of measured hemodynamic metrics to parameter changes of 10% in the high-resolution arterial model of Subject #6. Normalized sensitivity value represents a ratio of change in error relative to a parameter value change.

Parameters	Computed Hemodynamic Metrics									
	Pulmonary Arterial Flow Rate	Pulmonary Arterial Systolic Pressure	Pulmonary Arterial Diastolic Pressure	Pulmonary Arterial Pulse Pressure	Pulmonary Arterial Mean Pressure	Aortic Flow Rate	Aortic Systolic Pressure	Aortic Diastolic Pressure	Aortic Pulse Pressure	Aortic Mean Pressure
Total Pulmonary Arterial Resistance	-0.141	0.275	0.355	0.216	0.125	-0.120	-0.026	-0.048	0.000	-0.052
Total Pulmonary Venous Resistance	0.006	0.120	0.329	-0.037	0.228	-0.087	-0.065	-0.162	0.050	-0.099
Total Pulmonary Arterial Compliance	0.077	0.003	0.213	-0.155	0.062	-0.155	0.017	0.111	-0.096	0.012
Total Pulmonary Venous Compliance	0.103	0.066	0.050	0.079	0.061	0.013	0.029	0.093	-0.046	0.051
RV Source Resistance Coefficient (Ks)	0.027	-0.135	-0.116	-0.149	-0.103	-0.141	-0.039	0.007	-0.095	-0.035
Pulmonary Vasculature Initial Pressures	0.386	0.429	0.485	0.386	0.454	0.349	0.293	0.328	0.251	0.330
Total Systemic Arterial Resistance	-0.191	-0.102	0.028	-0.200	-0.060	-0.380	0.359	0.745	-0.102	0.469
Total Systemic Venous Resistance	0.035	-0.036	0.017	-0.076	-0.002	-0.008	0.064	0.114	0.004	0.100
Total Systemic Arterial Compliance	0.104	0.028	0.022	0.033	0.038	-0.131	-0.215	0.192	-0.699	-0.048
Total Systemic Venous Compliance	0.141	0.011	-0.029	0.041	0.025	-0.110	0.005	0.092	-0.098	0.010
LV Source Resistance Coefficient (Ks)	-0.178	-0.075	0.105	-0.210	-0.012	-0.316	-0.229	-0.157	-0.314	-0.225
Systemic Vasculature Initial Pressures	0.365	0.378	0.388	0.371	0.382	0.329	0.211	0.242	0.175	0.189

Table A 7 Normalized sensitivity values of measured hemodynamic metrics to parameter changes of 10% in the high-resolution ventricular model of Subject #6. Normalized sensitivity value represents a ratio of change in error relative to a parameter value change.

Parameters	Computed Hemodynamic Metrics									
	RV End-Diastolic Volume	RV End-Systolic Volume	RV Stroke Volume	RV End-Systolic Pressure	RV End-Diastolic Pressure	LV End-Diastolic Volume	LV End-Systolic Volume	LV Stroke Volume	LV End-Systolic Pressure	LV End-Diastolic Pressure
T _{0,LV} (kPa)	0.140	0.024	0.264	0.168	-0.099	-0.089	-0.387	0.273	0.284	-1.562
T _{0,SEPTUM} (kPa)	0.024	-0.003	0.053	0.034	-0.041	-0.015	-0.073	0.055	0.050	-0.263
T _{0,RV} (kPa)	-0.146	-0.383	0.109	0.138	-0.843	0.062	0.030	0.101	0.083	0.595
C _{LV} (Pa)	-0.019	-0.006	-0.034	-0.016	0.098	-0.040	-0.045	-0.035	-0.037	0.382
C _{SEPTUM} (Pa)	-0.006	-0.001	-0.012	-0.005	-0.015	-0.013	-0.013	-0.013	-0.013	0.156
C _{RV} (Pa)	-0.025	-0.025	-0.026	-0.035	0.411	-0.018	-0.015	-0.023	-0.017	-0.123
C _{sa} (Pa)	0.017	-0.005	0.039	-0.025	-0.477	-0.054	-0.135	0.045	-0.130	-1.036
C _{sv} (Pa)	-0.053	-0.062	-0.044	-0.091	-0.817	-0.029	-0.029	-0.030	-0.037	-0.733
C _{pa} (Pa)	-0.080	-0.167	0.014	-0.240	-0.723	0.011	0.013	0.009	-0.002	-0.132
C _{pv} (Pa)	-0.025	-0.037	-0.013	-0.053	-0.483	-0.020	-0.021	-0.020	-0.026	-0.593
R _{sa} (kPa*ms/mL)	-0.231	-0.179	-0.286	-0.203	-0.750	0.089	0.409	-0.300	0.393	1.599
R _{pa} (kPa*ms/mL)	0.136	0.343	-0.087	0.419	0.643	-0.086	-0.091	-0.080	-0.069	-1.008
V _{sv,0} (mL)	-0.399	-0.435	-0.360	-0.675	-2.287	-0.300	-0.284	-0.321	-0.357	-2.367
V _{pv,0} (mL)	-0.222	-0.263	-0.178	-0.404	-1.614	-0.198	-0.198	-0.199	-0.242	-1.749
V _{sa,0} (mL)	-0.328	-0.368	-0.286	-0.568	-2.045	-0.262	-0.252	-0.275	-0.313	-2.148
V _{pa,0} (mL)	-0.194	-0.229	-0.156	-0.349	-1.407	-0.161	-0.159	-0.164	-0.195	-1.504

Appendix B Abdominal Aortic Coarctation Models: Additional Information

Finite-element meshes contained 2-4 million tetrahedral elements and localized refinement was performed using an adaptive technique in regions of high velocities and complex flow.[254] The assigned stiffness parameters were derived from a study within our group that characterizes aortic stiffness in a cohort of pediatric patients with aortic coarctation.[207] In that study, the stiffness was measured using PC-MRI and invasive pressure measurements from catheterization.

The workflow consisted of initially building and validating the preoperative model. The clinically acquired measurements of preoperative cardiac output, aortic pressure and sub-renal flow were matched by tuning the parameters of Windkessel models.[193] Three-element Windkessel models were used to represent the resistance and compliance of the anatomy distal to the model's outlets.[255] The proximal resistor was set as 5% of the total resistance in all outflow branches, with the exception of the carotid, subclavian, and renal arteries where the relative value for the proximal resistor was increased to eliminate backflow. Additionally, the inlet flow waveform was reduced by 5% to account for the flow going to the enlarged lumbar arteries that are not included in the computational models.

A mesh dependence analysis was conducted to ensure that the presence of high frequency disturbances in the preoperative model was independent of mesh size. The renal artery flow waveforms from models containing 2.5 million elements and 4.9 million elements were compared (**Appendix Figure B.1**). The presence of high-frequency flow disturbances persists in the renal arteries of the model with the refined mesh (4.9 million elements). This confirms that the high-

frequency disturbances are not dependent on mesh size. The results reported in this work were obtained using the mesh containing 2.5 million elements.

To analyze time-step size dependency of the high frequency disturbances in the preoperative model, an analysis was conducted where the time-step size was decreased to one fifth of the original ($\Delta t = 5e-6$ s). The high-frequency disturbances were present in the renal flow waveforms of both simulations (**Appendix Figure B.2**), confirming that the presence of these disturbances is independent of the time-step size.

To compare the diseased aortic hemodynamics to a ‘healthy’ control, the model of the preoperative anatomy was modified by removing the aortic coarctation, ostial stenoses of visceral arteries and collaterals. The model of the control healthy anatomy is presented in **Appendix Figure B.3**. The boundary conditions of the control case were tuned to match preoperative flow splits (**Appendix Table B.1**), and a normal blood pressure for the patient’s size and age (96/65 mmHg).[194] The control case showed healthy hemodynamics in the ascending aorta and renal arteries. The renal artery flow and pressure waveforms (**Appendix Figure B.3**) show systolic dominated waveforms without high-frequency disturbances.

In the virtual repair scenarios, flow distributions to the supra-aortic arteries was severely diminished due to the removal of the effective resistance created by the coarctation. An auto-parameterization scheme was applied to 5 of the 14 outlets to match proper supra-aortic flow distributions post-operatively.[256] The 5 outlets that underwent auto-parameterization were the following: right common carotid, right subclavian artery, left common carotid, left subclavian artery, and superior mesenteric artery. After auto-parameterization was performed, the simulations of all surgical interventions were run with the same outflow boundary conditions parameters (**Appendix Table B.2**).

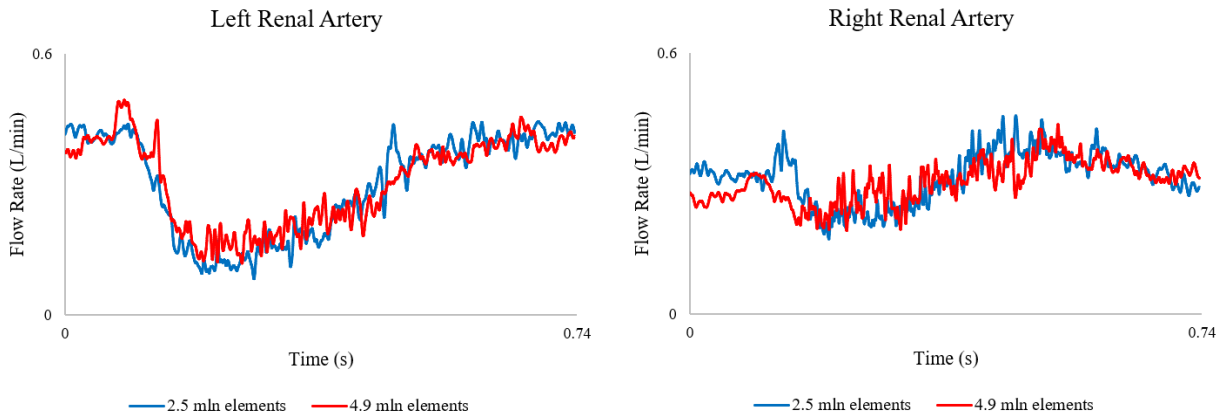


Figure B 1 Renal flow waveforms in preoperative models with mesh sizes of 2.5 million elements (blue) and 4.9 million elements (red). Local mesh refinement methods were used to increase mesh size in the region of the aortic narrowing and renal arteries.

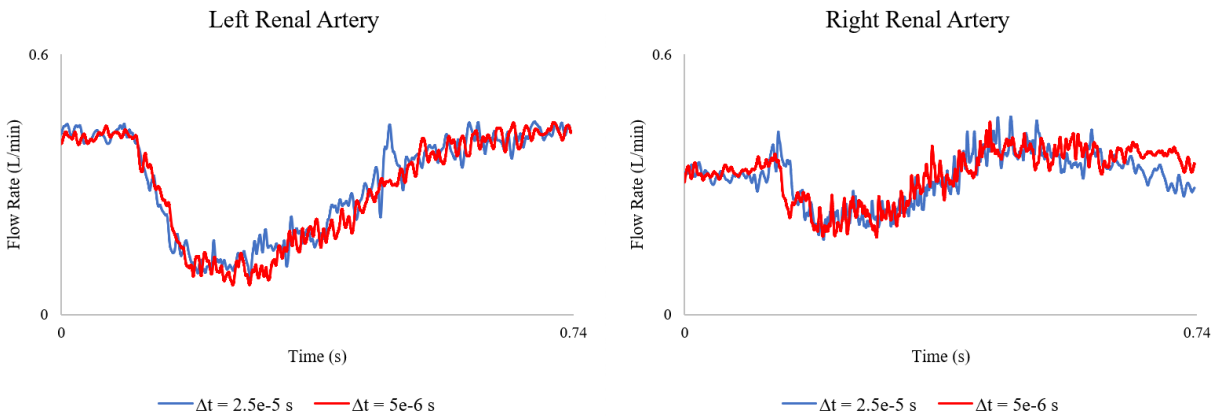


Figure B 2 Simulations of the preoperative model were run with a time step size of $2.5e-5$ s (blue) and $5e-6$ s (red). All waveforms exhibit high-frequency disturbances, confirming the presence of high-frequency disturbances in both temporal resolutions.

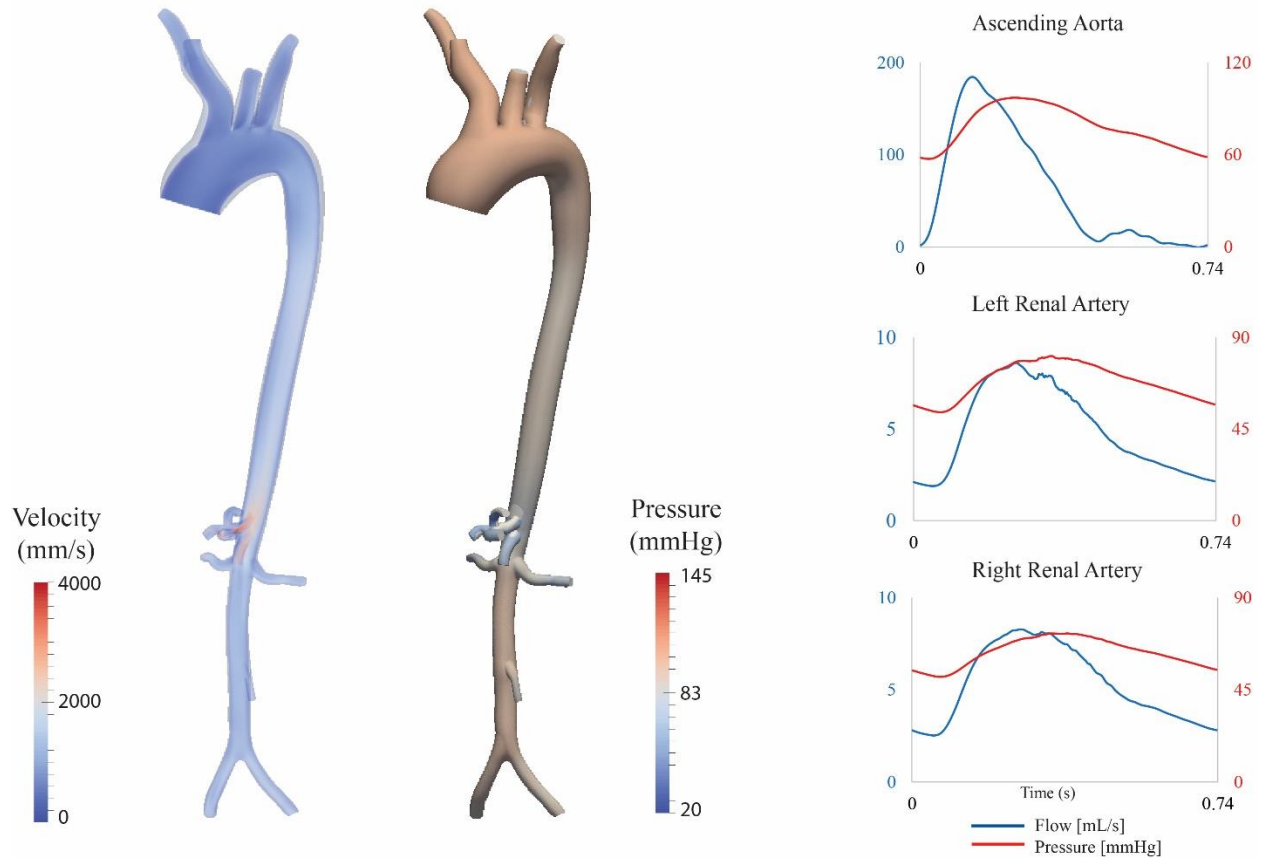


Figure B 3 Left: 3D maps of preoperative hemodynamics in peak systole. Right: flow (blue) and pressure (red) waveforms in the ascending aorta, left renal artery, and right renal artery. The renal artery waveforms reveal near normal systolic dominated flows.

Table B 1 Parameter values for the three-element Windkessel models used in the preoperative model (left) and all postoperative models (right).

Vessel	Preoperative			Postoperative		
	Rp	C	Rd	Rp	C	Rd
Left Common Carotid Artery	0.3401	6.580	1.9276	0.3401	6.580	1.0712
Left Subclavian Artery	0.3426	6.270	1.9523	0.3426	6.270	1.1043
Right Common Carotid Artery	0.3402	6.580	1.9282	0.3402	6.580	1.0693
Right Subclavian Artery	0.3353	6.270	1.9103	0.3353	6.270	1.0833
Superior Mesenteric Artery	0.0236	5.367	0.3992	0.0236	5.367	0.5731
Left Gastric Artery	0.0152	1.568	0.2586	0.0152	1.568	0.2586
Splenic Artery	0.0264	2.405	0.4457	0.0264	2.405	0.4457
Hepatic Artery 1	0.0003	1.690	0.0051	0.0003	1.690	0.0051
Hepatic Artery 2	0.0842	3.000	1.5033	0.0842	3.000	1.5033
Left Renal Artery	0.2090	3.537	0.8358	0.2090	3.537	0.8358
Right Renal Artery	0.2034	3.537	0.8136	0.2034	3.537	0.8136
Inferior Mesenteric Artery	0.2889	0.697	4.8701	0.2889	0.697	4.8701
Left Iliac Artery	0.1013	2.091	1.7557	0.1013	2.091	1.7557
Right Iliac Artery	0.0994	2.091	1.7313	0.0994	2.091	1.7313

Rp represents proximal resistor (Pa s mm^{-3}), *C* represents capacitor ($\text{mm}^3 \text{Pa}^{-1}$), and *Rd* represents distal resistor (Pa s mm^{-3})

Table B 2 Simulated mean flow rates in mL/min. Hepatic Left Artery in Preoperative model includes the addition of mean flow from both Hepatic Artery 1 and Hepatic Artery 2. Mean flows for all branches were matched within 5% error margins.

Vessel	Preoperative	Control
Left Common Carotid Artery	28	28
Left Subclavian Artery	27	27
Right Common Carotid Artery	28	28
Right Subclavian Artery	27	28
Superior Mesenteric Artery	57	56
Left Gastric Artery	29	28
Splenic Artery	30	29
Hepatic Artery	26	25
Left Renal Artery	29	30
Right Renal Artery	31	32
Inferior Mesenteric Artery	9	9
Left Iliac Artery	28	28
Right Iliac Artery	28	29

Bibliography

- [1] G. Kovacs, A. Berghold, S. Scheidl, and H. Olschewski, 'Pulmonary arterial pressure during rest and exercise in healthy subjects: a systematic review', *European Respiratory Journal*, vol. 34, no. 4, pp. 888–894, Oct. 2009, doi: 10.1183/09031936.00145608.
- [2] R. Saggar and O. Sitbon, 'Hemodynamics in Pulmonary Arterial Hypertension: Current and Future Perspectives', *Am J Cardiol*, vol. 110, no. 6, pp. S9–S15, Sep. 2012, doi: 10.1016/J.AMJCARD.2012.06.011.
- [3] E. D. Frohlich, M. Ulrych, R. C. Tarazi, H. P. Dustan, and I. H. Page, 'A Hemodynamic Comparison of Essential and Renovascular Hypertension', *Circulation*, vol. 35, no. 2, pp. 289–297, 1967, doi: 10.1161/01.CIR.35.2.289.
- [4] H. Enes Salman *et al.*, 'Hemodynamic and Structural Comparison of Human Fetal Heart Development Between Normally Growing and Hypoplastic Left Heart Syndrome-Diagnosed Hearts', *Front Physiol*, vol. 13, Mar. 2022, doi: 10.3389/FPHYS.2022.856879.
- [5] P. Martinez-Quinones *et al.*, 'Hypertension Induced Morphological and Physiological Changes in Cells of the Arterial Wall', *Am J Hypertens*, vol. 31, no. 10, pp. 1067–1078, Sep. 2018, doi: 10.1093/AJH/HPY083.
- [6] R. M. Touyz *et al.*, 'Vascular smooth muscle contraction in hypertension', *Cardiovasc Res*, vol. 114, no. 4, p. 529, Mar. 2018, doi: 10.1093/CVR/ CVY023.
- [7] X. Jin *et al.*, 'New Molecular Mechanisms for Cardiovascular Disease: Contribution of Endothelium-Derived Hyperpolarizing Factor in the Regulation of Vasoconstriction in Peripheral Resistance Arteries', *J Pharmacol Sci*, vol. 116, no. 4, pp. 332–336, Jan. 2011, doi: 10.1254/JPHS.10R30FM.
- [8] M. Kim, M. J. Roman, M. C. Cavallini, J. E. Schwartz, T. G. Pickering, and R. B. Devereux, 'Effect of hypertension on aortic root size and prevalence of aortic regurgitation', *Hypertension*, vol. 28, no. 1, pp. 47–52, 1996, doi: 10.1161/01.HYP.28.1.47/FORMAT/EPUB.
- [9] T. E. Raymond, J. E. Khabbaza, R. Yadav, and A. R. Tonelli, 'Significance of main pulmonary artery dilation on imaging studies', *Ann Am Thorac Soc*, vol. 11, no. 10, pp. 1623–1632, Dec. 2014, doi: 10.1513/ANNALSATS.201406-253PP/SUPPL_FILE/DISCLOSURES.PDF.
- [10] R. Naeije and A. Manes, 'The right ventricle in pulmonary arterial hypertension', *European Respiratory Review*, vol. 23, no. 134, pp. 476–487, Dec. 2014, doi: 10.1183/09059180.00007414.
- [11] M. Yildiz, A. A. Oktay, M. H. Stewart, R. v. Milani, H. O. Ventura, and C. J. Lavie, 'Left ventricular hypertrophy and hypertension', *Prog Cardiovasc Dis*, vol. 63, no. 1, pp. 10–21, Jan. 2020, doi: 10.1016/J.PCAD.2019.11.009.

- [12] A. Vonk Noordegraaf, B. E. Westerhof, and N. Westerhof, ‘The Relationship Between the Right Ventricle and its Load in Pulmonary Hypertension’, *J Am Coll Cardiol*, vol. 69, no. 2, pp. 236–243, 2017, doi: 10.1016/j.jacc.2016.10.047.
- [13] J. Corral-Acero *et al.*, ‘The “Digital Twin” to enable the vision of precision cardiology’, *Eur Heart J*, vol. 41, no. 48, pp. 4556–4564, Dec. 2020, doi: 10.1093/EURHEARTJ/EHAA159.
- [14] D. A. Nordsletten, S. A. Niederer, M. P. Nash, P. J. Hunter, and N. P. Smith, ‘Coupling multi-physics models to cardiac mechanics’, *Prog Biophys Mol Biol*, vol. 104, no. 1–3, pp. 77–88, Jan. 2011, doi: 10.1016/J.PBIOMOLBIO.2009.11.001.
- [15] C. A. Taylor and C. A. Figueroa, ‘Patient-specific modeling of cardiovascular mechanics.’, *Annu Rev Biomed Eng*, vol. 11, pp. 109–134, 2009, doi: 10.1146/annurev.bioeng.10.061807.160521.
- [16] K. L. McNiece, T. S. Poffenbarger, J. L. Turner, K. D. Franco, J. M. Sorof, and R. J. Portman, ‘Prevalence of Hypertension and Pre-Hypertension among Adolescents’, *J Pediatr*, vol. 150, no. 6, pp. 640–644.e1, Jun. 2007, doi: 10.1016/J.JPEDI.2007.01.052.
- [17] M. P. Heron, ‘Deaths : leading causes for 2018’, vol. 70, May 2021, doi: 10.15620/CDC:104186.
- [18] L. Mahony *et al.*, ‘The Pediatric Heart Network: A primer for the conduct of multicenter studies in children with congenital and acquired heart disease’, *Pediatr Cardiol*, vol. 27, no. 2, pp. 191–198, Apr. 2006, doi: 10.1007/S00246-005-1151-9/TABLES/2.
- [19] S. K. Pasquali *et al.*, ‘Off-label use of cardiovascular medications in children hospitalized with congenital and acquired heart disease’, *Circ Cardiovasc Qual Outcomes*, vol. 1, no. 2, pp. 74–83, Nov. 2008, doi: 10.1161/CIRCOUTCOMES.108.787176.
- [20] C. Lenfant, ‘Report of the Task Force on Research in Pediatric Cardiovascular Disease’, *Circulation*, vol. 106, no. 9, pp. 1037–1042, Aug. 2002.
- [21] T. Karamlou, B. S. Diggs, R. M. Ungerleider, and K. F. Welke, ‘Evolution of treatment options and outcomes for hypoplastic left heart syndrome over an 18-year period’, *J Thorac Cardiovasc Surg*, vol. 139, no. 1, pp. 119–127, Jan. 2010, doi: 10.1016/J.JTCVS.2009.04.061.
- [22] B. T. Tang *et al.*, ‘Abdominal aortic hemodynamics in young healthy adults at rest and during lower limb exercise: Quantification using image-based computer modeling’, *Am J Physiol Heart Circ Physiol*, vol. 291, no. 2, pp. 668–676, 2006, doi: 10.1152/AJPHEART.01301.2005/ASSET/IMAGES/LARGE/ZH40080667760007.JPEG.
- [23] B. T. Tang, T. A. Fonte, F. P. Chan, P. S. Tsao, J. A. Feinstein, and C. A. Taylor, ‘Three-dimensional hemodynamics in the human pulmonary arteries under resting and exercise conditions’, *Ann Biomed Eng*, vol. 39, no. 1, pp. 347–358, Jan. 2011, doi: 10.1007/S10439-010-0124-1/FIGURES/7.
- [24] S. A. Niederer, J. Lumens, and N. A. Trayanova, ‘Computational models in cardiology’, *Nature Reviews Cardiology* 2018 16:2, vol. 16, no. 2, pp. 100–111, Oct. 2018, doi: 10.1038/s41569-018-0104-y.

- [25] T. Y. Hsia, T. Conover, and R. Figliola, ‘Computational Modeling to Support Surgical Decision Making in Single Ventricle Physiology’, *Semin Thorac Cardiovasc Surg Pediatr Card Surg Annu*, vol. 23, pp. 2–10, Jan. 2020, doi: 10.1053/J.PCSU.2020.01.001.
- [26] F. Cuomo, S. Roccabianca, Desmond. Dillon-Murphy, N. Xiao, J. D. Humphrey, and C. Alberto. Figueroa, ‘Effects of age-associated regional changes in human central artery mechanics on systemic hemodynamics revealed by computational modeling’, *PLoS One*, vol. 12, no. 3, pp. 1–21, 2017, doi: 10.7302/Z24B2Z7Z.
- [27] S. Laurent *et al.*, ‘Aortic Stiffness Is an Independent Predictor of All-Cause and Cardiovascular Mortality in Hypertensive Patients’, *Hypertension*, vol. 37, no. 5, pp. 1236–1241, 2001, doi: 10.1161/01.HYP.37.5.1236.
- [28] V. M. Barodka, B. L. Joshi, D. E. Berkowitz, C. W. Hogue, and D. Nyhan, ‘Implications of vascular aging’, *Anesth Analg*, vol. 112, no. 5, pp. 1048–1060, 2011, doi: 10.1213/ANE.0B013E3182147E3C.
- [29] F. U. S. Mattace-Raso *et al.*, ‘Determinants of pulse wave velocity in healthy people and in the presence of cardiovascular risk factors: “establishing normal and reference values”’, *Eur Heart J*, vol. 31, no. 19, pp. 2338–2350, Oct. 2010, doi: 10.1093/EURHEARTJ/EHQ165.
- [30] W. Yang, M. Dong, M. Rabinovitch, F. P. Chan, A. L. Marsden, and J. A. Feinstein, ‘Evolution of hemodynamic forces in the pulmonary tree with progressively worsening pulmonary arterial hypertension in pediatric patients’, *Biomech Model Mechanobiol*, vol. 18, no. 3, pp. 779–796, 2019, doi: 10.1007/s10237-018-01114-0.
- [31] M. U. Qureshi *et al.*, ‘Numerical simulation of blood flow and pressure drop in the pulmonary arterial and venous circulation’, *Biomech Model Mechanobiol*, vol. 13, no. 5, pp. 1137–1154, Oct. 2014, doi: 10.1007/S10237-014-0563-Y/FIGURES/8.
- [32] J. F. LaDisa, C. A. Taylor, and J. A. Feinstein, ‘Aortic coarctation: Recent developments in experimental and computational methods to assess treatments for this simple condition’, *Prog Pediatr Cardiol*, vol. 30, no. 1–2, pp. 45–49, Dec. 2010, doi: 10.1016/J.PPEDCARD.2010.09.006.
- [33] L. Goubergrits *et al.*, ‘MRI-based computational fluid dynamics for diagnosis and treatment prediction: Clinical validation study in patients with coarctation of aorta’, *Journal of Magnetic Resonance Imaging*, vol. 41, no. 4, pp. 909–916, Apr. 2015, doi: 10.1002/JMRI.24639.
- [34] H. E. Salman, R. Y. Kamal, Z. M. Hijazi, and H. C. Yalcin, ‘Hemodynamic and Structural Comparison of Human Fetal Heart Development Between Normally Growing and Hypoplastic Left Heart Syndrome-Diagnosed Hearts’, *Front Physiol*, vol. 13, Mar. 2022, doi: 10.3389/FPHYS.2022.856879.
- [35] E. L. Bove *et al.*, ‘Use of mathematic modeling to compare and predict hemodynamic effects of the modified Blalock–Taussig and right ventricle–pulmonary artery shunts for hypoplastic left heart syndrome’, *J Thorac Cardiovasc Surg*, vol. 136, no. 2, pp. 312–320.e2, Aug. 2008, doi: 10.1016/J.JTCVS.2007.04.078.

- [36] Y. Horiuchi *et al.*, ‘Identifying novel phenotypes of acute heart failure using cluster analysis of clinical variables’, *Int J Cardiol*, vol. 262, pp. 57–63, Jul. 2018, doi: 10.1016/J.IJCARD.2018.03.098.
- [37] P. D. Morris *et al.*, ‘Fast Virtual Fractional Flow Reserve Based Upon Steady-State Computational Fluid Dynamics Analysis: Results From the VIRTU-Fast Study’, *Basic to Translational Science*, vol. 2, no. 4, pp. 434–446, Aug. 2017, doi: 10.1016/J.JACBTS.2017.04.003.
- [38] C. X. Tang *et al.*, ‘CT FFR for Ischemia-Specific CAD With a New Computational Fluid Dynamics Algorithm: A Chinese Multicenter Study’, *Cardiovascular Imaging*, vol. 13, no. 4, pp. 980–990, Apr. 2020, doi: 10.1016/J.JCMG.2019.06.018.
- [39] W. F. Fearon, ‘Physiologic approach for coronary intervention’, *Korean J Intern Med*, vol. 28, no. 1, p. 1, 2013, doi: 10.3904/KJIM.2013.28.1.1.
- [40] P. D. Morris *et al.*, ‘Computational fluid dynamics modelling in cardiovascular medicine’, *Heart*, vol. 102, no. 1, pp. 18–28, Jan. 2016, doi: 10.1136/HEARTJNL-2015-308044.
- [41] S. D. S. Peter and D. J. Ostlie, ‘A review of vascular surgery in the pediatric population’, *Pediatr Surg Int*, vol. 23, no. 1, pp. 1–10, Jan. 2007, doi: 10.1007/S00383-006-1778-5/METRICS.
- [42] T. M. J. van Bakel, K. D. Lau, J. Hirsch-Romano, S. Trimarchi, A. L. Dorfman, and C. A. Figueroa, ‘Patient-specific modeling of hemodynamics: Supporting surgical planning in a fontan circulation correction’, *J Cardiovasc Transl Res*, vol. 11, no. 2, pp. 145–155, Apr. 2018, doi: 10.1007/s12265-017-9781-x.
- [43] P. M. Trusty *et al.*, ‘Fontan surgical planning: Previous accomplishments, current challenges, and future directions’, *J Cardiovasc Transl Res*, vol. 11, no. 2, pp. 133–144, Jan. 2018, doi: 10.1007/S12265-018-9786-0/FIGURES/9.
- [44] M. AL, V.-C. IE, C. FP, F. JA, and T. CA, ‘Effects of exercise and respiration on hemodynamic efficiency in CFD simulations of the total cavopulmonary connection’, *Ann Biomed Eng*, vol. 35, no. 2, pp. 250–263, Feb. 2007, doi: 10.1007/S10439-006-9224-3.
- [45] M. Esmaily-Moghadam, F. Migliavacca, I. E. Vignon-Clementel, T. Y. Hsia, and A. L. Marsden, ‘Optimization of shunt placement for the norwood surgery using multi-domain modeling’, *J Biomech Eng*, vol. 134, no. 5, May 2012, doi: 10.1115/1.4006814/475141.
- [46] P. M. Trusty *et al.*, ‘The first cohort of prospective Fontan surgical planning patients with follow-up data: How accurate is surgical planning?’, *J Thorac Cardiovasc Surg*, vol. 157, no. 3, pp. 1146–1155, Mar. 2019, doi: 10.1016/J.JTCVS.2018.11.102.
- [47] D. Cosentino *et al.*, ‘Patient-specific computational models to support interventional procedures: A case study of complex aortic re-coarctation’, *EuroIntervention*, vol. 11, no. 6, pp. 669–672, Oct. 2015, doi: 10.4244/EIJY15M09_03.
- [48] T. M. van Bakel *et al.*, ‘A computational analysis of different endograft designs for Zone 0 aortic arch repair†’, *European Journal of Cardio-Thoracic Surgery*, vol. 54, no. 2, pp. 389–396, Aug. 2018, doi: 10.1093/ejcts/ezy068.

- [49] G. Simonneau *et al.*, ‘Haemodynamic definitions and updated clinical classification of pulmonary hypertension’, *Eur Respir J*, vol. 53, no. 1, 2019, doi: 10.1183/13993003.01913-2018.
- [50] A. Vonk Noordegraaf *et al.*, ‘Pathophysiology of the right ventricle and of the pulmonary circulation in pulmonary hypertension: an update Number 3 in the series “Proceedings of the 6th World Symposium on Pulmonary Hypertension” Edited by N’, *European Respiratory Journal*, vol. 53, 2019, doi: 10.1183/13993003.01900-2018.
- [51] L. A. Shimoda and S. S. Laurie, ‘Vascular remodeling in pulmonary hypertension’, *J Mol Med*, vol. 91, no. 3, pp. 297–309, 2013, doi: 10.1007/s00109-013-0998-0.
- [52] R. L. Benza *et al.*, ‘Predicting survival in pulmonary arterial hypertension: insights from the Registry to Evaluate Early and Long-Term Pulmonary Arterial Hypertension Disease Management (REVEAL)’, *Circulation*, vol. 122, no. 2, pp. 164–172, Jul. 2010, doi: 10.1161/CIRCULATIONAHA.109.898122.
- [53] T. Thenappan, S. J. Shah, S. Rich, L. Tian, S. L. Archer, and M. Gomberg-Maitland, ‘Survival in pulmonary arterial hypertension: a reappraisal of the NIH risk stratification equation’, *Eur Respir J*, vol. 35, no. 5, pp. 1079–1087, May 2010, doi: 10.1183/09031936.00072709.
- [54] M. Humbert *et al.*, ‘Survival in patients with idiopathic, familial, and anorexigen-associated pulmonary arterial hypertension in the modern management era’, *Circulation*, vol. 122, no. 2, pp. 156–163, Jul. 2010, doi: 10.1161/CIRCULATIONAHA.109.911818.
- [55] M. A. Sparks, S. D. Crowley, S. B. Gurley, M. Mirotsoy, and T. M. Coffman, ‘Classical Renin-Angiotensin system in kidney physiology.’, *Compr Physiol*, vol. 4, no. 3, pp. 1201–28, 2014, doi: 10.1002/cphy.c130040.
- [56] W. J. Fry, C. B. Ernst, J. C. Stanley, and B. Brink, ‘Renovascular hypertension in the pediatric patient.’, *Arch Surg*, vol. 107, no. 5, pp. 692–698, 1973.
- [57] H. Goldblatt, J. R. Kahn, and R. F. Hanzal, ‘Studies on Experimental Hypertension : Ix. the Effect on Blood Pressure of Constriction of the Abdominal Aorta Above and Below the Site of Origin of Both Main Renal Arteries.’, *J Exp Med*, vol. 69, no. 5, pp. 649–74, Apr. 1939, doi: 10.1084/jem.69.5.649.
- [58] D. M. Coleman *et al.*, ‘Surgical management of pediatric renin-mediated hypertension secondary to renal artery occlusive disease and abdominal aortic coarctation’, *J Vasc Surg*, vol. 72, no. 6, pp. 2035-2046.e1, 2020, doi: 10.1016/j.jvs.2020.02.045.
- [59] J. C. Stanley, E. Criado, J. L. Eliason, G. R. Upchurch, R. Berguer, and J. E. Rectenwald, ‘Abdominal aortic coarctation: Surgical treatment of 53 patients with a thoracoabdominal bypass, patch aortoplasty, or interposition aorto-aortic graft’, *J Vasc Surg*, vol. 48, no. 5, pp. 1073–1082, 2008, doi: 10.1016/j.jvs.2008.05.078.
- [60] R. K. Rumman *et al.*, ‘Management and Outcomes of Childhood Renal Artery Stenosis and Middle Aortic Syndrome’, *Am J Hypertens*, vol. 31, no. 6, pp. 687–695, May 2018, doi: 10.1093/AJH/HPY014.

- [61] P. P. Roeleveld *et al.*, ‘Hypoplastic left heart syndrome: from fetus to fontan’, *Cardiol Young*, vol. 28, no. 11, pp. 1275–1288, Nov. 2018, doi: 10.1017/S104795111800135X.
- [62] R. G. Ohye, D. Schranz, and Y. D’Udekem, ‘Current therapy for hypoplastic left heart syndrome and related single ventricle lesions’, *Circulation*, vol. 134, no. 17, pp. 1265–1279, 2016, doi: 10.1161/CIRCULATIONAHA.116.022816.
- [63] M. Butlin, A. Qasem, and A. P. Avolio, ‘Estimation of central aortic pressure waveform features derived from the brachial cuff volume displacement waveform’, *Proceedings of the Annual International Conference of the IEEE Engineering in Medicine and Biology Society, EMBS*, pp. 2591–2594, 2012, doi: 10.1109/EMBC.2012.6346494.
- [64] T. Weber *et al.*, ‘Validation of a Brachial Cuff-Based Method for Estimating Central Systolic Blood Pressure’, *Hypertension*, vol. 58, no. 5, pp. 825–832, Nov. 2011, doi: 10.1161/HYPERTENSIONAHA.111.176313.
- [65] R. E. D. Climie, M. G. Schultz, S. B. Nikolic, K. D. K. Ahuja, J. W. Fell, and J. E. Sharman, ‘Validity and reliability of central blood pressure estimated by upper arm oscillometric cuff pressure’, *Am J Hypertens*, vol. 25, no. 4, pp. 414–420, Apr. 2012, doi: 10.1038/AJH.2011.238.
- [66] B. A. Baba, P. T. Johan, and J. C. Mohan, ‘Comparison of central aortic pressure to brachial artery pressure in hypertensive patients on drug treatment: An observational study’, *Indian Heart J*, vol. 70, no. Suppl 3, p. S208, Dec. 2018, doi: 10.1016/J.IHJ.2018.10.418.
- [67] S. Muzzarelli *et al.*, ‘Prediction of Hemodynamic Severity of Coarctation by Magnetic Resonance Imaging’, *Am J Cardiol*, vol. 108, no. 9, pp. 1335–1340, Nov. 2011, doi: 10.1016/J.AMJCARD.2011.06.051.
- [68] S. Aslan *et al.*, ‘Non-invasive Prediction of Peak Systolic Pressure Drop across Coarctation of Aorta using Computational Fluid Dynamics’, *Annu Int Conf IEEE Eng Med Biol Soc*, vol. 2020, p. 2295, Jul. 2020, doi: 10.1109/EMBC44109.2020.9176461.
- [69] ‘Physiology, Cardiac Output - StatPearls - NCBI Bookshelf’.
<https://www.ncbi.nlm.nih.gov/books/NBK470455/> (accessed Nov. 14, 2022).
- [70] G. de Simone *et al.*, ‘Stroke Volume and Cardiac Output in Normotensive Children and Adults’, *Circulation*, vol. 95, no. 7, pp. 1837–1843, Apr. 1997, doi: 10.1161/01.CIR.95.7.1837.
- [71] J. D. Humphrey, D. G. Harrison, C. A. Figueroa, P. Lacolley, and S. Laurent, ‘Central Artery stiffness in hypertension and aging a problem with cause and consequence’, *Circ Res*, vol. 118, no. 3, pp. 379–381, 2016, doi: 10.1161/CIRCRESAHA.115.307722.
- [72] S. Laurent and P. Boutouyrie, ‘The structural factor of hypertension: large and small artery alterations’, *Circ Res*, vol. 116, no. 6, pp. 1007–1021, Mar. 2015, doi: 10.1161/CIRCRESAHA.116.303596.
- [73] E. G. Lakatta, M. Wang, and S. S. Najjar, ‘Arterial Aging and Subclinical Arterial Disease are Fundamentally Inter twined at Macroscopic and Molecular Levels’, *Med Clin North Am*, vol. 93, no. 3, p. 583, May 2009, doi: 10.1016/J.MCNA.2009.02.008.

- [74] S. Kovalova, J. Necas, and J. Vespalec, ‘What is a “normal” right ventricle?’, *European Journal of Echocardiography*, vol. 7, no. 4, pp. 293–297, Aug. 2006, doi: 10.1016/J.EUJE.2005.06.010.
- [75] M. J. Faber *et al.*, ‘Right and left ventricular function after chronic pulmonary artery banding in rats assessed with biventricular pressure-volume loops’, *American Journal of Physiology-Heart and Circulatory Physiology*, vol. 291, no. 4, pp. H1580–H1586, 2006, doi: 10.1152/ajpheart.00286.2006.
- [76] K. A. Brown and R. v. Ditchey, ‘Human right ventricular end-systolic pressure-volume relation defined by maximal elastance’, *Circulation*, vol. 78, no. 1, pp. 81–91, 1988, doi: 10.1161/01.CIR.78.1.81.
- [77] H. Suga, K. Sagawa, and A. A. Shoukas, ‘Load independence of the instantaneous pressure-volume ratio of the canine left ventricle and effects of epinephrine and heart rate on the ratio.’, *Circ Res*, vol. 32, no. 3, pp. 314–322, 1973, doi: 10.1161/01.RES.32.3.314.
- [78] S. M. Shavik, C. Tossas-Betancourt, C. A. Figueroa, S. Baek, and L. C. Lee, ‘Multiscale Modeling Framework of Ventricular-Arterial Bi-directional Interactions in the Cardiopulmonary Circulation’, *Front Physiol*, vol. 11, no. January, pp. 1–13, 2020, doi: 10.3389/fphys.2020.00002.
- [79] C. Tossas-Betancourt *et al.*, ‘Data-driven computational models of ventricular-arterial hemodynamics in pediatric pulmonary arterial hypertension’, *Front Physiol*, vol. 13, p. 1744, Sep. 2022, doi: 10.3389/FPHYS.2022.958734/BIBTEX.
- [80] S. Brimiouille *et al.*, ‘Single-beat estimation of right ventricular end-systolic pressure-volume relationship’, *Am J Physiol Heart Circ Physiol*, vol. 284, no. 5 53-5, pp. 1625–1630, May 2003, doi: 10.1152/AJPHEART.01023.2002/ASSET/IMAGES/LARGE/H40532250004.JPEG.
- [81] H. Senzaki, C. H. Chen, and D. A. Kass, ‘Single-beat estimation of end-systolic pressure-volume relation in humans: A new method with the potential for noninvasive application’, *Circulation*, vol. 94, no. 10, pp. 2497–2506, Nov. 1996, doi: 10.1161/01.CIR.94.10.2497.
- [82] C. A. Figueroa, I. E. Vignon-Clementel, K. E. Jansen, T. J. R. Hughes, and C. A. Taylor, ‘A coupled momentum method for modeling blood flow in three-dimensional deformable arteries’, *Comput Methods Appl Mech Eng*, vol. 195, no. 41–43, pp. 5685–5706, 2006, doi: 10.1016/j.cma.2005.11.011.
- [83] N. Xiao, J. D. Humphrey, and C. A. Figueroa, ‘Multi-scale computational model of three-dimensional hemodynamics within a deformable full-body arterial network’, *J Comput Phys*, vol. 244, pp. 22–40, 2013, doi: 10.1016/j.jcp.2012.09.016.
- [84] K. D. Lau and C. A. Figueroa, ‘Simulation of short-term pressure regulation during the tilt test in a coupled 3D–0D closed-loop model of the circulation’, *Biomech Model Mechanobiol*, vol. 14, no. 4, pp. 915–929, 2015, doi: 10.1007/s10237-014-0645-x.
- [85] C. J. Arthurs *et al.*, ‘CRIMSON: An open-source software framework for cardiovascular integrated modelling and simulation’, *PLoS Comput Biol*, vol. 17, no. 5, p. e1008881, May 2021, doi: 10.1371/journal.pcbi.1008881.

- [86] I. E. Vignon-clementel, C. A. Figueroa, K. E. Jansen, and C. A. Taylor, ‘Outflow boundary conditions for three-dimensional finite element modeling of blood flow and pressure in arteries’, vol. 195, pp. 3776–3796, 2006, doi: 10.1016/j.cma.2005.04.014.
- [87] H. J. Kim *et al.*, ‘On coupling a lumped parameter heart model and a three-dimensional finite element aorta model’, *Ann Biomed Eng*, vol. 37, no. 11, pp. 2153–2169, Nov. 2009, doi: 10.1007/S10439-009-9760-8/FIGURES/10.
- [88] C. J. Arthurs, K. D. Lau, K. N. Asrress, S. R. Redwood, and C. Alberto Figueroa, ‘A mathematical model of coronary blood flow control: Simulation of patientspecific three-dimensional hemodynamics during exercise’, *Am J Physiol Heart Circ Physiol*, vol. 310, no. 9, pp. H1242–H1258, May 2016, doi: 10.1152/ajpheart.00517.2015.
- [89] Y. Ahmed *et al.*, ‘Interventional Planning for Endovascular Revision of a Lateral Tunnel Fontan: A Patient-Specific Computational Analysis’, *Front Physiol*, vol. 12, p. 1226, Aug. 2021, doi: 10.3389/FPHYS.2021.718254/BIBTEX.
- [90] T. M. J. Van Bakel *et al.*, ‘Cardiac remodelling following thoracic endovascular aortic repair for descending aortic aneurysms’, *European Journal of Cardio-thoracic Surgery*, vol. 55, no. 6, pp. 1061–1070, 2019, doi: 10.1093/ejcts/ezy399.
- [91] T. Hirai, S. Sasayama, T. Kawasaki, and S. I. Yagi, ‘Stiffness of systemic arteries in patients with myocardial infarction. A noninvasive method to predict severity of coronary atherosclerosis’, *Circulation*, vol. 80, no. 1, pp. 78–86, 1989, doi: 10.1161/01.CIR.80.1.78.
- [92] M. Silva Vieira, C. J. Arthurs, T. Hussain, R. Razavi, and C. A. Figueroa, ‘Patient-specific modeling of right coronary circulation vulnerability post-liver transplant in Alagille’s syndrome’, *PLoS One*, vol. 13, no. 11, pp. 1–16, 2018, doi: 10.1371/journal.pone.0205829.
- [93] N. Xiao, J. Alastruey, and C. A. Figueroa, ‘A Systematic Comparison between 1-D and 3-D Hemodynamics in Compliant Arterial Models’, *Int J Numer Method Biomed Eng*, vol. 30, no. 2, p. 204, Feb. 2014, doi: 10.1002/CNM.2598.
- [94] S. M. Shavik, L. Zhong, X. Zhao, and L. C. Lee, ‘In-silico assessment of the effects of right ventricular assist device on pulmonary arterial hypertension using an image based biventricular modeling framework’, *Mech Res Commun*, vol. 97, pp. 101–111, 2019, doi: 10.1016/j.mechrescom.2019.04.008.
- [95] S. M. Shavik *et al.*, ‘Computational Modeling Studies of the Roles of Left Ventricular Geometry, Afterload, and Muscle Contractility on Myocardial Strains in Heart Failure with Preserved Ejection Fraction’, *Journal of Cardiovascular Translational Research* 2021, pp. 1–15, Apr. 2021, doi: 10.1007/S12265-021-10130-Y.
- [96] M. S. Alnæs *et al.*, ‘The FEniCS Project Version 1.5’, vol. 3, no. 100, pp. 9–23, 2015, doi: 10.11588/ans.2015.100.20553.
- [97] G. Sommer *et al.*, ‘Biomechanical properties and microstructure of human ventricular myocardium’, *Acta Biomater*, vol. 24, pp. 172–192, Sep. 2015, doi: 10.1016/J.ACTBIO.2015.06.031.

- [98] J. G. Pinto and Y. C. Fung, ‘Mechanical properties of the heart muscle in the passive state’, *J Biomech*, vol. 6, no. 6, 1973, doi: 10.1016/0021-9290(73)90017-1.
- [99] K. D. Costa, J. W. Holmes, and A. D. McCulloch, ‘Modelling cardiac mechanical properties in three dimensions’, *Philosophical Transactions of the Royal Society of London. Series A: Mathematical, Physical and Engineering Sciences*, vol. 359, no. 1783, pp. 1233–1250, Jun. 2001, doi: 10.1098/RSTA.2001.0828.
- [100] G. A. Holzapfel, T. C. Gasser, and R. W. Ogden, ‘A New Constitutive Framework for Arterial Wall Mechanics and a Comparative Study of Material Models’, *Journal of elasticity and the physical science of solids* 2000 61:1, vol. 61, no. 1, pp. 1–48, 2000, doi: 10.1023/A:1010835316564.
- [101] H. Schmid *et al.*, ‘Myocardial material parameter estimation’, *Biomechanics and Modeling in Mechanobiology* 2007 7:3, vol. 7, no. 3, pp. 161–173, May 2007, doi: 10.1007/S10237-007-0083-0.
- [102] D. Nordsletten *et al.*, ‘A viscoelastic model for human myocardium’, *Acta Biomater*, vol. 135, pp. 441–457, Nov. 2021, doi: 10.1016/J.ACTBIO.2021.08.036.
- [103] O. Gültekin, G. Sommer, and G. A. Holzapfel, ‘An orthotropic viscoelastic model for the passive myocardium: continuum basis and numerical treatment’, <http://dx.doi.org/10.1080/10255842.2016.1176155>, vol. 19, no. 15, pp. 1647–1664, Nov. 2016, doi: 10.1080/10255842.2016.1176155.
- [104] W. Zhang, A. Capilnasiu, and D. Nordsletten, ‘Comparative Analysis of Nonlinear Viscoelastic Models Across Common Biomechanical Experiments’, *Journal of Elasticity* 2021 145:1, vol. 145, no. 1, pp. 117–152, Apr. 2021, doi: 10.1007/S10659-021-09827-7.
- [105] J. M. Guccione, A. D. McCulloch, and L. K. Waldman, ‘Passive Material Properties of Intact Ventricular Myocardium Determined From a Cylindrical Model’, *J Biomech Eng*, vol. 113, no. 1, pp. 42–55, 1991.
- [106] A. Y. K. Wong, ‘Mechanics of cardiac muscle, based on Huxley’s model: Mathematical simulation of isometric contraction’, *J Biomech*, vol. 4, no. 6, pp. 529–540, Dec. 1971, doi: 10.1016/0021-9290(71)90042-X.
- [107] J. M. Guccione, L. K. Waldman, and A. D. McCulloch, ‘Mechanics of active contraction in cardiac muscle: Part II—cylindrical models of the systolic left ventricle’, *J Biomech Eng*, vol. 115, no. 1, pp. 82–90, 1993, doi: 10.1115/1.2895474.
- [108] S. A. Niederer, P. J. Hunter, and N. P. Smith, ‘A Quantitative Analysis of Cardiac Myocyte Relaxation: A Simulation Study’, *Biophys J*, vol. 90, pp. 1697–1722, 2006, doi: 10.1529/biophysj.105.069534.
- [109] J. J. Rice, F. Wang, D. M. Bers, and P. P. de Tombe, ‘Approximate model of cooperative activation and crossbridge cycling in cardiac muscle using ordinary differential equations’, *Biophys J*, vol. 95, no. 5, pp. 2368–2390, Sep. 2008, doi: 10.1529/BIOPHYSJ.107.119487.

- [110] R. Chabiniok *et al.*, ‘Multiphysics and multiscale modelling, data–model fusion and integration of organ physiology in the clinic: Ventricular cardiac mechanics’, *Interface Focus*, vol. 6, no. 2, Apr. 2016, doi: 10.1098/RSFS.2015.0083.
- [111] P. J. Hunter, A. D. McCulloch, and H. E. D. J. ter Keurs, ‘Modelling the mechanical properties of cardiac muscle’, *Prog Biophys Mol Biol*, vol. 69, no. 2–3, pp. 289–331, 1998, doi: 10.1016/S0079-6107(98)00013-3.
- [112] S. M. Shavik, Z. Jiang, S. Baek, and L. C. Lee, ‘High spatial resolution multi-organ finite element modeling of ventricular-arterial coupling’, *Front Physiol*, vol. 9, no. MAR, 2018, doi: 10.3389/fphys.2018.00119.
- [113] D. D. Ivy, E. B. Rosenzweig, J.-C. Lemarié, M. Brand, D. Rosenberg, and R. J. Barst, ‘Long-Term Outcomes in Children With Pulmonary Arterial Hypertension Treated With Bosentan in Real-World Clinical Settings’, *Am J Cardiol*, vol. 106, no. 9, pp. 1332–1338, Nov. 2010, doi: 10.1016/j.amjcard.2010.06.064.
- [114] J. B. Strait and E. G. Lakatta, ‘Aging-Associated Cardiovascular Changes and Their Relationship to Heart Failure’, *Heart Failure Clinics*, vol. 8, no. 1. NIH Public Access, pp. 143–164, Jan. 2012. doi: 10.1016/j.hfc.2011.08.011.
- [115] J. M. Douwes, M. T. R. Roofthoof, B. Bartelds, M. D. Talsma, H. L. Hillege, and R. M. F. Berger, ‘Pulsatile haemodynamic parameters are predictors of survival in paediatric pulmonary arterial hypertension’, *Int J Cardiol*, vol. 168, no. 2, pp. 1370–1377, 2013, doi: 10.1016/j.ijcard.2012.12.080.
- [116] R. M. F. Berger and D. Bonnet, ‘Treatment options for paediatric pulmonary arterial hypertension’, *European Respiratory Review*, vol. 19, no. 118, pp. 321–330, 2010, doi: 10.1183/09059180.00008410.
- [117] J. D. Humphrey and C. A. Taylor, ‘Intracranial and Abdominal Aortic Aneurysms: Similarities, Differences, and Need for a New Class of Computational Models’, *Annu Rev Biomed Eng*, vol. 10, no. 1, pp. 221–246, Aug. 2008, doi: 10.1146/annurev.bioeng.10.061807.160439.
- [118] R. Miller, E. Kerfoot, C. Mauer, T. F. Ismail, A. A. Young, and D. A. Nordsletten, ‘An Implementation of Patient-Specific Biventricular Mechanics Simulations With a Deep Learning and Computational Pipeline’, *Front Physiol*, vol. 12, p. 1398, Sep. 2021, doi: 10.3389/FPHYS.2021.716597/BIBTEX.
- [119] V. Bikia *et al.*, ‘Noninvasive Cardiac Output and Central Systolic Pressure from Cuff-Pressure and Pulse Wave Velocity’, *IEEE J Biomed Health Inform*, vol. 24, no. 7, pp. 1968–1981, Jul. 2020, doi: 10.1109/JBHI.2019.2956604.
- [120] V. O. Kheyfets, W. O’Dell, T. Smith, J. J. Reilly, and E. A. Finol, ‘Considerations for numerical modeling of the pulmonary circulation - A review with a focus on pulmonary hypertension’, *Journal of Biomechanical Engineering*, vol. 135, no. 6. American Society of Mechanical Engineers Digital Collection, Jun. 01, 2013. doi: 10.1115/1.4024141.
- [121] B. T. Tang, S. S. Pickard, F. P. Chan, P. S. Tsao, C. A. Taylor, and J. A. Feinstein, ‘Wall shear stress is decreased in the pulmonary arteries of patients with pulmonary arterial

- hypertension: An image-based, computational fluid dynamics study’, *Pulm Circ*, vol. 2, no. 4, pp. 470–476, 2012, doi: 10.4103/2045-8932.105035.
- [122] V. O. Kheyfets *et al.*, ‘Patient-specific computational modeling of blood flow in the pulmonary arterial circulation’, *Comput Methods Programs Biomed*, vol. 120, no. 2, pp. 88–101, 2015, doi: 10.1016/j.cmpb.2015.04.005.
- [123] B. A. Zambrano *et al.*, ‘Image-based computational assessment of vascular wall mechanics and hemodynamics in pulmonary arterial hypertension patients’, *J Biomech*, vol. 68, pp. 84–92, Feb. 2018, doi: 10.1016/j.jbiomech.2017.12.022.
- [124] M. K. Rausch, A. Dam, S. Göktepe, O. J. Abilez, and E. Kuhl, ‘Computational modeling of growth: Systemic and pulmonary hypertension in the heart’, *Biomech Model Mechanobiol*, vol. 10, no. 6, pp. 799–811, 2011, doi: 10.1007/s10237-010-0275-x.
- [125] R. Avazmohammadi, E. A. Mendiola, D. S. Li, P. Vanderslice, R. A. F. Dixon, and M. S. Sacks, ‘Interactions Between Structural Remodeling and Hypertrophy in the Right Ventricle in Response to Pulmonary Arterial Hypertension’, *J Biomech Eng*, vol. 141, no. 9, p. 091016, 2019, doi: 10.1115/1.4044174.
- [126] C. A. Miller *et al.*, ‘Quantification of left ventricular indices from SSFP cine imaging: Impact of real-world variability in analysis methodology and utility of geometric modeling’, *Journal of Magnetic Resonance Imaging*, vol. 37, no. 5, pp. 1213–1222, May 2013, doi: 10.1002/jmri.23892.
- [127] J. Caudron, J. Fares, V. Lefebvre, P. H. Vivier, C. Petitjean, and J. N. Dacher, ‘Cardiac MRI Assessment of Right Ventricular Function in Acquired Heart Disease. Factors of Variability.’, *Acad Radiol*, vol. 19, no. 8, pp. 991–1002, 2012, doi: 10.1016/j.acra.2012.03.022.
- [128] C. Petitjean and J. N. Dacher, ‘A review of segmentation methods in short axis cardiac MR images’, *Medical Image Analysis*, vol. 15, no. 2. Elsevier, pp. 169–184, Apr. 01, 2011. doi: 10.1016/j.media.2010.12.004.
- [129] W. J. Rogers *et al.*, ‘Quantification of and correction for left ventricular systolic long-axis shortening by magnetic resonance tissue tagging and slice isolation’, *Circulation*, vol. 84, no. 2, pp. 721–731, 1991, doi: 10.1161/01.CIR.84.2.721.
- [130] S. S. Klein, T. P. Graham, and C. H. Lorenz, ‘Noninvasive Delineation of Normal Right Ventricular Contractile Motion With Magnetic Resonance Imaging Myocardial Tagging’, 1998. doi: 10.1114/1.75.
- [131] A. Guz, J. A. Innes, and K. Murphy, ‘Respiratory modulation of left ventricular stroke volume in man measured using pulsed Doppler ultrasound.’, *J Physiol*, vol. 393, no. 1, pp. 499–512, Dec. 1987, doi: 10.1113/JPHYSIOL.1987.SP016836.
- [132] M. Gusseva *et al.*, ‘Model-Assisted Time-Synchronization of Cardiac MR Image and Catheter Pressure Data’, *Lecture Notes in Computer Science (including subseries Lecture Notes in Artificial Intelligence and Lecture Notes in Bioinformatics)*, vol. 12738 LNCS, pp. 362–372, 2021, doi: 10.1007/978-3-030-78710-3_35.

- [133] M. Gusseva *et al.*, ‘Time-Synchronization of Interventional Cardiovascular Magnetic Resonance Data Using a Biomechanical Model for Pressure-Volume Loop Analysis’, *Journal of Magnetic Resonance Imaging*, May 2022, doi: 10.1002/JMRI.28216.
- [134] O. Gal, ‘fit_ellipse’. MATLAB Central File Exchange, 2020.
- [135] I. E. Vignon-Clementel, C. A. Figueroa, K. E. Jansen, and C. A. Taylor, ‘Outflow boundary conditions for three-dimensional finite element modeling of blood flow and pressure in arteries’, vol. 195, pp. 3776–3796, 2006, doi: 10.1016/j.cma.2005.04.014.
- [136] J. Alastruey, N. Xiao, H. Fok, T. Schaeffter, and C. A. Figueroa, ‘On the impact of modelling assumptions in multi-scale, subject-specific models of aortic haemodynamics’, *J R Soc Interface*, vol. 13, no. 119, 2016, doi: <http://dx.doi.org/10.1098/rsif.2016.0073>.
- [137] O. Sahni, J. Müller, K. E. Jansen, M. S. Shephard, and C. A. Taylor, ‘Efficient anisotropic adaptive discretization of the cardiovascular system’, *Comput Methods Appl Mech Eng*, vol. 195, no. 41–43, pp. 5634–5655, 2006, doi: 10.1016/j.cma.2005.10.018.
- [138] C. A. Figueroa, I. E. Vignon-Clementel, K. E. Jansen, T. J. R. Hughes, and C. A. Taylor, ‘A coupled momentum method for modeling blood flow in three-dimensional deformable arteries’, *Comput Methods Appl Mech Eng*, vol. 195, no. 41–43, pp. 5685–5706, Aug. 2006, doi: 10.1016/j.cma.2005.11.011.
- [139] S. Roccabianca, C. A. Figueroa, G. Tellides, and J. D. Humphrey, ‘Quantification of regional differences in aortic stiffness in the aging human’, *J Mech Behav Biomed Mater*, vol. 29, pp. 618–634, 2014, doi: 10.1016/j.jmbbm.2013.01.026.
- [140] N. Li, S. Zhang, J. Hou, I. K. K. Jang, and B. Yu, ‘Assessment of pulmonary artery morphology by optical coherence tomography’, *Heart Lung Circ*, vol. 21, no. 12, pp. 778–781, 2012, doi: 10.1016/j.hlc.2012.07.014.
- [141] C. J. Arthurs, R. G. Grifka, P. Agarwal, A. L. Dorfman, A. v. John, and C. A. Figueroa, ‘Reproducing Patient-Specific Hemodynamics in the Blalock–Taussig Circulation Using a Flexible Multi-Domain Simulation Framework: Applications for Optimal Shunt Design’, *Front Pediatr*, vol. 5, no. April, pp. 1–13, 2017, doi: 10.3389/fped.2017.00078.
- [142] S. Sankaran, M. E. Moghadam, A. M. Kahn, E. E. Tseng, J. M. Guccione, and A. L. Marsden, ‘Patient-specific multiscale modeling of blood flow for coronary artery bypass graft surgery’, *Ann Biomed Eng*, vol. 40, no. 10, pp. 2228–2242, 2012, doi: 10.1007/s10439-012-0579-3.
- [143] A. L. Marsden, ‘Simulation based planning of surgical interventions in pediatric cardiology’, *Physics of Fluids*, vol. 25, no. 10, p. 101303, Oct. 2013, doi: 10.1063/1.4825031.
- [144] J. P. Mynard, M. R. Davidson, D. J. Penny, and J. J. Smolich, ‘A simple, versatile valve model for use in lumped parameter and one-dimensional cardiovascular models’, *Int J Numer Method Biomed Eng*, vol. 28, no. 6–7, pp. 626–641, 2012, doi: 10.1002/cnm.1466.
- [145] Y. Ahmed *et al.*, ‘Interventional Planning for Endovascular Revision of a Lateral Tunnel Fontan: A Patient-Specific Computational Analysis’, *Front Physiol*, vol. 12, no. August, pp. 1–11, 2021, doi: 10.3389/fphys.2021.718254.

- [146] M. Hadjicharalambous *et al.*, ‘Investigating the reference domain influence in personalised models of cardiac mechanics’, *Biomech Model Mechanobiol*, no. 0123456789, 2021, doi: 10.1007/s10237-021-01464-2.
- [147] D. D. Streeter, H. M. Spotnitz, D. P. Patel, J. Ross, and E. H. Sonnenblick, ‘Fiber orientation in the canine left ventricle during diastole and systole.’, *Circ Res*, vol. 24, no. 3, pp. 339–347, 1969, doi: 10.1161/01.RES.24.3.339.
- [148] J. D. Bayer, R. C. Blake, G. Plank, and N. A. Trayanova, ‘A novel rule-based algorithm for assigning myocardial fiber orientation to computational heart models’, *Ann Biomed Eng*, vol. 40, no. 10, pp. 2243–2254, 2012, doi: 10.1007/s10439-012-0593-5.
- [149] C. Geuzaine and J. F. Remacle, ‘Gmsh: A 3-D finite element mesh generator with built-in pre- and post-processing facilities’, *Int J Numer Methods Eng*, vol. 79, no. 11, pp. 1309–1331, Sep. 2009, doi: 10.1002/nme.2579.
- [150] L. J. Dell’Italia and R. A. Walsh, ‘Application of a time varying elastance model to right ventricular performance in man’, *Cardiovasc Res*, vol. 22, no. 12, pp. 864–874, Dec. 1988, doi: 10.1093/cvr/22.12.864.
- [151] H. Finsberg *et al.*, ‘Efficient estimation of personalized biventricular mechanical function employing gradient-based optimization’, *Int J Numer Method Biomed Eng*, vol. 34, no. 7, 2018, doi: 10.1002/cnm.2982.
- [152] D. A. Kass, T. Yamazaki, D. Burkhoff, W. L. Maughan, and K. Sagawa, ‘Determination of left ventricular end-systolic pressure-volume relationships by the conductance (volume) catheter technique.’, *Circulation*, vol. 73, no. 3, pp. 586–595, 1986, doi: 10.1161/01.CIR.73.3.586.
- [153] F. Cuomo *et al.*, ‘Sex-dependent differences in central artery haemodynamics in normal and fibulin-5 deficient mice: Implications for ageing’, *Proceedings of the Royal Society A: Mathematical, Physical and Engineering Sciences*, vol. 475, no. 2221, 2019, doi: 10.1098/rspa.2018.0076.
- [154] R. M. Friesen *et al.*, ‘Proximal pulmonary vascular stiffness as a prognostic factor in children with pulmonary arterial hypertension’, *Eur Heart J Cardiovasc Imaging*, vol. 20, no. 2, pp. 209–217, 2019, doi: 10.1093/ehjci/jey069.
- [155] S. Mahapatra, R. A. Nishimura, P. Sorajja, S. Cha, and M. D. McGoon, ‘Relationship of Pulmonary Arterial Capacitance and Mortality in Idiopathic Pulmonary Arterial Hypertension’, *J Am Coll Cardiol*, vol. 47, no. 4, pp. 799–803, Feb. 2006, doi: 10.1016/J.JACC.2005.09.054.
- [156] C. Apitz *et al.*, ‘Right Ventricular Dysfunction and B-Type Natriuretic Peptide in Asymptomatic Patients After Repair for Tetralogy of Fallot’, *Pediatr Cardiol*, vol. 30, pp. 898–904, 2009, doi: 10.1007/s00246-009-9453-y.
- [157] S. Sarikouch *et al.*, ‘Sex-specific pediatric Percentiles for ventricular size and mass as reference values for Cardiac MRI assessment by steady-state free-precession and phase-contrast MRI flow’, *Circ Cardiovasc Imaging*, vol. 3, no. 1, pp. 65–76, 2010, doi: 10.1161/CIRCIMAGING.109.859074.

- [158] K. Alfakih, S. Plein, H. Thiele, T. Jones, J. P. Ridgway, and M. U. Sivananthan, ‘Normal human left and right ventricular dimensions for MRI as assessed by turbo gradient echo and steady-state free precession imaging sequences’, *Journal of Magnetic Resonance Imaging*, vol. 17, no. 3, pp. 323–329, 2003, doi: 10.1002/jmri.10262.
- [159] Y. Benjamini and Y. Hochberg, ‘Controlling the False Discovery Rate: A Practical and Powerful Approach to Multiple Testing’, *Journal of the Royal Statistical Society: Series B (Methodological)*, vol. 57, no. 1, pp. 289–300, Jan. 1995, doi: 10.1111/J.2517-6161.1995.TB02031.X.
- [160] B. Kjellström, A. Lindholm, and E. Ostfeld, ‘Cardiac Magnetic Resonance Imaging in Pulmonary Arterial Hypertension: Ready for Clinical Practice and Guidelines?’, *Curr Heart Fail Rep*, vol. 17, no. 5, pp. 181–191, Oct. 2020, doi: 10.1007/S11897-020-00479-7/TABLES/1.
- [161] P. Y. Courand *et al.*, ‘Prognostic value of right ventricular ejection fraction in pulmonary arterial hypertension’, *European Respiratory Journal*, vol. 45, no. 1, pp. 139–149, Jan. 2015, doi: 10.1183/09031936.00158014.
- [162] C. Tji-Joong Gan *et al.*, ‘Impaired left ventricular filling due to right-to-left ventricular interaction in patients with pulmonary arterial hypertension’, *Am J Physiol Heart Circ Physiol*, vol. 290, pp. 1528–1533, 2006, doi: 10.1152/ajpheart.01031.2005.-The.
- [163] J. M. Lazar, A. R. Flores, D. J. Grandis, J. E. Orie, and D. S. Schulman, ‘Effects of chronic right ventricular pressure overload on left ventricular diastolic function’, *Am J Cardiol*, vol. 72, no. 15, pp. 1179–1182, Nov. 1993, doi: 10.1016/0002-9149(93)90990-T.
- [164] M. Hardziyenka *et al.*, ‘Right ventricular failure following chronic pressure overload is associated with reduction in left ventricular mass: Evidence for atrophic remodeling’, *J Am Coll Cardiol*, vol. 57, no. 8, pp. 921–928, Feb. 2011, doi: 10.1016/j.jacc.2010.08.648.
- [165] H. Finsberg *et al.*, ‘Computational quantification of patient-specific changes in ventricular dynamics associated with pulmonary hypertension’, *Am J Physiol Heart Circ Physiol*, vol. 317, no. 6, pp. H1363–H1375, 2019, doi: 10.1152/AJPHEART.00094.2019.
- [166] E. Manders *et al.*, ‘Contractile dysfunction of left ventricular cardiomyocytes in patients with pulmonary arterial hypertension’, *J Am Coll Cardiol*, vol. 64, no. 1, pp. 28–37, Jul. 2014, doi: 10.1016/J.JACC.2014.04.031.
- [167] A. Lungu, J. M. Wild, D. Capener, D. G. Kiely, A. J. Swift, and D. R. Hose, ‘MRI model-based non-invasive differential diagnosis in pulmonary hypertension’, *J Biomech*, vol. 47, no. 12, pp. 2941–2947, Sep. 2014, doi: 10.1016/J.JBIOMECH.2014.07.024.
- [168] A. Lungu, A. J. Swift, D. Capener, D. Kiely, R. Hose, and J. M. Wild, ‘Diagnosis of pulmonary hypertension from magnetic resonance imaging-based computational models and decision tree analysis.’, *Pulm Circ*, vol. 6, no. 2, pp. 181–90, Jun. 2016, doi: 10.1086/686020.
- [169] T. J. W. Dawes *et al.*, ‘Machine learning of threedimensional right ventricular motion enables outcome prediction in pulmonary hypertension: A cardiac MR imaging study’,

- Radiology*, vol. 283, no. 2, pp. 381–390, May 2017, doi: 10.1148/RADIOL.2016161315/SUPPL_FILE/R161315SUPPF3.JPG.
- [170] J. P. Alunni *et al.*, ‘Cardiac MRI in pulmonary artery hypertension: Correlations between morphological and functional parameters and invasive measurements’, *Eur Radiol*, vol. 20, no. 5, pp. 1149–1159, 2010, doi: 10.1007/s00330-009-1664-3.
- [171] W. Yang *et al.*, ‘Right ventricular stroke work correlates with outcomes in pediatric pulmonary arterial hypertension’, *Pulm Circ*, vol. 8, no. 3, Jul. 2018, doi: 10.1177/2045894018780534.
- [172] C. E. Simpson *et al.*, ‘Ventricular mass as a prognostic imaging biomarker in incident pulmonary arterial hypertension’, *Eur Respir J*, vol. 53, no. 4, Apr. 2019, doi: 10.1183/13993003.02067-2018.
- [173] J. Sanz *et al.*, ‘Evaluation of Pulmonary Artery Stiffness in Pulmonary Hypertension With Cardiac Magnetic Resonance’, *JACC Cardiovasc Imaging*, vol. 2, no. 3, pp. 286–295, 2009, doi: 10.1016/j.jcmg.2008.08.007.
- [174] C. J. Arthurs, N. Xiao, P. Moireau, T. Schaeffter, and C. Alberto Figueroa, ‘A flexible framework for sequential estimation of model parameters in computational hemodynamics’, *Adv. Model. and Simul. in Eng. Sci.*, vol. 7, p. 48, 2020, doi: 10.1186/s40323-020-00186-x.
- [175] M. Ismail, W. A. Wall, and M. W. Gee, ‘Adjoint-based inverse analysis of windkessel parameters for patient-specific vascular models’, *J Comput Phys*, vol. 244, pp. 113–130, Jul. 2013, doi: 10.1016/J.JCP.2012.10.028.
- [176] G. Troianowski, C. A. Taylor, J. A. Feinstein, and I. E. Vignon-Clementel, ‘Three-dimensional simulations in glenn patients: Clinically based boundary conditions, hemodynamic results and sensitivity to input data’, *J Biomech Eng*, vol. 133, no. 11, Nov. 2011, doi: 10.1115/1.4005377/399777.
- [177] W. K. Laskey, H. G. Parker, V. A. Ferrari, W. G. Kussmaul, and A. Noordergraaf, ‘Estimation of total systemic arterial compliance in humans’, *J Appl Physiol (1985)*, vol. 69, no. 1, pp. 112–119, 1990, doi: 10.1152/JAPPL.1990.69.1.112.
- [178] M. J. Colebank, M. Umar Qureshi, and M. S. Olufsen, ‘Sensitivity analysis and uncertainty quantification of 1-D models of pulmonary hemodynamics in mice under control and hypertensive conditions’, *Int J Numer Method Biomed Eng*, vol. 37, no. 11, p. e3242, Nov. 2021, doi: 10.1002/CNM.3242.
- [179] A. Caiazzo, F. Caforio, G. Montecinos, L. O. Muller, P. J. Blanco, and E. F. Toro, ‘Assessment of reduced-order unscented Kalman filter for parameter identification in 1-dimensional blood flow models using experimental data’, *Int J Numer Method Biomed Eng*, vol. 33, no. 8, Aug. 2017, doi: 10.1002/CNM.2843.
- [180] B. Matzuka, J. Mehlsen, H. Tran, and M. S. Olufsen, ‘Using kalman filtering to predict time-varying parameters in a model predicting baroreflex regulation during head-up tilt’, *IEEE Trans Biomed Eng*, vol. 62, no. 8, pp. 1992–2000, Aug. 2015, doi: 10.1109/TBME.2015.2409211.

- [181] P. Perdikaris and G. E. Karniadakis, ‘Model inversion via multi-fidelity Bayesian optimization: a new paradigm for parameter estimation in haemodynamics, and beyond’, *J R Soc Interface*, vol. 13, no. 118, May 2016, doi: 10.1098/RSIF.2015.1107.
- [182] J. S. Tran, D. E. Schiavazzi, A. B. Ramachandra, A. M. Kahn, and A. L. Marsden, ‘Automated Tuning for Parameter Identification and Uncertainty Quantification in Multi-scale Coronary Simulations’, *Comput Fluids*, vol. 142, p. 128, Jan. 2017, doi: 10.1016/J.COMPFLUID.2016.05.015.
- [183] W. J. Fry, C. B. Ernst, J. C. Stanley, and B. Brink, ‘Renovascular hypertension in the pediatric patient.’, *Arch Surg*, vol. 107, no. 5, pp. 692–8, Nov. 1973.
- [184] J. C. Stanley and W. J. Fry, ‘Pediatric renal artery occlusive disease and renovascular hypertension. Etiology, diagnosis, and operative treatment.’, *Arch Surg*, vol. 116, no. 5, pp. 669–76, May 1981.
- [185] J. C. Stanley, G. B. Zelenock, L. M. Messina, and T. W. Wakefield, ‘Pediatric renovascular hypertension: a thirty-year experience of operative treatment.’, *J Vasc Surg*, vol. 21, no. 2, pp. 212–26; discussion 226-7, Feb. 1995.
- [186] J. C. Stanley, E. Criado, G. R. Upchurch, P. D. Brophy, K. J. Cho, and J. E. Rectenwald, ‘Pediatric renovascular hypertension: 132 primary and 30 secondary operations in 97 children’, *J Vasc Surg*, vol. 44, no. 6, pp. 1219–1228, Dec. 2006, doi: 10.1016/j.jvs.2006.08.009.
- [187] D. M. Coleman *et al.*, ‘SS26 Surgical Management of Pediatric Renovascular Hypertension’, *J Vasc Surg*, vol. 65, no. 6, p. 138S, Jun. 2017, doi: 10.1016/j.jvs.2017.03.258.
- [188] R. K. Rumman *et al.*, ‘Disease beyond the arch: A systematic review of middle aortic syndrome in childhood’, *Am J Hypertens*, vol. 28, no. 7, pp. 833–846, Jul. 2015, doi: 10.1093/ajh/hpu296.
- [189] A. P. Rocchini, A. Rosenthal, A. C. Barger, A. R. Castaneda, and A. S. Nadas, ‘Pathogenesis of paradoxical hypertension after coarctation resection.’, *Circulation*, vol. 54, no. 3, pp. 382–7, Sep. 1976.
- [190] C. A. Figueroa, I. E. Vignon-Clementel, K. E. Jansen, T. J. R. Hughes, and C. A. Taylor, ‘A coupled momentum method for modeling blood flow in three-dimensional deformable arteries’, *Comput Methods Appl Mech Eng*, vol. 195, no. 41–43, pp. 5685–5706, 2006, doi: 10.1016/j.cma.2005.11.011.
- [191] T. M. J. van Bakel, K. D. Lau, J. Hirsch-Romano, S. Trimarchi, A. L. Dorfman, and C. A. Figueroa, ‘Patient-Specific Modeling of Hemodynamics: Supporting Surgical Planning in a Fontan Circulation Correction’, *J Cardiovasc Transl Res*, vol. 11, no. 2, pp. 145–155, Apr. 2018, doi: 10.1007/s12265-017-9781-x.
- [192] C. J. Arthurs, R. Khlebnikov, A. Melville, M. Marčan, A. Gomez, and F. Cuomo, ‘CRIMSON : An Open-Source Software Framework for Cardiovascular Integrated Modelling and Simulation’, pp. 1–20, 2020.

- [193] N. Xiao, J. Alastruey, and C. A. Figueroa, ‘A systematic comparison between 1-D and 3-D hemodynamics in compliant arterial models’, *Int J Numer Method Biomed Eng*, vol. 30, no. 2, pp. 204–31, 2013, doi: 10.1002/cnm.2598.
- [194] National High Blood Pressure Education Program Working Group on High Blood Pressure in Children and Adolescents, ‘The fourth report on the diagnosis, evaluation, and treatment of high blood pressure in children and adolescents.’, *Pediatrics*, vol. 114, no. 2 Suppl 4th Report, pp. 555–76, Aug. 2004.
- [195] B. M. T. Lantz, J. M. Foerster, D. P. Link, and J. W. Holcroft, ‘Regional distribution of cardiac output: Normal values in man determined by video dilution technique’, *American Journal of Roentgenology*, vol. 137, no. 5, pp. 903–907, 1981, doi: 10.2214/ajr.137.5.903.
- [196] J. R. Cohen and E. Birnbaum, ‘Coarctation of the abdominal aorta.’, *J Vasc Surg*, vol. 8, no. 2, pp. 160–4, Aug. 1988, doi: 10.1016/0741-5214(88)90404-1.
- [197] Y. P. Panayiotopoulos, M. R. Tyrrell, G. Koffman, J. F. Reidy, G. B. Haycock, and P. R. Taylor, ‘Mid-aortic syndrome presenting in childhood’, *British Journal of Surgery*, vol. 83, no. 2, pp. 235–240, 1996, doi: 10.1002/bjs.1800830228.
- [198] H. W. Scott and H. T. Bahnson, ‘Evidence for a renal factor in the hypertension of experimental coarctation of the aorta’, *Surgery*, vol. 30, no. 1, pp. 206–217, Jul. 1951, doi: 10.5555/URI:PII:0039606051900189.
- [199] D. Porras *et al.*, ‘Midaortic syndrome: 30 years of experience with medical, endovascular and surgical management’, *Pediatric Nephrology*, vol. 28, no. 10, pp. 2023–2033, Oct. 2013, doi: 10.1007/s00467-013-2514-8.
- [200] W. Sandmann, P. Dueppers, S. Pourhassan, A. Voiculescu, D. Klee, and K. M. Balzer, ‘Early and Long-term Results after Reconstructive Surgery in 42 Children and Two Young Adults with Renovascular Hypertension due to Fibromuscular Dysplasia and Middle Aortic Syndrome’, *European Journal of Vascular and Endovascular Surgery*, vol. 47, no. 5, pp. 509–516, May 2014, doi: 10.1016/j.ejvs.2013.12.012.
- [201] C. B. Sethna, B. S. Kaplan, A. M. Cahill, O. C. Velazquez, and K. E. C. Meyers, ‘Idiopathic mid-aortic syndrome in children’, *Pediatric Nephrology*, vol. 23, no. 7, pp. 1135–1142, Jul. 2008, doi: 10.1007/s00467-008-0767-4.
- [202] A. Tummolo *et al.*, ‘Mid-aortic syndrome: long-term outcome of 36 children’, *Pediatric Nephrology*, vol. 24, no. 11, pp. 2225–2232, Nov. 2009, doi: 10.1007/s00467-009-1242-6.
- [203] P. K. Castelli, J. R. Dillman, E. A. Smith, R. Vellody, K. Cho, and J. C. Stanley, ‘Imaging of Renin-Mediated Hypertension in Children’, *American Journal of Roentgenology*, vol. 200, no. 6, pp. W661–W672, Jun. 2013, doi: 10.2214/AJR.12.9427.
- [204] C. A. Taylor and C. A. Figueroa, ‘Patient-specific modeling of cardiovascular mechanics.’, *Annu Rev Biomed Eng*, vol. 11, pp. 109–134, 2009, doi: 10.1146/annurev.bioeng.10.061807.160521.
- [205] T. M. van Bakel *et al.*, ‘Cardiac remodelling following thoracic endovascular aortic repair for descending aortic aneurysms †’, *European Journal of Cardio-Thoracic Surgery*, vol. 0, pp. 1–10, 2018, doi: 10.1093/ejcts/ezy399.

- [206] K. Tullus, D. J. Roebuck, C. A. McLaren, and S. D. Marks, ‘Imaging in the evaluation of renovascular disease’, *Pediatric Nephrology*, vol. 25, no. 6, pp. 1049–1056, Jun. 2010, doi: 10.1007/s00467-009-1320-9.
- [207] J. A. Sotelo *et al.*, ‘Pressure gradient prediction in aortic coarctation using a computational-fluid-dynamics model: validation against invasive pressure catheterization at rest and pharmacological stress’, *Journal of Cardiovascular Magnetic Resonance*, vol. 17, no. Suppl 1, p. Q78, 2015, doi: 10.1186/1532-429X-17-S1-Q78.
- [208] J. A. Noonan and A. S. Nadas, ‘The hypoplastic left heart syndrome; an analysis of 101 cases.’, *Pediatr Clin North Am*, vol. 5, no. 4, pp. 1029–1056, Nov. 1958, doi: 10.1016/s0031-3955(16)30727-1.
- [209] C. T. Mai *et al.*, ‘National population-based estimates for major birth defects, 2010–2014’, *Birth Defects Res*, vol. 111, no. 18, pp. 1420–1435, 2019, doi: 10.1002/bdr2.1589.
- [210] R. G. Ohye, D. Schranz, and Y. D’Udekem, ‘Current therapy for hypoplastic left heart syndrome and related single ventricle lesions’, *Circulation*, vol. 134, no. 17, pp. 1265–1279, 2016, doi: 10.1161/CIRCULATIONAHA.116.022816.
- [211] D. J. Barron, M. D. Kilby, B. Davies, J. G. Wright, T. J. Jones, and W. J. Brawn, ‘Hypoplastic left heart syndrome’, *The Lancet*, vol. 374, no. 9689, pp. 551–564, 2009, doi: 10.1016/S0140-6736(09)60563-8.
- [212] J. A. Feinstein *et al.*, ‘Hypoplastic left heart syndrome: Current considerations and expectations’, *J Am Coll Cardiol*, vol. 59, no. 1 SUPPL., 2012, doi: 10.1016/j.jacc.2011.09.022.
- [213] W. I. Douglas, C. S. Goldberg, R. S. Mosca, I. H. Law, and E. L. Bove, ‘Hemi-Fontan procedure for hypoplastic left heart syndrome: Outcome and suitability for Fontan’, *Annals of Thoracic Surgery*, vol. 68, no. 4, pp. 1361–1367, 1999, doi: 10.1016/S0003-4975(99)00915-7.
- [214] J. C. Hirsch *et al.*, ‘Fontan operation in the current era: A 15-year single institution experience’, *Ann Surg*, vol. 248, no. 3, pp. 402–408, 2008, doi: 10.1097/SLA.0b013e3181858286.
- [215] T. E. Downing *et al.*, ‘Surgical and catheter-based reinterventions are common in long-term survivors of the fontan operation’, *Circ Cardiovasc Interv*, vol. 10, no. 8, pp. 1–9, 2017, doi: 10.1161/CIRCINTERVENTIONS.116.004924.
- [216] M. Daley *et al.*, ‘Reintervention and survival in 1428 patients in the Australian and New Zealand Fontan Registry’, *Heart*, vol. 106, no. 10, pp. 751–757, 2020, doi: 10.1136/heartjnl-2019-315430.
- [217] C. S. Van Dorn, S. C. Menon, J. T. Johnson, R. W. Day, J. L. Hoffman, and A. T. Yetman, ‘Lifetime Cardiac Reinterventions Following the Fontan Procedure’, *Pediatr Cardiol*, vol. 36, no. 2, pp. 329–334, 2015, doi: 10.1007/s00246-014-1007-2.
- [218] M. Petko *et al.*, ‘Surgical reinterventions following the Fontan procedure’, *European Journal of Cardio-thoracic Surgery*, vol. 24, no. 2, pp. 255–259, 2003, doi: 10.1016/S1010-7940(03)00257-4.

- [219] H. K. Park, H. J. Shin, and Y. H. Park, ‘Outcomes of Fontan conversion for failing Fontan circulation: Mid-term results’, *Interact Cardiovasc Thorac Surg*, vol. 23, no. 1, pp. 14–17, 2016, doi: 10.1093/icvts/ivw062.
- [220] C. Tossas-Betancourt *et al.*, ‘Computational analysis of renal artery flow characteristics by modeling aortoplasty and aortic bypass interventions for abdominal aortic coarctation’, *J Vasc Surg*, vol. 71, no. 2, 2020, doi: 10.1016/j.jvs.2019.02.063.
- [221] J. Primeaux, A. Salavitarbar, J. C. Lu, R. G. Grifka, and C. A. Figueroa, ‘Characterization of Post-Operative Hemodynamics Following the Norwood Procedure Using Population Data and Multi-Scale Modeling’, *Front Physiol*, vol. 12, no. May, pp. 1–18, 2021, doi: 10.3389/fphys.2021.603040.
- [222] E. L. Bove, M. R. De Leval, F. Migliavacca, G. Guadagni, and G. Dubini, ‘Computational fluid dynamics in the evaluation of hemodynamic performance of cavopulmonary connections after the Norwood procedure for hypoplastic left heart syndrome’, *Journal of Thoracic and Cardiovascular Surgery*, vol. 126, no. 4, pp. 1040–1047, 2003, doi: 10.1016/S0022-5223(03)00698-6.
- [223] P. M. Trusty *et al.*, ‘The first cohort of prospective Fontan surgical planning patients with follow-up data: How accurate is surgical planning?’, *J Thorac Cardiovasc Surg*, vol. 157, no. 3, pp. 1146–1155, Mar. 2019, doi: 10.1016/j.jtcvs.2018.11.102.
- [224] M. Toma *et al.*, ‘Effect of edge-to-edge mitral valve repair on chordal strain: Fluid-structure interaction simulations’, *Biology (Basel)*, vol. 9, no. 7, pp. 1–12, 2020, doi: 10.3390/biology9070173.
- [225] C. Li *et al.*, ‘Porcine and bovine aortic valve comparison for surgical optimization: A fluid-structure interaction modeling study.’, *Int J Cardiol*, vol. 334, pp. 88–95, Jul. 2021, doi: 10.1016/j.ijcard.2021.04.051.
- [226] M. Restrepo *et al.*, ‘Surgical planning of the total cavopulmonary connection: robustness analysis.’, *Ann Biomed Eng*, vol. 43, no. 6, pp. 1321–1334, Jun. 2015, doi: 10.1007/s10439-014-1149-7.
- [227] K. S. Sundareswaran *et al.*, ‘Correction of pulmonary arteriovenous malformation using image-based surgical planning.’, *JACC Cardiovasc Imaging*, vol. 2, no. 8, pp. 1024–1030, Aug. 2009, doi: 10.1016/j.jcmg.2009.03.019.
- [228] D. A. de Zélicourt *et al.*, ‘Individualized computer-based surgical planning to address pulmonary arteriovenous malformations in patients with a single ventricle with an interrupted inferior vena cava and azygous continuation.’, *J Thorac Cardiovasc Surg*, vol. 141, no. 5, pp. 1170–1177, May 2011, doi: 10.1016/j.jtcvs.2010.11.032.
- [229] J. Michael Lee and G. J. Wilson, ‘Anisotropic tensile viscoelastic properties of vascular graft materials tested at low strain rates’, *Biomaterials*, vol. 7, no. 6, pp. 423–431, Nov. 1986, doi: 10.1016/0142-9612(86)90029-3.
- [230] J. P. Mynard, M. R. Davidson, D. J. Penny, and J. J. Smolich, ‘A simple, versatile valve model for use in lumped parameter and one-dimensional cardiovascular models’, *Int J Numer Method Biomed Eng*, vol. 28, no. 6–7, pp. 626–641, 2012, doi: 10.1002/cnm.1466.

- [231] C. A. Figueroa, I. E. Vignon-Clementel, K. E. Jansen, T. J. R. Hughes, and C. A. Taylor, 'A coupled momentum method for modeling blood flow in three-dimensional deformable arteries', *Comput Methods Appl Mech Eng*, vol. 195, no. 41–43, pp. 5685–5706, 2006, doi: 10.1016/j.cma.2005.11.011.
- [232] A. L. Marsden, I. E. Vignon-Clementel, F. P. Chan, J. A. Feinstein, and C. A. Taylor, 'Effects of exercise and respiration on hemodynamic efficiency in CFD simulations of the total cavopulmonary connection', *Ann Biomed Eng*, vol. 35, no. 2, pp. 250–263, 2007, doi: 10.1007/s10439-006-9224-3.
- [233] L. P. Dasi *et al.*, 'Fontan hemodynamics: importance of pulmonary artery diameter.', *J Thorac Cardiovasc Surg*, vol. 137, no. 3, pp. 560–564, Mar. 2009, doi: 10.1016/j.jtcvs.2008.04.036.
- [234] T. M. J. van Bakel, K. D. Lau, J. Hirsch-Romano, S. Trimarchi, A. L. Dorfman, and C. A. Figueroa, 'Patient-specific modeling of hemodynamics: Supporting surgical planning in a fontan circulation correction', *J Cardiovasc Transl Res*, vol. 11, no. 2, pp. 145–155, Apr. 2018, doi: 10.1007/s12265-017-9781-x.
- [235] F. J. H. Nauta *et al.*, 'Computational Fluid Dynamics and Aortic Thrombus Formation Following Thoracic Endovascular Aortic Repair', *Annals of Thoracic Surgery*, vol. 103, no. 6, pp. 1914–1921, 2017, doi: 10.1016/j.athoracsur.2016.09.067.
- [236] T. M. Van Bakel *et al.*, 'A computational analysis of different endograft designs for Zone 0 aortic arch repair', *European Journal of Cardio-thoracic Surgery*, vol. 54, no. 2, pp. 389–396, 2018, doi: 10.1093/ejcts/ezy068.
- [237] C. Tossas-Betancourt *et al.*, 'Computational analysis of renal artery flow characteristics by modeling aortoplasty and aortic bypass interventions for abdominal aortic coarctation', *J Vasc Surg*, vol. 71, no. 2, 2020, doi: 10.1016/j.jvs.2019.02.063.
- [238] C. M. Haggerty *et al.*, 'Simulations : Implications for the Reliability of Surgical Planning', vol. 40, no. 12, pp. 2639–2651, 2013, doi: 10.1007/s10439-012-0614-4.Comparing.
- [239] G. Troianowski, C. A. Taylor, J. A. Feinstein, and I. E. Vignon-Clementel, 'Three-dimensional simulations in glenn patients: Clinically based boundary conditions, hemodynamic results and sensitivity to input data', *J Biomech Eng*, vol. 133, no. 11, 2011, doi: 10.1115/1.4005377.
- [240] D. A. de Zélicourt and V. Kurtcuoglu, 'Patient-Specific Surgical Planning, Where Do We Stand? The Example of the Fontan Procedure', *Ann Biomed Eng*, vol. 44, no. 1, pp. 174–186, 2016, doi: 10.1007/s10439-015-1381-9.
- [241] Z. A. Wei *et al.*, 'Used To Meet the Clinical Timeline for Fontan Surgical Planning?', pp. 172–179, 2018, doi: 10.1016/j.jbiomech.2016.11.025.CAN.
- [242] N. Galiè *et al.*, 'Risk stratification and medical therapy of pulmonary arterial hypertension', *European Respiratory Journal*, vol. 53, no. 1, Jan. 2019, doi: 10.1183/13993003.01889-2018.

- [243] A. Boucly *et al.*, ‘Risk assessment, prognosis and guideline implementation in pulmonary arterial hypertension’, *European Respiratory Journal*, vol. 50, no. 2, p. 1700889, Aug. 2017, doi: 10.1183/13993003.00889-2017.
- [244] D. J. PATEL, F. M. DE FREITAS, J. C. GREENFIELD, and D. L. FRY, ‘Relationship of Radius To Pressure Along the Aorta in Living Dogs.’, *J Appl Physiol*, vol. 18, pp. 1111–7, 1963, doi: 10.1152/jappl.1963.18.6.1111.
- [245] K. C. White, J. F. Kavanaugh, D. M. Wang, and J. M. Tarbell, ‘Hemodynamics and wall shear rate in the abdominal aorta of dogs: Effects of vasoactive agents’, *Circ Res*, vol. 75, no. 4, pp. 637–649, 1994, doi: 10.1161/01.RES.75.4.637.
- [246] M. I. M. Noble, I. T. Gabe, D. Trenchard, and A. Guz, ‘Blood pressure and flow in the ascending aorta of conscious dogs’, *Cardiovasc Res*, vol. 1, no. 1, pp. 9–20, 1967, doi: 10.1093/cvr/1.1.9.
- [247] L. Rouleau, D. Tremblay, R. Cartier, R. Mongrain, and R. L. Leask, ‘Regional variations in canine descending aortic tissue mechanical properties change with formalin fixation’, *Cardiovascular Pathology*, vol. 21, no. 5, pp. 390–397, 2012, doi: 10.1016/j.carpath.2011.12.002.
- [248] X. Liu *et al.*, ‘Automatic Shape Optimization of Patient-Specific Tissue Engineered Vascular Grafts for Aortic Coarctation’, *Proceedings of the Annual International Conference of the IEEE Engineering in Medicine and Biology Society, EMBS*, vol. 2020-July, pp. 2319–2323, Jul. 2020, doi: 10.1109/EMBC44109.2020.9176371.
- [249] M. Luffel *et al.*, ‘SURGEM: A solid modeling tool for planning and optimizing pediatric heart surgeries’, *Computer-Aided Design*, vol. 70, pp. 3–12, Jan. 2016, doi: 10.1016/J.CAD.2015.06.018.
- [250] B. J. A. Janssen, T. de Celle, J. J. M. Debets, A. E. Brouns, M. F. Callahan, and T. L. Smith, ‘Effects of anesthetics on systemic hemodynamics in mice’, *Am J Physiol Heart Circ Physiol*, vol. 287, no. 4 56-4, pp. 1618–1624, 2004, doi: 10.1152/ajpheart.01192.2003.
- [251] A. J. Evans *et al.*, ‘Magnetic resonance imaging of blood flow with a phase subtraction technique. In vitro and in vivo validation.’, *Invest Radiol*, vol. 28, no. 2, pp. 109–115, Feb. 1993, doi: 10.1097/00004424-199302000-00004.
- [252] A. L. Pauca, M. F. O’Rourke, and N. D. Kon, ‘Prospective evaluation of a method for estimating ascending aortic pressure from the radial artery pressure waveform’, *Hypertension*, vol. 38, no. 4, pp. 932–937, 2001, doi: 10.1161/hy1001.096106.
- [253] F. Cuomo *et al.*, ‘Sex-dependent differences in central artery haemodynamics in normal and fibulin-5 deficient mice: Implications for ageing’, *Proceedings of the Royal Society A: Mathematical, Physical and Engineering Sciences*, vol. 475, no. 2221, 2019, doi: 10.1098/rspa.2018.0076.
- [254] O. Sahni, J. Müller, K. E. Jansen, M. S. Shephard, and C. A. Taylor, ‘Efficient anisotropic adaptive discretization of the cardiovascular system’, *Comput Methods Appl Mech Eng*, vol. 195, no. 41–43, pp. 5634–5655, 2006, doi: 10.1016/j.cma.2005.10.018.

- [255] I. E. Vignon-Clementel, C. A. Figueroa, K. E. Jansen, and C. A. Taylor, ‘Outflow boundary conditions for 3D simulations of non-periodic blood flow and pressure fields in deformable arteries’, *Comput Methods Biomech Biomed Engin*, vol. 13, no. 5, pp. 625–640, 2010, doi: 10.1080/10255840903413565.
- [256] C. J. Arthurs, K. D. Lau, K. N. Asress, S. R. Redwood, and C. A. Figueroa, ‘A mathematical model of coronary blood flow control: simulation of patient-specific three-dimensional hemodynamics during exercise’, *Am J Physiol Heart Circ Physiol*, vol. 310, no. 9, pp. H1242–H1258, May 2016, doi: 10.1152/ajpheart.00517.2015.